7-28-2017

Optimization and Bayesian Inference in Model-based Decision Making

Ali Abdollahi
ali.abdollahi@uconn.edu

Optimization and Bayesian Inference in Model-based Decision Making

Ali Abdollahi, Ph.D.

University of Connecticut, 2017

ABSTRACT

The focus of this dissertation is on using optimization and Bayesian inference in model-based decision making. We discuss two problems: (a) optimal battery charging and battery life management; (b) fault diagnosis using probabilistic graphical models. In the first part of this thesis, we address the optimal charging problem using a two-time-scale algorithm which performs fast-charging at the lower-level (fast time-scale), while managing the battery life at the higher-level (low time-scale). At the lower-level, we derive optimal charging algorithms for Li-ion batteries using equivalent electrical circuit models and quadratic optimization approaches. The objective function is considered as a linear combination of time-to-charge, energy-loss, temperature rise index, and any other arbitrary function of state-of-charge (SOC). A generic algorithm, which is applicable to any equivalent electrical circuit model of a battery, is derived for calculating the optimal current profile. At the higher-level, we propose a battery life management algorithm to determine the optimal values for the control parameters of the charging process, namely, maximum allowable current and maximum allowable terminal voltage. As a precursor to the battery life management algorithm, we propose two new battery capacity fade models that are shown to be statistically superior to

Ali Abdollahi, Ph.D.

University of Connecticut, 2017

the bi-exponential capacity fade model. In the second part of the thesis, we consider the fault diagnosis problem using probabilistic graphical models. We discuss the Detection-False Alarm (DFA), the Leaky Noisy OR (LNOR), and the logistic regression (LR)-based test models. Here, we prove the equivalence of DFA and LNOR test models. Then, we propose a unified test model that includes both the LNOR and the LR test models as special cases, and derive a Maximum *a posteriori* solution for the multiple fault diagnosis problem based on the unified test model using the Lagrangian relaxation method and deriving a dual cost function for the problem.

Optimization and Bayesian Inference in Model-based Decision Making

Ali Abdollahi

M.S., Electrical Engineering, Ferdowsi University of Mashhad, 2002

B.S., Electrical Engineering, Ferdowsi University of Mashhad, 1999

A Dissertation

Submitted in Partial Fulfillment of the

Requirements for the Degree of

Doctor of Philosophy

at the

University of Connecticut

2017

APPROVAL PAGE

Doctor of Philosophy Dissertation

Optimization and Bayesian Inference in Model-based Decision Making

Presented by

Ali Abdollahi, M.S. Electrical Engineering

Major Advisor _____
Krishna R. Pattipati

Associate Advisor _____
Yaakov Bar-Shalom

Associate Advisor _____
Shengli Zhou

University of Connecticut

2017

To: *my mother and my wife*

ACKNOWLEDGMENTS

Now that I am in the last stages of preparing my PhD thesis, I would like to spend some time to thank those who helped me during this journey. First, I would like to thank my major advisor, Prof. Krishna R. Pattipati, who helped me prepare this work. I love the moments that we discussed and I am thankful for his support, guidance, and encouragement. I learned from him lessons of research and lessons of life. I would like to thank my co-advisor, Prof. Yaakov Bar-Shalom, for his meticulous reading of my papers and for his helpful comments. I would like to thank Prof. Shengli Zhou for serving on my dissertation Committee.

I would like to thank Cyberlab students, Xu Han, Niranjan Raghunathan, Manisha Mishra, Pujitha Mannaru, Rajeev Ghimire, David Sidoti, Lingyi Zhang, Gopi Vinod Avvari, Bharath Pattipati, Donald McMenemy, and Spandana Vallabhaneni, for the friendly environment that they provided in Cyberlab, and I would like to especially thank Xu Han and Niranjan Raghunathan for their help in the optimal battery charging project.

I would like to thank Michael Rauth, Bob Card, and Travis Williams from Fairchild Semiconductor for the discussions that we had during the weekly teleconferences. I would also like to thank the Department Head, Prof. Rajeev Bansal, the Department Associate Head, Prof. John Chandy, and the administrative staff of the Department, Mary P. McCarthy, Karen Kuca, Celine Goorahoo, and Dee Stolstrom for their help.

Support from Fairchild Semiconductor, National Science Foundation (NSF), UTC Chair Professorship and UCONN's Academic Plan is gratefully acknowledged.

Finally, I would like to thank my family members who have always been the source of support, encouragement and love. I would like to specially thank and dedicate this work to my mother and my wife.

Contents

List of Figures

List of Tables

Chapter 1

Introduction

The focus of this dissertation is on optimization and Bayesian inference in model-based decision making. In the optimization part, our focus is on optimal battery charging. Figure 1.0.1 shows the block diagram of a battery management system (BMS). The battery fuel gauge (BFG) provides the charger with battery model parameters, battery capacity estimate, battery usage statistics, and battery state-of-charge (SOC). The charging process is considered as a two-level algorithm. In a higher level (level I), we determine the optimal values for maximum allowable current and maximum allowable terminal voltage of the battery. In a lower level (level II), we find the optimal charging current with respect to an objective function.

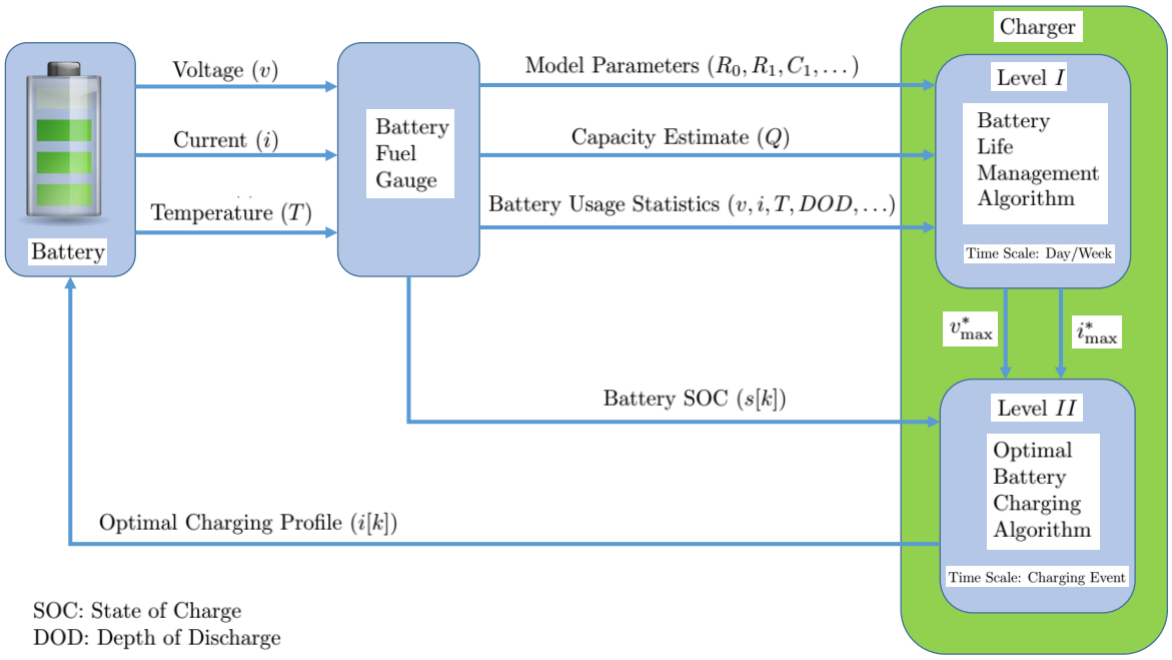

FIGURE 1.0.1: Battery management system (BMS) block diagram

At the lower level (level II), using equivalent electrical circuit models of the battery, we formulate the charging problem as a constrained optimization problem with an objective function that is a combination of three sub-objectives: time-to-charge (TTC), energy loss (EL), and a temperature rise index (TRI); the constraints are the battery dynamics, the maximum allowable terminal voltage, and the maximum allowable current. We show that under if a simple model (composed of an Open-Circuit Voltage (OCV) and a resistance) is used for the battery, the well-known Constant Current-Constant Voltage (CC-CV) policy with the value of the current in the CC stage being a function of the ratio of the weightings on TTC and EL, and of the resistance of the battery, is the optimal charging profile. The optimal battery charging problem is then formulated in its general form for any electrical model of the battery

and for a more general objective function (composed of weighted sum of TTC, EL, TRI, and any function of the state-of-charge (SOC)).

At the higher level (level I), as a precursor to formulating the battery life management in terms of an optimization problem, we present two new models for normalized battery capacity as functions of the number of cycles and two charge control parameters, viz., maximum terminal voltage of the battery and maximum charge current. These models are compared to a bi-exponential capacity model proposed in the literature. The effectiveness of the proposed models for forecasting the battery capacity is validated using experimental data and they are shown statistically to be substantially more accurate than the bi-exponential capacity model. The new models are used for battery life management by developing an optimal charging parameter selection method, which provides the best setting values for the two control variables to achieve a pre-specified desired "useful cycle life," while attaining the fastest possible time-to-charge.

In the Bayesian inference part, our focus is on the problem of fault diagnosis in probabilistic graphical models. The fault diagnosis problem can be represented as a tri-partite probabilistic graphical model. The first layer of this tri-partite graph is composed of the components of the system, which are the potential sources of failure. The health condition of each component is represented by a binary state variable, which is zero if the component is healthy and one otherwise. The second layer is composed of tests with binary outcomes (pass or fail), and the third layer constitutes of the noisy observations associated with the test outcomes. The cause-effect relations between the states of components and the observed test outcomes can be compactly modeled in terms of detection and false alarm probabilities. This model, which uses the concept of detection and false alarm probabilities, is referred to as the DFA test

model in this dissertation. The fault diagnosis problem is formulated as a maximum *a posteriori* (MAP) inference problem, and a dual cost function of the resulting optimization problem is derived. Another model, which is discussed, is the leaky noisy OR (LNOR) test model. We prove that, for every DFA test model, there is an equivalent LNOR test model. Thus, all the formulations involving the DFA test model are applicable to the LNOR test model. Another model that is discussed is the logistic regression (LR) test model. Then, a unified test model, which subsumes both the LNOR and the LR test models as special cases, is developed. The MAP problem for fault diagnosis for the unified test model is discussed and a dual cost function is derived.

1.1 Publications

Publications to-date include: [5, 6, 11, 9, 10, 7, 8, 135].

1. A. Abdollahi, X. Han, N. Raghunathan, B. Pattapati, B. Balasingam, K. R. Pattipati, Y. Bar-Shalom, and B. Card, "Optimal Charging for General Equivalent Electrical Battery Model, and Battery Life Management," *Journal of Energy Storage*, vol. 9, pp. 47–58, 2017.

2. A. Abdollahi, X. Han, G. V. Avvari, N. Raghunathan, B. Balasingam, K. R. Pattipati, and Y. Bar-Shalom, "Optimal battery charging, Part I: Minimizing time-to-charge, energy loss, and temperature rise for OCV-resistance battery model," *Journal of Power Sources*, vol. 303, pp. 388-398, 2016.

3. A. Abdollahi, K. R. Pattipati, A. Kodali, S. Singh, S. Zhang, and P. B. Luh, "Probabilistic Graphical Models for Fault Diagnosis in Complex Systems," Part-I

Ch. 5 in *Principles of Performance and Reliability Modeling and Evaluation*, Springer 2016. pp. 109–139.

4. A. Abdollahi, K. R. Pattipati, "Probabilistic Graphical Models for Fault Prognosis in Complex Systems," *in preparation*, 2017.

5. A. Abdollahi, K. R. Pattipati, "Unification of Leaky Noisy OR and Logistic Regression Models and Maximum A Posteriori Inference for Multiple Fault Diagnosis Using the Unified Model," in *International Workshop on Principles of Diagnosis (DX)*, Denver, CO., Oct., 2016.

6. A. Abdollahi, N. Raghunathan, X. Han, G. V. Avvari, B. Balasingam, K. R. Pattipati, and Y. Bar-Shalom, "Battery charging optimization for OCV-resistance equivalent circuit model," in *Proc. American Control Conference (ACC)*, 2015, pp. 3467-3472.

7. A. Abdollahi, N. Raghunathan, X. Han, B. Pattipati, B. Balasingam, K. R. Pattipati, Y. Bar-Shalom, and B. Card, "Battery health degradation and optimal life management," in *Proc. IEEE AUTOTESTCON*, 2015, pp. 146-151.

8. B. Pattipati, B. Balasingam, A. Abdollahi, G. V. Avvari, K. R. Pattipati, and Y. Bar-Shalom, "Integrated battery fuel gauge and optimal charger," In *Proc. IEEE AUTOTESTCON*, 2014, pp. 260-269.

1.2 Optimal Battery Charging and Battery Life Management

1.2.1 Motivation

The ever-increasing market for battery-operated smart devices and electric vehicles is a catalyst for the efficient operation and health monitoring of batteries. In this vein, researchers address this challenge, broadly, in two ways: optimal battery charging and life cycle management. The latter requires the tracking of battery capacity. Although the literature abounds with different charging methods and different capacity modeling approaches (see the following subsection), to the best of our knowledge, no general framework exists that considers both charging and life management of a battery. In this thesis, this integrated battery charging and battery life management will be discussed and a two-level algorithm for solving the problem is proposed.

1.2.2 Related Work

There are different approaches for charging batteries in the literature, including: traditional methods of charging such as the constant trickle current charge strategy, constant-current constant-voltage (CC-CV) [51], multi-step constant-current charging [115], Taguchi-based methods [116, 187], boost charging [132], pulse-charging [153, 41, 42, 113], ant-colony based optimization of multistage constant current strategy [117], optimal-control based approaches[77], neural network [148], Grey-predicted charging system [43]. For a review of different charging methods, the interested reader may consult [51], [102], [39], [175].

There are a number of capacity models in the literature, including bi-

exponential [82], physics-based electrochemical [114], [160], [152], and methods that are based on support vector machines [136], relevance vector machines (RVM) [162], sample entropy-based [85], extended Kalman filter [150], weighted total least squares [151], and SOC lookup [59]. A robust real time capacity estimation approach based on recursive least squares, total least squares, and OCV lookup has been proposed in [21]. A good review of several capacity estimation techniques can be found in [201]. For more information on capacity fade, the interested reader may refer to [14], [205].

1.2.3 Challenges

One challenge in finding the optimal charging profile is that batteries are nonlinear systems. The open-circuit voltage (OCV) of a battery is a nonlinear function of the state-of-charge (SOC) of the battery. Another challenge is controlling the capacity fade due to a charging profile. Capacity of a battery decreases with usage and the amount of capacity fade depends on how the battery is charged and discharged. While the discharge is out of designer's control, the charging profile can be controlled. For example, if the battery is charged with a low-level of current, its capacity fades more slowly over time compared to a battery with the same characteristics, but charged with high levels of current. The former requires longer charging times, while the latter shortens the charging time at the cost of decreased battery life. A challenge in finding the optimal charging profile is how to strike a balance between the speed of charge and the life of a battery.

1.2.4 Approach and Results

In this thesis, we investigate a two-level control strategy for combined optimal battery charging and battery life management. The low-level (level-II) deals with the problem of optimally charging the battery, given the control parameters of charging, viz., the maximum allowable current and the maximum allowable terminal voltage. A combination of different cost functions is considered including: time-to-charge, energy loss, and temperature rise index. For the battery, equivalent electrical circuit models are considered [20, 21]. At the higher level of optimization (level-I), we consider the optimal selection of control parameters of the charging process (maximum allowable current and maximum allowable terminal voltage). These parameters greatly affect the life of the battery. As a precursor to the level-I optimization strategy, we present two models of normalized battery capacity (or, equivalently, capacity fade), one of which as a function of the number of cycles and the two charge control parameters. In the level-I optimization, we develop an algorithm for selecting the setpoints for the control variables to achieve a pre-specified desired "useful cycle life", while attaining the fastest possible time-to-charge. This work was published in [5, 6, 11, 9, 10].

1.3 Multiple Fault Diagnosis using Probabilistic Graphical Models

1.3.1 Motivation

Reliability is essential to system availability and critical to system performance, and it is achieved in two phases: in design and development via design for performance reliability

and testability, and during system operation via fault diagnosis and maintenance. Design process aims at increasing product performance and reliability, while reducing the cost and time-to-market. The performance and reliability goals conflict with the the need to reduce cost and time-to-market, and this imposes a trade-off on how reliability and performance are achieved. Market pressures restrict the extent to which reliability can be achieved during system design; after-market services, such as efficient fault diagnosis, prognosis and condition-based maintenance, represent additional strategies to improve system availability. The latter strategies are assuming greater significance as systems are becoming complex with larger numbers of interacting components and are networked with the attendant cross-subsystem fault propagation. As a result, accurate methods of fault detection, diagnosis, and prognosis are in high demand in industry.

1.3.2 Related Work

Traditional approaches to fault detection and isolation, as discussed in [191], include "failure-sensitive" filters [101], [97], voting systems (for systems with a high degree of redundancy in parallel hardware), multiple hypothesis filter-detectors [111], [15], [49], jump process techniques [35], [34], and innovation-based detection systems [122], [124], [165], [79], [192].

Data-driven approaches to FDD are used when the system models are unavailable, but adequate data monitoring is available. Such systems are frequently used when vendors of subsystems do not provide the details of the internal functioning of their products in order to protect their intellectual property. To circumvent this lack of product details, data-driven approaches utilize substantial monitoring data in

order to train a model that satisfactorily represents the black-box system. Recursive identification [118], neural networks [68], [32] and machine learning methods [177], [159] are among the data-driven techniques.

Knowledge-based approaches to FDD require qualitative models for process monitoring and are used when mathematical models are unavailable. Most knowledge-based techniques are based on causal analysis, expert systems, and/or ad hoc rules. Because of the qualitative nature of these models, knowledge-based approaches have been applied to many complex systems. Graphical models, such as Petri nets, multi-signal flow graphs and Bayesian networks [177], are applied for diagnostic knowledge representation and inference in complex systems. Bayesian Networks subsume the deterministic fault diagnosis models embodied in the Petri net and multi-signal models.

The model based, data-driven and knowledge-based approaches provide the "sand box" that test designers can use to experiment with, and systematically select relevant models or combinations thereof, to satisfy the requirements on diagnostic accuracy, computational speed, memory, on-line versus off-line diagnosis, and so on. Ironically, no single technique can serve as the diagnostic approach for complex systems. Thus, an integrated diagnostic process that naturally employs data-driven techniques, graph-based dependency models and mathematical/physical models is necessary for fault diagnosis, thereby enabling efficient maintenance of these systems. The probabilistic graphical models provide such an integrating platform.

1.3.3 Challenges

The process of detecting and isolating faults in complex systems is challenging, because:

- The numbers of faults and monitoring signals ("processed sensor measurements",

"tests", "symptoms", "visual observations") in these systems are large (running into tens of thousands).

- Each test outcome may be caused by faults in multiple components of possibly multiple subsystems ("many-to-many" fault-test relationships).
- Faults propagate from one subsystem to another ("cross-subsystem fault propagation") with delays.
- The combination of failure sources leads to combinatorial explosion in an exhaustive search for failure sources, which is impractical in real-world problems.
- Test outcomes, which are uncertain, are observed with delays caused by fault propagation, computation and communication.
- Simultaneous occurrence of multiple faults is frequent.

This makes traditional single-fault diagnosis approaches untenable. Uncertain test outcomes pose particularly difficult challenges to fault diagnosis: while, in a perfect binary test outcome situation, a passed test indicates the normal status of its associated components and a failed test implies the existence of at least one faulty component associated with the test, neither can be inferred when the tests are imperfect.

1.3.4 Approach and Results

We address the multiple fault diagnosis using probabilistic graphical models in which the failure sources have probabilistic cause-effect relations with the test outcomes. These are performed using the detection and false alarm probabilities (DFA test model). Also, we show that the DFA test model and the leaky noisy OR (LNOR) test model

are two different ways of representing the same uncertain test outcome phenomena. A unified test model is proposed to include both the LNOR and the logistic regression (LR) test models. The maximum *a prosteriori* inference for multiple fault diagnosis is derived for the unified test model and it is extended for fault prognosis. This work was published in [11, 7]. Additional publication is planned [8].

1.4 Contributions and Research Impact

The primary contributions of this thesis are:

1. Deriving a closed form solution for determining the optimal battery charging profile to minimize a weighted sum of time-to-charge and energy loss;

2. Proving that for an OCV-Resistance battery model, CC-CV is the optimal solution with respect to an objective function, composed of linear combination of time-to-charge and energy-loss.

3. Deriving a semi-closed form solution for optimal battery charging profile by adding the temperature rise index to the cost function;

4. Showing that the effect of temperature rise can be approximated as an equivalent heating resistance;

5. Deriving the optimal battery charging profile for general equivalent electrical circuit models as a linear quadratic - constant voltage (LQ-CV) strategy;

6. Deriving two new battery capacity fade models that are shown to be statistically superior to the bi-exponential capacity fade model.

7. Developing an optimal charging parameter selection method for selecting the best settings for the control variables to achieve a desired "useful cycle life", while attaining the fastest possible time-to-charge;

8. Proving the equivalence of the Detection-False Alarm (DFA) and the Leaky Noisy OR (LNOR) test models;

9. Introducing a unified test model to include both the LNOR and the logistic regression (LR) test models;

10. Solving the maximum *a posteriori* (MAP) inference problem associated with the unified test model;

11. Deriving a dual cost function for the fault diagnosis problem both in the DFA test model and in the unified test model.

12. Developing an algorithm for fault prognosis in systems using the unified test model.

The broader impacts of this thesis are as follows:

1. Minimizing the life cycle cost of systems;

2. Enhancing the safety and reliability of systems;

3. Improving customer satisfaction through enhanced system availability;

4. Utility in a large number of applications, including automotive systems, aerospace systems, electrification of transportation, medical equipment, smart buildings/smart grid, and communication networks, to name a few.

Chapter 2

Optimal Battery Charging

2.1 Introduction

Battery charging is a problem of significant interest, especially as the battery-dependent smart devices proliferate.The literature abounds with different strategies for charging batteries. Among the traditional methods of charging, the simplest is the constant trickle current charge strategy, which, due to its low charging current, requires a long charging time (around 10 hours) [51]; constant current strategy with higher rates of current requires shorter charging time. The most widely-used traditional strategy is the constant-current constant-voltage (CC-CV) [51] strategy, in which a constant current is applied to the battery until the terminal voltage reaches a specified value, and afterwards the charging current decreases by applying a constant voltage to the terminals of the battery. In [89, 88], a multi-step constant-current charging is devised for shortening the charging time and prolonging the cycle life of the battery. Using orthogonal arrays, Taguchi-based methods for battery charging [116, 188] present

a systematic method to find the optimal solution with guidelines for choosing the design parameters. In [132], a boost charging strategy is proposed by applying very high currents to close-to-fully discharged batteries. In pulse-charging methods [153, 202, 41, 42, 113], the battery is exposed to very short rest or even deliberate discharging periods during the charging process. Soft-computing approaches are also used in the optimization of battery charging profile. In [117], the charging problem is viewed as an optimization problem with the objective function of maximizing the charge within 30 minutes using a multistage constant current charging algorithm whose optimal solution is obtained via an ant-colony approach. In [77], a universal voltage protocol is proposed to improve charging efficiency and cycle life by applying a charging profile depending on the state-of-health (SOH) of the battery, using SOH estimation approaches [78] in the optimization process. Recently, in [84], battery charging is considered as an optimization problem with cost function of time-to-charge and energy loss (as we do in this paper), but they have not solved the problem analytically; rather they have presented a numerical solution to the problem. Other approaches, such as genetic algorithm and neural network based strategies [148], data mining [12, 76], Grey-predicted charging system [43] have also been used for charging batteries.

In this chapter, we look at the charging problem from a fresh perspective using optimal control theory, and our goal is to find the optimal current profile that minimizes a specific cost function. In this sense, different objectives may be embedded in the cost function. One obvious cost function is the time-to-charge (TTC). We prefer to minimize the charging time as much as possible, as TTC reduction contributes to user satisfaction. Another important objective is the energy loss (EL) during charging. Reducing the energy loss increases the charging efficiency. In this paper, first we

use an integrated cost function that includes both the TTC and EL. Then, we also include the effects of temperature into account, and the cost function is selected as a linear combination of three criteria: time-to-charge, energy loss, and temperature rise index (TRI). In both cases, analytical solutions of the optimal charging problem are derived, when the battery model is considered as an Open-Circuit Voltage (OCV) and a resistance. When more complex models are adopted for the battery, we can no longer obtain an analytic solution, but we can find a numerical algorithm to provide the optimal charging profile.

This chapter is organized as follows. In section 2.2, we derive an analytical solution for the optimal charging current profile to minimize TTC and EL, for OCV-Resistance model (referred to here as Model I). In section 2.3, we extend this approach to the case where temperature rise is considered as well. In section 2.4, we we derive the optimal charging profile, which is called LQ-CV (Linear QuadraticConstant Voltage), for a general equivalent electrical model of battery. Section 2.5 is devoted to simulation results and finally we summarize the chapter in section 2.6.

2.2 Analytic Solution for Optimal Charging Current Profile for OCV-Resistance Model

We consider a simplified equivalent electrical circuit model of the battery as shown in Fig. 2.2.2. The theory extends naturally to more complex models involving parallel RC elements (shown in Fig. 2.2.3), but, as we will discuss in section 2.4, the analytical closed form solutions are not possible in the latter case. The model consists of a voltage source corresponding to the open-circuit voltage (OCV), which is dependent on the state of charge (SOC), and a resistance R_0. The SOC is denoted by s. The

equivalent electrical circuit models in Fig. 2.2.2 and Fig. 2.2.3, in this dissertation, are termed "model I" and "model II", respectively, for the sake of consistency with previous publications [20]. The OCV is a nonlinear function of SOC and is denoted by OCV $(s[k])$. In [20], OCV-SOC function is described as follows:

$$s_{\mathrm{s}} \triangleq E + s(1 - 2E) \tag{2.2.1}$$

$$OCV(s_{\mathrm{s}}) = K_0 + K_1 s_{\mathrm{s}}^{-1} + K_2 s_{\mathrm{s}}^{-2} + K_3 s_{\mathrm{s}}^{-3} + K_4 s_{\mathrm{s}}^{-4} + K_5 s_{\mathrm{s}} + K_6 \ln(s_{\mathrm{s}}) + K_7 \ln(1 - s_{\mathrm{s}}) \tag{2.2.2}$$

and $E = 0.15$. Note that the scaling of SOC in (2.2.1) is performed for numerical stability. For example, if $s = 0$, then $\ln(s)$ equals negative infinity, if the scaling is not used. K_0 through K_7 are some constants.

Figure 2.2.1 depicts the OCV curve as a function of SOC for several commercial batteries.

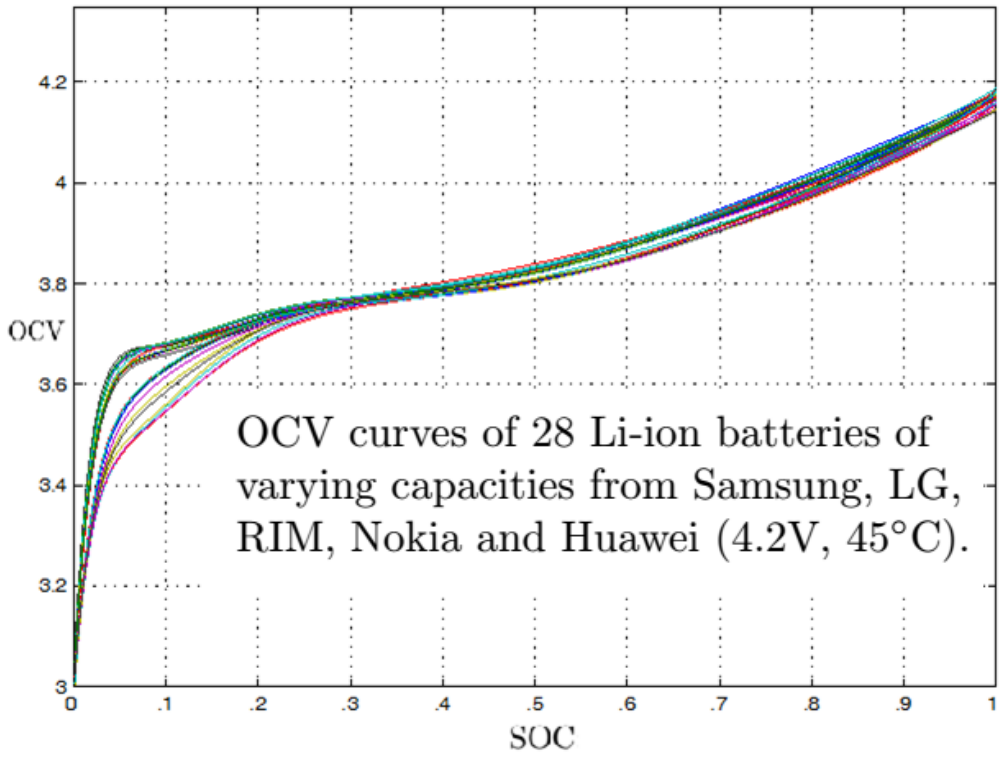

FIGURE 2.2.1: OCV curve as a function of SOC

The state of charge is zero when the battery is totally discharged and it is one if it is completely charged. The sampling time is denoted by Δ (in seconds). We assume that the initial and final SOC are known: $s[0] = s_0$, $s[k_f] = s_{k_f}$, where $k_f\Delta$ is the charging time. We also assume that the maximum allowed value of the terminal charging voltage is v_c, that is, $v[k] \leq v_c$ for all k. In this thesis, we consider charging current as positive and discharging current as negative.

The SOC dynamics for the battery considering the foregoing model are as follows:

$$s[k+1] = s[k] + c_h i[k] \tag{2.2.3}$$

where c_h (in 1/Amperes) is the parameter in Coulomb counting, given by

$$c_h = \frac{\Delta}{3600Q} \tag{2.2.4}$$

where Q (in Ah) is the battery capacity, assumed to be known.

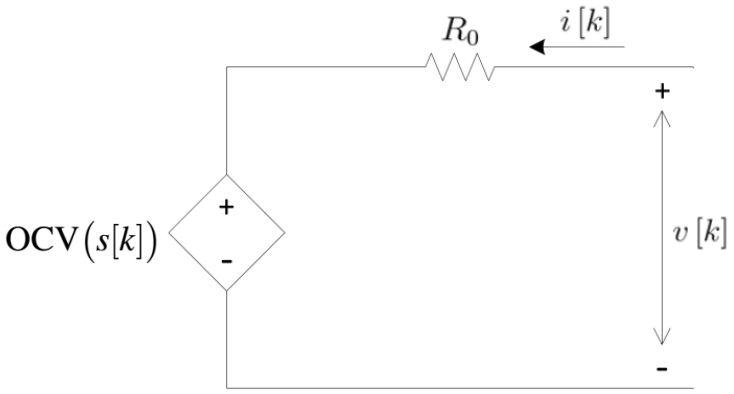

FIGURE 2.2.2: Equivalent electrical circuit model I of battery

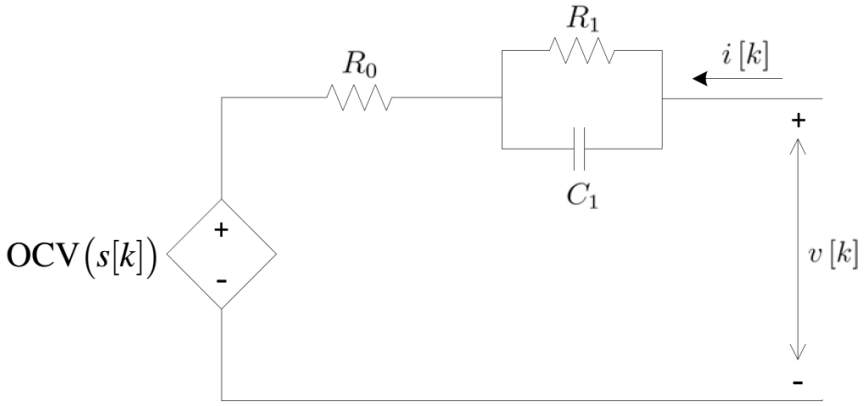

FIGURE 2.2.3: Equivalent electrical circuit model III of battery

Let the objective function be a combination of TTC and EL. In other words,

$$\tilde{J}_{\mathrm{tE}} = w_{\mathrm{t}} J_{\mathrm{t}} + w_{\mathrm{E}} J_{\mathrm{E}} = w_{\mathrm{t}} k_f \Delta + w_{\mathrm{E}} \sum_{k=0}^{k_f-1} R_0 i^2[k] \Delta \tag{2.2.5}$$

where J_{t} is the TTC cost function, J_{E} is the EL cost function; w_{t} and w_{E} are weights on the TTC and EL cost functions, respectively. The resistance of the battery, i.e., R_0, is assumed to be known.

The charging problem then could be formulated as follows:
Minimize $\tilde{J}_{\mathrm{tE}}$ subject to:

$$s[k+1] = s[k] + c_h i[k] \quad s[0] = s_0 \quad s[k_f] = s_{k_f} \tag{2.2.6}$$

$$\mathrm{OCV}\left(s[k]\right) + R_0 i[k] \leq v_{\max} \tag{2.2.7}$$

$$i[k] \leq i_{\max} \tag{2.2.8}$$

It is important to note that only the ratio of weights affects the optimal current profile of $i[k]$. Therefore, by dividing (2.2.5) by w_{E}, we redefine the cost function as follows:

$$J_{\mathrm{tE}} = \tilde{J}_{\mathrm{tE}}/w_{\mathrm{E}} = \rho_{\mathrm{t}} J_{\mathrm{t}} + J_{\mathrm{E}} = \rho_{\mathrm{t}} k_f \Delta + \sum_{k=0}^{k_f-1} R_0 i^2[k] \Delta \tag{2.2.9}$$

where $\rho_{\mathrm{t}} = w_{\mathrm{t}}/w_{\mathrm{E}}$. Also note that when the current is injected into the battery, the OCV starts to increase and this, in turn, causes the terminal voltage to rise, until it reaches $v_{\max}$, which is the maximum allowed terminal voltage. During the whole charging process the current should not exceed $i_{\max}$, which is the maximum allowed charging current. Selecting the optimal values of $i_{\max}$ and $v_{\max}$ is discussed in chapter

4. In this chapter, we use v_c for $v_{\max}$, where v_c is the voltage corresponding to SOC of 1; that is

$$v_c = \mathrm{OCV}(1) \tag{2.2.10}$$

Assume that at time k_1, the terminal voltage $v[k_1]$ reaches v_c and let us denote the state of charge at time k_1 as s_1. After time k_1, the terminal voltage should be fixed at the constant voltage (CV) v_c; hence, for $k = k_1, k_1 + 1, ..., k_f - 1$, the dynamics of the system are as follows:

$$i[k] = \frac{1}{R_0}(v_c - \mathrm{OCV}(s[k])) \tag{2.2.11}$$

$$s[k+1] = s[k] + c_h i[k] \tag{2.2.12}$$

$$s[k_1] = s_1 \quad s[k_f] = s_{k_f} \tag{2.2.13}$$

Before going further, let us define a new equivalent problem as follows: Minimize

$$J_{\mathrm{tE}} = \rho_{\mathrm{t}} J_{\mathrm{t}} + J_{\mathrm{E}} = \rho_{\mathrm{t}} k_1 \Delta + \sum_{k=0}^{k_1 - 1} R_0 i^2[k] \Delta \tag{2.2.14}$$

subject to:

$$s[k+1] = s[k] + c_h I[k] \quad s[0] = s_0 \quad s[k_1] = s_1 \tag{2.2.15}$$

This problem is in fact the minimization in the stage where the terminal voltage is below v_c and therefore here the condition $\text{OCV}\,(s[k]) + R_0 I[k] \leq v_c$ is not shown as we know that it holds.

Inspired by [186] and [60], we solve the problem in three steps as described below:

❶ Given k_1 (when the terminal voltage constraint becomes active), find the optimal current profile that minimizes the energy losses, and calculate the corresponding energy losses as a function of k_1.

❷ Generate a new equivalent cost function J_{tE^*} consisting of the weighted TTC plus the k_1-dependent minimum energy loss obtained in step 1, and find the optimal k_1 based on this cost function.

❸ Given the optimal k_1 from step 2, evaluate the optimal current obtained in step 1.

In the first step, assuming k_1 is known, we find the optimal current $i^*[k|k_1]$ that minimizes the energy loss. Having this optimal current profile, we can calculate the minimum EL cost function $J^*_{\text{E}}(k_1)$, which is a function of k_1. In the second step, we use the partially optimized cost function $J_{\text{tE}^*} = \rho_{\text{t}} k_1 \Delta + J^*_{\text{E}}(k_1)$ and we find the optimum value for k_1, say k_1^*. In the third step, we insert the optimal final time k_1^* into the current $i^*[k|k_1]$ (obtained in step 1) to find the optimal current $i^*[k]$. Inserting

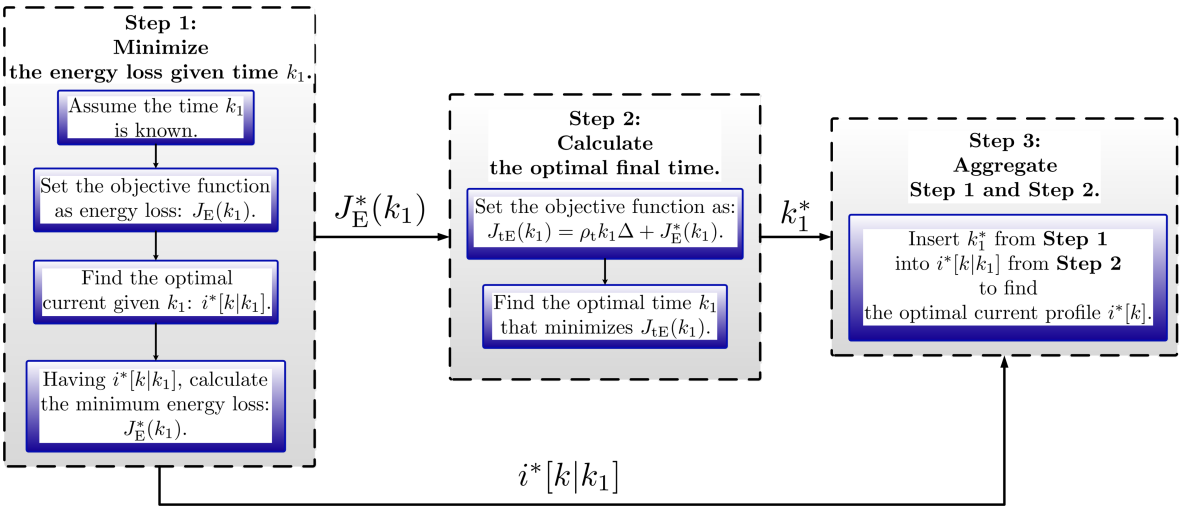

FIGURE 2.2.4: Minimization of time and energy loss

$i^*[k]$ into the cost function, one can calculate $J^*_{\mathrm{tE}}(k_1^*)$. Figure 2.2.4 illustrates the above three steps. In Fig. 2.2.4, think of k_1 as the final time, and consider the problem of minimizing a "combination of time and energy loss".

Note that, given k_1, the term $\rho_{\mathrm{t}} k_1 \Delta$ in (2.2.14) is constant and can be dropped; therefore, the first stage is formulated as follows:

Minimize

$$J_{\mathrm{E}}(k_1) = \sum_{k=0}^{k_1-1} R_0 i^2[k]\Delta \tag{2.2.16}$$

subject to

$$s[k+1] = s[k] + c_h i[k] \quad s[0] = s_0 \quad s[k_1] = s_1 \tag{2.2.17}$$

The Hamiltonian function for this problem is

$$H[k] = R_0 i^2[k]\Delta + \lambda[k+1](s[k] + c_h i[k]) \tag{2.2.18}$$

The following equations must hold for the optimal solution [30]:

$$\frac{\partial H[k]}{\partial i[k]} = 0 \tag{2.2.19}$$

$$\lambda[k] = \frac{\partial H[k]}{\partial s[k]} \tag{2.2.20}$$

$$s[k+1] = \frac{\partial H[k]}{\partial \lambda[k+1]} \tag{2.2.21}$$

From (2.2.19) we have

$$i^*[k] = -\frac{c_h \lambda[k+1]}{2R_0\Delta} \quad k = 0, 1, ...k_1 - 1 \tag{2.2.22}$$

From (2.2.20), we can write

$$\lambda[k] = \lambda[k+1] \quad k = k_1 - 1, ..., 0 \quad \lambda[k_1] = \nu \tag{2.2.23}$$

where ν is the Lagrange multiplier associated with the constraint $s[k_1] = s_1$. Equation

(2.2.23) implies that all co-states are equal; therefore, we can write

$$\lambda[k] = \nu \quad k = 0, 1, ...k_1 \tag{2.2.24}$$

Based on (2.2.24), equation (2.2.22) can be written as

$$i^*[k] = -\frac{c_h \nu}{2R_0\Delta} \quad k = 0, 1, ..., k_1 - 1 \tag{2.2.25}$$

Note that equation (2.2.25) states that the optimal current is constant. From (2.2.21), we can write

$$s[k+1] = s[k] + c_h i[k] \tag{2.2.26}$$

which is actually the dynamics of the system. Knowing the initial state of charge (s_0), and noting the optimal current in (2.2.25) is constant, we have

$$s[k] = s_0 + c_h \sum_{l=0}^{k-1} i[l] = s_0 - \frac{k c_h^2 \nu}{2R_0\Delta} \tag{2.2.27}$$

Since for $k = k_1$, we have $s[k_1] = s_1$, therefore

$$s_1 = s_0 - \frac{k_1 c_h^2 \nu}{2R_0\Delta} \tag{2.2.28}$$

Solving for ν, we have

$$\nu = -\frac{2R_0\Delta(s_1 - s_0)}{k_1 c_h^2} \tag{2.2.29}$$

Inserting (2.2.29) into (2.2.25), we have

$$i^*[k] = \frac{s_1 - s_0}{k_1 c_h} \quad k = 0, 1, ..., k_1 - 1 \tag{2.2.30}$$

Inserting (2.2.30) into the cost function, the optimal cost function, given k_1 is:

$$J_{\mathrm{E}}^*(k_1) = \sum_{k=0}^{k_1-1} R_0 \left(\frac{s_1 - s_0}{k_1 c_h} \right)^2 \Delta = \frac{R_0 \Delta (s_1 - s_0)^2}{k_1 c_h^2} \tag{2.2.31}$$

Now, consider step 2 and define the cost function as

$$J_{\mathrm{tE}^*} = \rho_{\mathrm{t}} k_1 \Delta + J_{\mathrm{E}}^*(k_1) = \rho_{\mathrm{t}} k_1 \Delta + \frac{R_0 \Delta (s_1 - s_0)^2}{k_1 c_h^2} \tag{2.2.32}$$

To find the optimum k_1, the following relations should hold:

$$J_{\mathrm{tE}^*}(k_1 - 1) \geq J_{\mathrm{tE}^*}(k_1) \tag{2.2.33}$$

$$J_{\mathrm{tE}^*}(k_1 + 1) \geq J_{\mathrm{tE}^*}(k_1) \tag{2.2.34}$$

Inserting (2.2.32) into (2.2.33) and (2.2.34) we obtain two second-order equations in term of k_1. Solving these equations, we get k_1^- and k_1^+, respectively, for relations (2.2.33) and (2.2.34).

$$k_1^{\mp} = \frac{\pm 1 + \sqrt{1 + \frac{4R_0(s_1 - s_0)^2}{\rho_{\mathrm{t}} c_h^2}}}{2} \tag{2.2.35}$$

The optimum k_1 is ceil(k_1^-) or floor(k_1^+). Since $k_1^- - k_1^+ = 1$, we have ceil(k_1^-) =

$\text{floor}(k_1^+) = \text{round}((k_1^- + k_1^+)/2)$. Thus,

$$k_1^* = \text{round}\left(\sqrt{\frac{1}{4} + \frac{R_0(s_1 - s_0)^2}{\rho_{\text{t}} c_h^2}}\right) \tag{2.2.36}$$

A more convenient way is to treat k_1 in (2.2.32) as a continuous variable and take derivative of (2.2.32) with respect to k_1 as follows:

$$\frac{\partial J_{\text{tE}^*}(k_1)}{\partial k_1} = \rho_{\text{t}}\Delta - \frac{R_0\Delta(s_1 - s_0)^2}{k_1^2 c_h^2} = 0 \tag{2.2.37}$$

$$k_1^* = \frac{s_1 - s_0}{c_h}\sqrt{\frac{R_0}{\rho_{\text{t}}}} \tag{2.2.38}$$

Note that if we neglect $\frac{1}{4}$ in (2.2.36), the argument of the rounded function in (2.2.36) is exactly the same as the one in (2.2.38).

Step 3 involves inserting (2.2.38) into (2.2.30) to find the optimum current

$$i^*[k] = \frac{s_1 - s_0}{k_1^* c_h} = \sqrt{\frac{\rho_{\text{t}}}{R_0}} \quad k = 0, 1, ..., k_1 - 1 \tag{2.2.39}$$

Remark 2.2.1. If we put more emphasis on TTC (i.e., we increase ρ_{t}), the optimal current increases and TTC decreases. For an animation of the effect of ρ_{t} on the optimal current, the reader may refer to [1].

Remark 2.2.2. When a battery ages, it experiences power fade which is equivalent to increasing the series resistance in the battery. Increasing the series resistance (i.e., R_0) results in a decrease in the optimal current and TTC increases. For an animation of the effect of power fade (increasing R_0) on the optimal current, the reader may

refer to [1].

It is seen that the optimal current is constant and is a function of the weight on TTC and the series resistance. Therefore, the solution of optimal time-to-charge and energy loss (OtE) problem is a CC-CV profile with the current of the CC stage given by (2.2.39). Following the CC stage, from k_1 to k_f, one has the CV stage where

$$v[k] = v_c \quad k = k_1, ..., k_f \tag{2.2.40}$$

To the best of our knowledge, this is the first time that it is proved that the well-known CC-CV charging profile is the optimal solution of a particular optimization problem, namely, the problem of minimizing the weighted sum of time-to-charge and energy loss for the OCV-Resistance model in Fig. 2.2.2.

In the sequel, this profile is referred to as OtE profile or OtE policy.

Before we close this section, we point out another way of solving the OtE problem of (2.2.14)-(2.2.15) by condensing (2.2.15) for all values of k into a single condition. From (2.2.15) we can write

$$i[k] = \left(s[k+1] - s[k]\right)/c_h \tag{2.2.41}$$

Since (2.2.41) holds for $k = 0, 1, ..., k_1 - 1$, and using the initial and end values of SOC from (2.2.15) we can write:

$$\sum_{l=0}^{k_1-1} i[l] = (s_1 - s_0)/c_h \tag{2.2.42}$$

Therefore, the problem of (2.2.14)-(2.2.15) is equivalent to a quadratic pro-

gramming problem with the constraint in (2.2.42). In this way, we are dealing with currents $i[l]$ as our unknowns. It is easy to show that this results in the same solution as (2.2.39). This simplification of the dynamics of the system into the condensed condition of (2.2.42) will be useful in the next section where we derive an analytical solution when the cost function includes the summation of temperature rises as well.

It should be noted that the practical meaning of the parameters of optimization problem (e.g., w_{t} and w_{E} in (2.2.5) and ρ_{t} in (2.2.14)) is to use them in an iterative design procedure to reach the desired performance. For example, if the maximum energy loss is $E_{\max}$ and the maximum time-to-charge is $TTC_{\max}$, then in the design procedure, w_{t} and w_{E} should be selected inversely proportional to $E_{\max}$ and $TTC_{\max}$, respectively; that is $w_{\mathrm{t}} \propto \frac{1}{TTC_{\max}}$, $w_{\mathrm{E}} \propto \frac{1}{E_{\max}}$ and then iterate. Or equivalently, ρ_{t} should be selected proportional to $\frac{E_{\max}}{TTC_{\max}}$; that is $\rho_{\mathrm{t}} \propto \frac{E_{\max}}{TTC_{\max}}$ and then iterate on the proportionality factor. As $\frac{E_{\max}}{TTC_{\max}}$ is actually the power loss, ρ_{t} should be selected proportional to power loss.

2.3 Optimal Charging Problem Considering Temperature

In this section, we will extend the cost function to include the battery temperature via temperature rise index (TRI, to be defined) as well as TTC and EL. To this end, we need a temperature model for the battery. The reader may refer to the "Appendix B" for details of temperature modeling. References [146] and [198] describe the temperature model of the battery as a linear system with two states, namely, T_{core} and T_{air}, and reference [147] uses the nonlinear heat transfer equation with a single state. Our simulations show that the dynamics of T_{air} have negligible fluctuations

around the ambient temperature. Therefore, the temperature model, considered below, can be simplified to the linear part of the heat transfer equation

$$T[k+1] = T[k] - a(T[k] - T_{\text{amb}}) + bi^2[k] \tag{2.3.1}$$

where

$$a = \frac{\Delta}{m_{\text{batt}} C_{h,\text{batt}} R_{\text{Eff}}} \tag{2.3.2}$$

is the cooling coefficient and

$$b = \frac{R_0 \Delta}{m_{\text{batt}} C_{h,\text{batt}}} \tag{2.3.3}$$

Here, T is the battery core temperature in kelvin (K), T_{amb} is the ambient temperature in K, m_{batt} is the battery mass in kg, $C_{h,\text{batt}}$ is the heat capacity of the battery in J/(kg $\cdot$ K), and R_{Eff} is the effective thermal resistance in K/W (kelvin/watt).

Defining temperature rise (TR) as $\tilde{T}[k] = T[k] - T_{\text{amb}}$ and assuming $T[0] = T_{\text{amb}}$, we can write

$$\tilde{T}[k+1] = (1-a)\tilde{T}[k] + bi^2[k], \qquad \tilde{T}[0] = 0 \tag{2.3.4}$$

The solution of (2.3.4) is

$$\tilde{T}[k] = b \sum_{l=0}^{k-1} (1-a)^{k-1-l} i^2[l] \tag{2.3.5}$$

Equation (2.3.5) states that the temperature rise at any time is the integral of the

square of current, from time zero up to that time with a "forgetting factor" of $(1-a)$ and the scaling factor b.

Since $\tilde{T}[k]$ is positive for any k, the cost function including TTC, EL and TR can be written as

$$J_{\mathrm{tET}} = \rho_{\mathrm{t}} J_{\mathrm{t}} + J_{\mathrm{E}} + \rho_{\mathrm{T}} J_{\mathrm{T}} \tag{2.3.6}$$

where J_{t} and J_{E} are TTC and EL as before and J_{T} is the temperature rise index (TRI) defined as follows:

$$J_{\mathrm{T}} = \Delta \sum_{k=0}^{k_f} \tilde{T}[k] \tag{2.3.7}$$

Since $\tilde{T}[0] = 0$, the TRI can be written as

$$J_{\mathrm{T}} = \Delta \sum_{k=0}^{k_f-1} \tilde{T}[k+1] \tag{2.3.8}$$

Using (2.3.5) and (2.3.8), we can write (2.3.6) as follows

$$\begin{aligned} J_{\mathrm{tET}} &= \rho_{\mathrm{t}} k_f \Delta + \sum_{k=0}^{k_f-1} R_0 i^2[k] \Delta \\ &+ \rho_{\mathrm{T}} b \Delta \sum_{k=0}^{k_f-1} \sum_{l=0}^{k} (1-a)^{k-l} i^2[l] \Delta \end{aligned} \tag{2.3.9}$$

which can be simplified as follows

$$J_{\mathrm{tET}} = \rho_{\mathrm{t}} k_f \Delta + \Delta \sum_{k=0}^{k_f-1} \left(R_0 + \rho_{\mathrm{T}} b \sum_{l=0}^{k_f-k-1} (1-a)^l \right) i^2[k] \tag{2.3.10}$$

Simplifying the inner summation and noting that $b/a = R_0 R_{\mathrm{Eff}}$, we can write

$$J_{\mathrm{tET}} = \rho_{\mathrm{t}} k_f \Delta + \Delta \sum_{k=0}^{k_f-1} R_{\mathrm{eq}}[k] i^2[k] \tag{2.3.11}$$

$$R_{\mathrm{eq}}[k] = R_0 + R_{\mathrm{T}}[k] \tag{2.3.12}$$

$$R_{\mathrm{T}}[k] = \rho_{\mathrm{T}} R_0 R_{\mathrm{Eff}} \left(1 - (1-a)^{k_f-k}\right) \tag{2.3.13}$$

where $R_{\mathrm{T}}[k]$ is the heating equivalent resistance. Assume, as before, that at time k_1, the terminal voltage v reaches its maximum allowable value of v_c, and SOC reaches s_1. Given s_1 and k_1, we can write the cost function as

$$J(s_1, k_1) = \Delta \sum_{k=0}^{k_1-1} R_{\mathrm{eq}}[k] i^2[k] \tag{2.3.14}$$

Note that we discarded the contributions of $i[k_1], ..., i[k_f - 1]$, because when the terminal voltage reaches v_c the current is already determined by the constrained dynamics of the system in (2.2.11); we also discarded the contribution of k_f, i.e. $\rho_{\mathrm{t}} k_f \Delta$, because: firstly, k_1 is given; secondly, given s_1, $k_f - k_1$ is also known, which means k_f is known. An important point to note is that, while the upper bound of the summation in (2.3.14) is $k_1 - 1$, the formulation for R_{eq}, i.e., (2.3.12), considers the

effect of the whole charging time and it contains k_f rather than k_1.

Now, given s_1 and k_1, we can state the optimal charging problem as follows: Minimize (2.3.14) subject to (2.2.42), or equivalently

$$\text{Minimize: } L = J(s_1, k_1) + \lambda \left(\sum_{l=0}^{k_1-1} i[l] - \frac{s_1 - s_0}{c_h} \right) \tag{2.3.15}$$

Taking the derivative of Lagrangian L with respect to $i[k]$ for $k = 0, 1, ..., k_1 - 1$ and equating it to zero, we have:

$$i[k] = -\frac{\lambda}{2R_{\text{eq}}[k]\Delta} = -\frac{\lambda G_{\text{eq}}[k]}{2\Delta} \tag{2.3.16}$$

where $G_{\text{eq}}[k] = 1/R_{\text{eq}}[k]$ is the conductance. Taking the derivative of L with respect to λ, and using (2.3.16) we find the optimal current profile in the first stage as follows:

$$i^*[k] = -\frac{G_{\text{eq}}[k]\,(s_1 - s_0)}{c_h \sum_{k=0}^{k_1-1} G_{\text{eq}}[k]} \quad k = 0, 1, ..., k_1 - 1 \tag{2.3.17}$$

We refer to the current profile in (2.3.17) as the optimal time-to-charge, energy losses and temperature rise (OtET) policy. Note that (2.3.17) is similar to what we obtained for the OtE case. In particular, if $\rho_{\text{T}} = 0$, then (2.3.17) will be the same as (2.2.30). Also, comparing (2.3.16) with the OtE case and, noting that for $k = 0, 1, ..., k_1 - 1$, we can use the approximation of $R_{\text{eq}}[k] \approx R_0(1 + \rho_{\text{T}} R_{\text{Eff}})$, analogous to the optimal current profile of (2.2.39), we can write

$$i^*[k] \approx \sqrt{\frac{\rho_{\text{t}}}{R_0(1 + \rho_{\text{T}} R_{\text{Eff}})}} \quad k = 0, 1, ..., k_1 - 1 \tag{2.3.18}$$

We refer to the current profile of (2.3.18) as the near-optimal time-to-charge, energy loss and temperature rise (NOtET) policy.

2.4 Linear Quadratic- Constant Voltage (LQ-CV) Strategy Formulation

In this section, we investigate the battery charging problem using the equivalent electrical circuit model (model III) shown in Fig. 2.4.1.

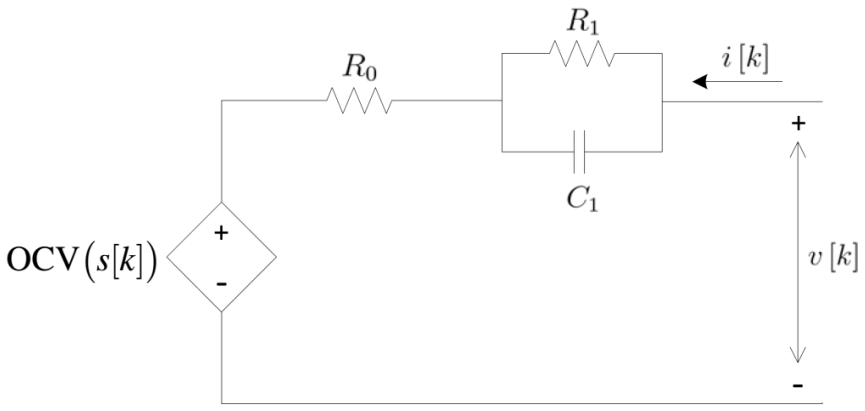

FIGURE 2.4.1: Equivalent electrical circuit model III of battery

Compared to the model discussed in subsection 2.2, it includes an extra RC circuit (R_1 and C_1). Let the current (in continuous time) through R_0 and R_1 be $i(t)$ and $i_1(t)$, respectively, and let the current through and the voltage across the capacitor C_1 be, respectively, $i_c(t)$ and $v_c(t)$. Then, we have: $i_c(t) = C_1 \frac{dv_c(t)}{dt}$, $i_c(t) = i(t) - i_1(t)$, $\frac{dv_c(t)}{dt} = R_1 \frac{di_1(t)}{dt}$, $\frac{di_1(t)}{dt} = \lim_{\Delta \longrightarrow 0} \frac{i_1(t+\Delta) - i_1(t)}{\Delta}$. Using these relations and inserting $\frac{1}{R_1} \lim_{\Delta \longrightarrow 0} \frac{\Delta}{1-\exp(-\Delta/(R_1 C_1))}$ for C_1, one can derive the following relation in

the discrete form:

$$i_1[k+1] = \alpha i_1[k] + (1-\alpha) i[k] \tag{2.4.1}$$

where $i_1[k]$ and $i[k]$ are $i_1(k\Delta)$ and $i(k\Delta)$, respectively; Δ is the sampling interval (typically 0.1 to 1 second, and assumed constant for simplicity of notation), and α is as follows:

$$\alpha = \exp(-\frac{\Delta}{R_1 C_1}) \tag{2.4.2}$$

The dynamic evolution of the battery state-of-charge (SOC), s, is given by

$$s[k+1] = s[k] + c_h i[k] \tag{2.4.3}$$

where $s[k]$ is the SOC at time k and c_h (in 1/Amperes) is the Coulomb counting coefficient, given by

$$c_h = \frac{\Delta}{3600Q} \tag{2.4.4}$$

where Δ is the time step (typically 0.1 to 1 second) and Q (in Ah) is the battery capacity, assumed to be known. It is assumed that the charging process takes $k_f\Delta$ seconds (k_f unknown and to be optimized), to attain a specified final desired SOC of s_{k_f}. That is,

$$s[k_f] = s_{k_f} \tag{2.4.5}$$

We consider a cost function composed of time-to-charge (TTC), energy loss (EL) in R_0 and R_1, and a temperature rise index (TRI). To have more flexibility in controlling the time to charge and the trajectory of SOC during charging, we also include a term including the sum of the squares of the difference of SOC at various times of the charging interval from the final desired SOC.

The cost function is, therefore, as follows:

$$J_{\mathrm{tEsT}} = \rho_{\mathrm{t}} J_{\mathrm{t}} + J_{\mathrm{E}} + \rho_{\mathrm{s}} J_{\mathrm{s}} + \rho_{\mathrm{T}} J_{\mathrm{T}} \tag{2.4.6}$$

where

$$J_{\mathrm{t}} = k_f \Delta \tag{2.4.7}$$

$$J_{\mathrm{E}} = \Delta \sum_{k=0}^{k_f - 1} (R_0 i^2[k] + R_1 i_1^2[k]) \tag{2.4.8}$$

$$J_{\mathrm{s}} = \sum_{k=0}^{k_f - 1} (s[k] - s_{k_f})^2 \tag{2.4.9}$$

$$J_{\mathrm{T}} = \Delta \sum_{k=0}^{k_f} \tilde{T}[k] \tag{2.4.10}$$

where $\tilde{T}[k]$ is the temperature rise from the ambient temperature, T_{amb}; that is

$$\tilde{T}[k] = T[k] - T_{\text{amb}} \tag{2.4.11}$$

Since it is the ratio of the weights that matters, we have assigned a weight of 1 to the energy loss cost function, i.e., J_{E}.

Remark 2.4.1. In (2.4.9), one can replace s_{k_f} with $s_{\text{d}}(k)$, the desired SOC at time step k, for the charging process to follow a desired sequence of SOCs $\{s_{\text{d}}(k)\}_{k=0}^{k_f}$.

Remark 2.4.2. The cost function can include other functions of the SOC and the method that we discuss is still applicable. One such candidate is the following term, which corresponds to sum of squares of cumulative SOC difference from the final desired SOC.

$$J_{\text{S}} = \sum_{k=0}^{k_f-1} \left(\sum_{l=0}^{k-1} (s[l] - s_{k_f}) \right)^2 \tag{2.4.12}$$

The temperature dynamics are as follows (For more details about thermal models refer to [5, 146, 198, 134, 147, 199, 206, 81]):

$$\tilde{T}[k+1] = (1-a)\tilde{T}[k] + b_0 i^2[k] + b_1 i_1^2[k] \tag{2.4.13}$$

where a is the cooling coefficient (see (B.0.21)). Note that equation (2.4.13) is similar to (2.3.4), except that here we have the effect of current i_1 too. The reader may refer to the "Appendix B" for details of temperature modeling.

$$b_0 = \frac{R_0 \Delta}{m_{\text{batt}} C_{h,\text{batt}}} \tag{2.4.14}$$

$$b_1 = \frac{R_1 \Delta}{m_{\text{batt}} C_{h,\text{batt}}} \tag{2.4.15}$$

and $C_{h,\text{batt}}$ is the heat capacity of the battery (see (B.0.21)). The solution of (2.4.13) is as follows:

$$\hat{T}[k] = \sum_{l=0}^{k-1} (1-a)^{k-1-l} (b_0 i^2[l] + b_1 i_1^2[l]) \tag{2.4.16}$$

Similarly to subsection 2.3, the cost function due to temperature, i.e., J_{T}, can be written as follows:

$$J_{\text{T}} = \Delta \sum_{k=0}^{k_f-1} \left(\left(\sum_{l=0}^{k_f-k-1} (1-a)^l \right) (b_0 i^2[l] + b_1 x^2[l]) \right) \tag{2.4.17}$$

Calculating the summation of $(1-a)^l$ and noting that $b_0/a = R_0 R_{\text{Eff}}$ and $b_1/a = R_1 R_{\text{Eff}}$, we can write

$$J_{\text{T}} = \Delta \sum_{k=0}^{k_f-1} R_{0\text{eq}}[k] i^2[k] + R_{1\text{eq}}[k] i_1^2[k] \tag{2.4.18}$$

$$R_{0\mathrm{eq}}[k] = R_0 + R_{0\mathrm{T}}[k] \tag{2.4.19}$$

$$R_{0\mathrm{T}}[k] = \rho_{\mathrm{T}} R_0 R_{\mathrm{Eff}} \left(1 - (1-a)^{k_f - k}\right) \tag{2.4.20}$$

$$R_{1\mathrm{eq}}[k] = R_1 + R_{1\mathrm{T}}[k] \tag{2.4.21}$$

$$R_{1\mathrm{T}}[k] = \rho_{\mathrm{T}} R_1 R_{\mathrm{Eff}} \left(1 - (1-a)^{k_f - k}\right) \tag{2.4.22}$$

where $R_{0\mathrm{T}}[k]$ and $R_{1\mathrm{T}}[k]$ are the heating equivalent resistances respectively due to R_0 and R_1. To simplify the equations, we define the following state vector:

$$\underline{z}[k] = \begin{bmatrix} s[k] - s_{k_f} \\ i_1[k] \end{bmatrix} \tag{2.4.23}$$

The dynamics of $\underline{z}[k]$ with its initial and final states could be written as follows:

$$\underline{z}[k+1] = \Phi \underline{z}[k] + \Gamma i[k] \tag{2.4.24}$$

$$\Phi = \begin{bmatrix} 1 & 0 \\ 0 & \alpha \end{bmatrix} \tag{2.4.25}$$

$$\Gamma = \begin{bmatrix} c_h, 1-\alpha \end{bmatrix}^T \tag{2.4.26}$$

$$\underline{z}[0] = \begin{bmatrix} s_0 - s_{k_f}, 0 \end{bmatrix}^T \tag{2.4.27}$$

$$\underline{z}[k_f] = \begin{bmatrix} 0, \text{free} \end{bmatrix}^T \tag{2.4.28}$$

The battery terminal voltage is then as follows:

$$v[k] = \text{OCV}\ (s[k]) + R_0 i[k] + \begin{bmatrix} 0 & R_1 \end{bmatrix} \underline{z}[k] \tag{2.4.29}$$

with following constraints:

$$v[k] \leq v_{\max} \tag{2.4.30}$$

$$i[k] \leq i_{\max} \tag{2.4.31}$$

Selecting the optimal values of $i_{\max}$ and $v_{\max}$ is discussed in chapter 4. In this section, without loss of generality, we use v_c for $v_{\max}$, where v_c is the voltage corresponding to SOC of 1; that is

$$v_c = \text{OCV}(1) \tag{2.4.32}$$

Using the above notations, we can write the cost function as follows:

$$J_{\mathrm{tEsT}} = \rho_{\mathrm{t}} k_f \Delta + \sum_{k=0}^{k_f-1} \Big(\Delta R_{0\mathrm{eq}}[k] i^2[k] + \underline{z}^T[k] \tilde{Q}[k] \underline{z}[k] \Big) \tag{2.4.33}$$

where

$$\tilde{Q}[k] = \begin{bmatrix} \rho_{\mathrm{s}} & 0 \\ 0 & \Delta R_{1\mathrm{eq}}[k] \end{bmatrix} \tag{2.4.34}$$

$$\tag{2.4.35}$$

Similarly to section 2.2, we divide the charging process into two stages: in the first stage that lasts for k_1 samples, the battery terminal voltage is less than v_c. That is

$$v[k] < v_c \qquad k = 0, 1, ..., k_1 - 1 \tag{2.4.36}$$

and in the second stage which starts at time k_1 onwards, the battery terminal voltage is equal to v_c. That is

$$v[k] = v_c \qquad k = k_1, k_1 + 1, ..., k_f \tag{2.4.37}$$

As the voltage hits the boundary value of v_c at time k_1, and remains constant from then on, the current in stage 2 is already determined by the constrained dynamics

of the system, as follows:

$$i[k] = \frac{v_c - \text{OCV} - R_1 i_1[k]}{R_0} \qquad k = k_1, k_1 + 1, ..., k_f \tag{2.4.38}$$

$$x[k] = \alpha i_1[k-1] + (1-\alpha) i[k-1] \qquad k = k_1, k_1 + 1, ..., k_f \tag{2.4.39}$$

with the following initial values

$$i[k_1 - 1] = i_{k_1 - 1} \tag{2.4.40}$$

$$i_1[k_1 - 1] = i_{1_{k_1 - 1}} \tag{2.4.41}$$

where i_{k_1-1} and $i_{1_{k_1-1}}$ are the initial values of the currents for stage 2, which are equal to the final values of currents for stage 1.

The current profile in stage 1 is obtained by solving a linear quadratic (LQ) problem. The following algorithm finds the optimal current profile in stage 1.

Algorithm: For a given k_1 value, the optimal current profile in stage 1 (the LQ stage) is obtained as follows:

$$i[k] = -\frac{\Gamma^T}{2\Delta R_{0\text{eq}}[k]} \left(P[k+1] \left((I_3 + \Psi[k] P[k+1])^{-1} \left(\Phi \underline{z}[k] - \Psi[k] \underline{g}[k+1] \nu \right) \right) + \underline{g}[k+1] \nu \right) \tag{2.4.42}$$

where ν and $\Psi[k]$ are given by:

$$\nu = \frac{s_1 - s_{k_f} - \underline{g}^T[0] \underline{z}[0]}{\omega[0]} \tag{2.4.43}$$

$$\Psi[k] = \frac{\Gamma\Gamma^T}{2\Delta R_{0\mathrm{eq}}[k]} \tag{2.4.44}$$

$\underline{z}[0]$ is the initial state, and $\underline{g}[0]$ and $\omega[0]$ are calculated by solving the following backward set of recursions:

$$\begin{aligned} P[k] &= 2\tilde{Q}[k] + \Phi^T P[k+1]\left(I_3 + \Psi[k]P[k+1]\right)^{-1}\Phi \\ \underline{g}[k] &= \Phi^T\left(I_3 + P[k+1]\Psi[k]\right)^{-1}\underline{g}[k+1] \\ \omega[k] &= \omega[k+1] - \underline{g}^T[k+1]\left(I_3 + \Psi[k]P[k+1]\right)^{-1}\Psi[k]\underline{g}[k+1] \end{aligned} \tag{2.4.45}$$

with the following terminal values:

$$\begin{aligned} P[k_1] &= \begin{bmatrix} 0 & 0 \\ 0 & 0 \end{bmatrix} \\ \underline{g}[k_1] &= \begin{bmatrix} 1 & 0 \end{bmatrix}^T \\ \omega[k_1] &= 0 \end{aligned} \tag{2.4.46}$$

The derivation of this algorithm is presented in the "Appendix C".

Based on the above, the numerical calculation of the optimal current is computed via the following steps:

❶ Set $J_{\mathrm{tEsT}}^{\mathrm{old}}$ to a big value (for example, in Matlab, set it as "Inf").

❷ Initialize k_1 with 1.

❸ Solve the set of equations (2.4.45) with the terminal values in (2.4.46).

❹ Calculate the current in stage 2 (the CV stage) by assuming the terminal

voltage as v_c until the SOC reaches the desired value of s_{k_f}.

❺ Calculate the cost function based on the current profiles of stage 1 and stage 2 and assign it to $J_{\text{tEsT}}^{\text{new}}$.

❻ If $J_{\text{tEsT}}^{\text{new}} > J_{\text{tEsT}}^{\text{old}}$, the optimal k_1 is the previous value and the optimal current profile was obtained in the previous step; otherwise, go to next step.

❼ Solve the set of recursions (2.4.45) for one step with the terminal values obtained in the previous step.

❽ Go to step "❹".

It is important to note that although the optimal current profile is derived for model III (see Fig. 2.4.1), the method is generic and it is applicable to any equivalent electrical circuit model, with an enlarged state vector $z[k]$.

It should be noted that the practical meaning of the parameters of optimization problem (e.g., ρ_{t}, ρ_{s}, and ρ_{T} in (2.4.6)) is to use them in an iterative design procedure to reach the desired performance. For example, if the maximum allowed energy loss is $E_{\max}$ and the maximum acceptable time-to-charge is $TTC_{\max}$, then in the design procedure, ρ_{t} should be selected proportional to $\frac{E_{\max}}{TTC_{\max}}$; that is $\rho_{\text{t}} \propto \frac{E_{\max}}{TTC_{\max}}$ and then iterate on the proportionality factor.

2.5 Simulations

In this section, we present simulations based on the theoretical foundations of the previous sections.

2.5.1 Model I

Verification of the Optimal Solution

Here, we apply different levels of current and the simulation is run until the terminal voltage reaches v_c and after that a constant voltage of v_c is applied until the battery is charged to s_{k_f}. Five different current profiles are chosen including the optimal current profile (Fig. 2.5.1). The optimal current profile as mentioned before has the value of $\sqrt{\frac{\rho_t}{R_0}}$ in the CC stage. The battery parameters of Nokia BP-4L (Cell#3), given in the "Appendix A", are used. The following simulation parameters are used: $\rho = 1$, $\Delta = 1$(s), $s_0 = 0$, $s_{k_f} = 1$.

The "Appendix A" also shows the parameters of the OCV curve (calculated based on [20]). The OCV is a function of SOC s as in [20].

$$s_{\rm s} \triangleq E + s(1 - 2E) \tag{2.5.1}$$

$$OCV(s_{\rm s}) = K_0 + K_1 s_{\rm s}^{-1} + K_2 s_{\rm s}^{-2} + K_3 s_{\rm s}^{-3} + K_4 s_{\rm s}^{-4} + K_5 s_{\rm s} + K_6 \ln(s_{\rm s}) + K_7 \ln(1 - s_{\rm s}) \tag{2.5.2}$$

and $E = 0.15$. Fig. 2.5.1 shows the current profiles with different levels of current in the CC stage. As seen from Fig. 2.5.1, at lower levels of current, the CC stage will take a longer time and the terminal voltage reaches the threshold voltage of v_c at a later time. At higher levels of current, however, the OCV grows more rapidly. As the terminal voltage is $v[k] = \text{OCV}\,(s[k]) + R_0 i[k]$, at higher levels of current the threshold voltage of v_c is reached in a shorter time.

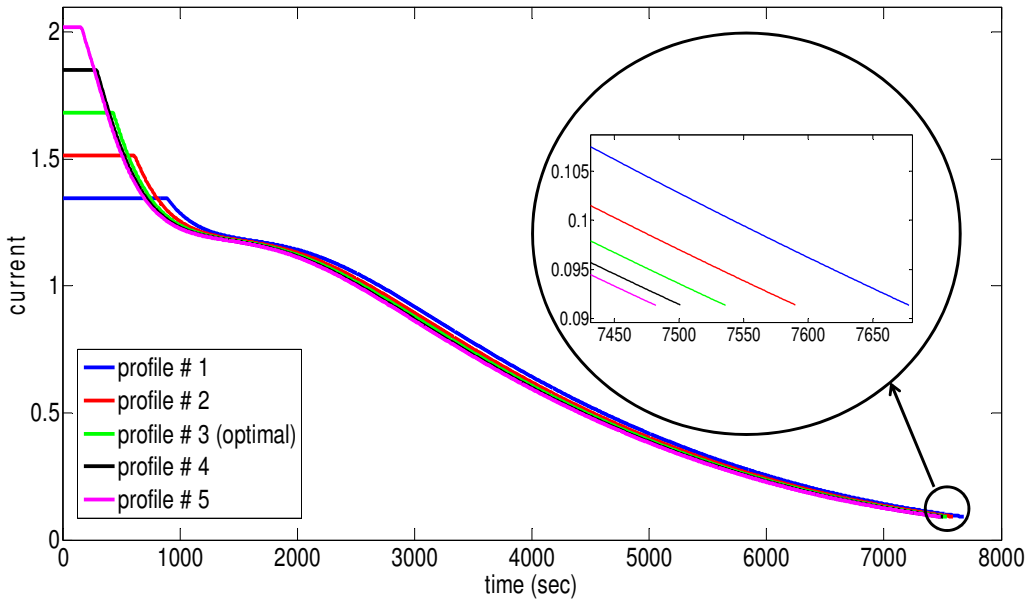

FIGURE 2.5.1: Five different current profiles (including the optimal profile)

Fig. 2.5.2(a) shows the cost function J_{tE} for the five current profiles of Fig. 2.5.1 and Fig. 2.5.2(b) shows the corresponding current levels in the CC stage. It is seen that the optimal current profile (i.e., profile 3) has the lowest cost function. Deviating from this profile, either by increasing or decreasing the current in the CC stage, results in an increase in the cost function. For the lower current levels (profiles 1-2), the rise in the cost function is due to a rise in TTC and for higher current levels (profiles 4-5) the rise in cost function is due to rise in EL.

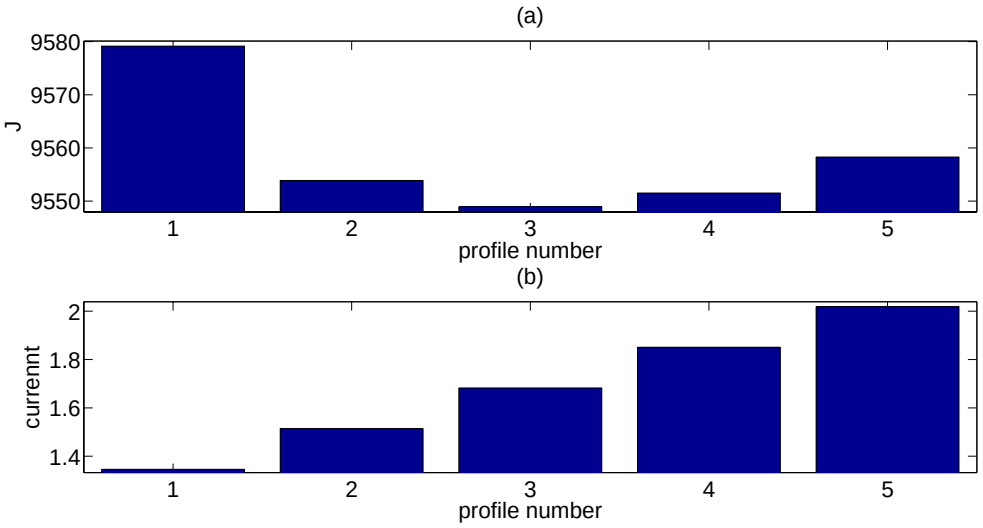

FIGURE 2.5.2: Five different current profiles: a) cost functions b) current levels in CC stage

Effect of Weights

In this subsection, we use different cost functions and find the corresponding optimal profiles. Different values of ρ_t from 0.1 to 0.5 are chosen. Figures 2.5.3, 2.5.4, and 2.5.5, respectively, show the profiles of current, state of charge and terminal voltage. Fig. 2.5.3 shows that low values of ρ_t result in low values of current in the CC stage. In other words, a low ρ_t puts less emphasis on charging time and more emphasis on the energy losses; hence, it results in low level of current which provides low energy losses. On the other hand, by increasing ρ_t, more emphasis is placed on the charging time. Consequently, the level of current is increased proportionally to $\sqrt{\rho_t}$ to reduce the TTC.

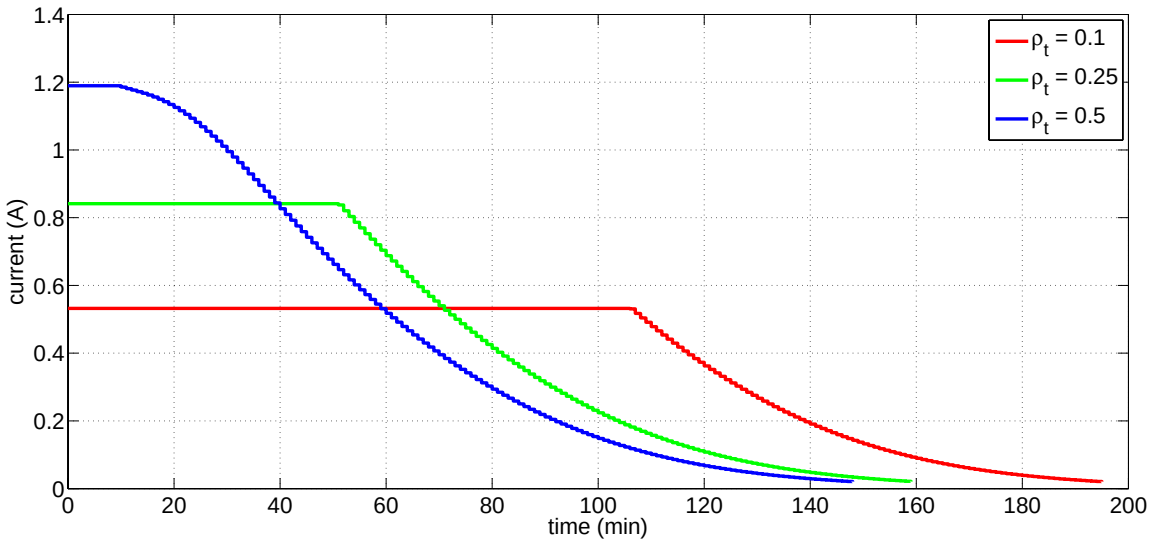

FIGURE 2.5.3: Current profiles for different values of ρ_t

Fig. 2.5.4 shows the state-of-charge profiles for different values of ρ_t. It is seen that by increasing ρ_t, more emphasis is placed on charging time and the SOC reaches the final value in a shorter time. Fig. 2.5.5 shows the terminal voltage profiles for different values of ρ_t. Note that for low values of ρ_t, as the emphasis on energy loss is high, the corresponding current level in CC is low, and consequently, the terminal voltage reaches the threshold value of v_c at a later time. Hence, the duration of CC stage is high and the charging time is high as well.

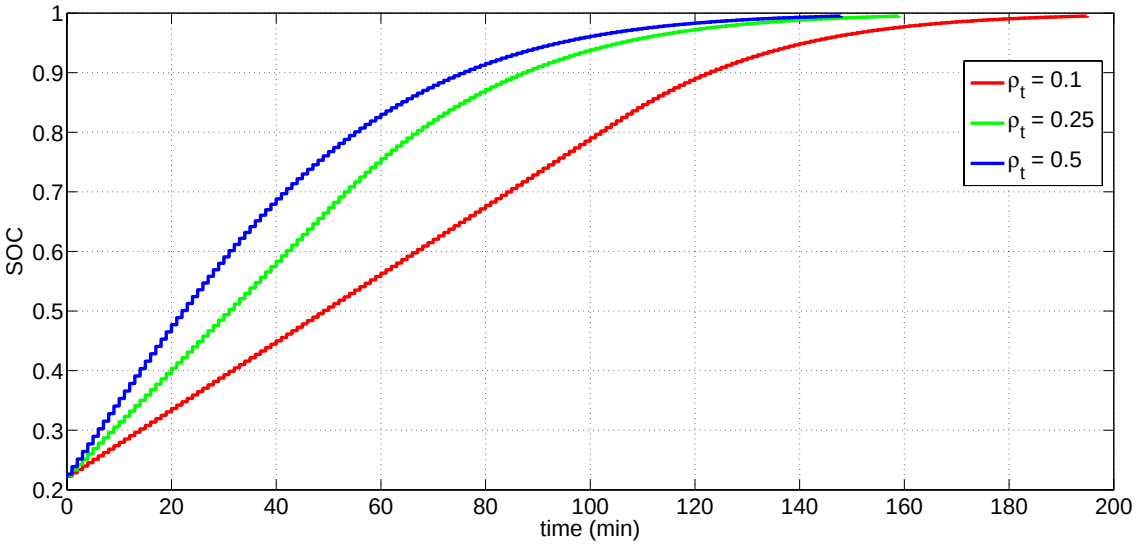

FIGURE 2.5.4: SOC profiles for different values of ρ_t

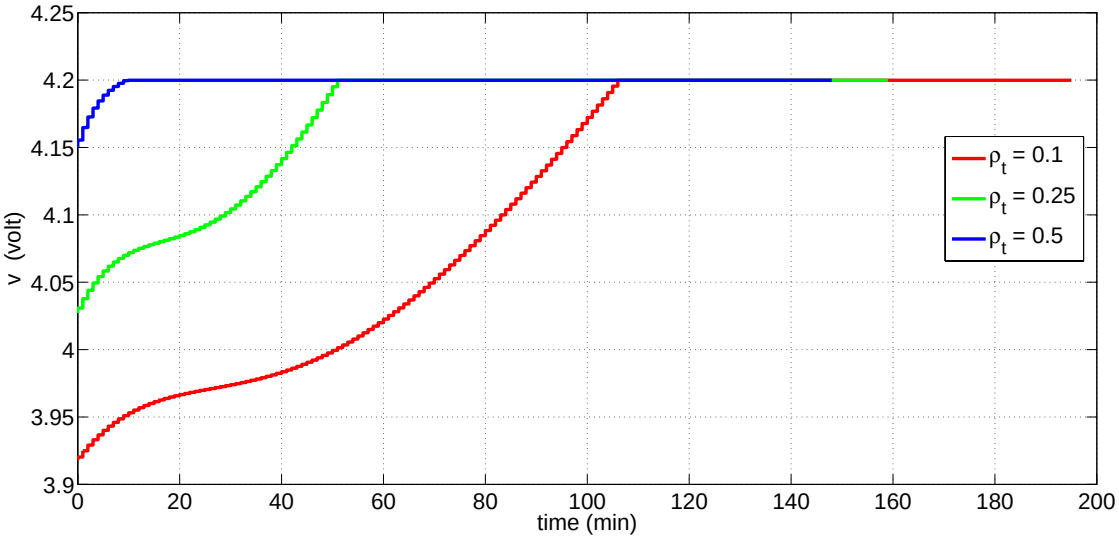

FIGURE 2.5.5: Voltage profiles for different values of ρ_t

Fig. 2.5.6 shows the time-to-charge, energy losses and efficiency as functions of ρ_t. As expected, high values of ρ_t result in lower TTC. The low TTC, however, is

obtained by increasing the current level; as EL is proportional to the square of current, thus the high values of ρ_t result in high values of EL. The high values of EL mean that a higher fraction of input power is wasted; hence it is equivalent to a decline in efficiency.

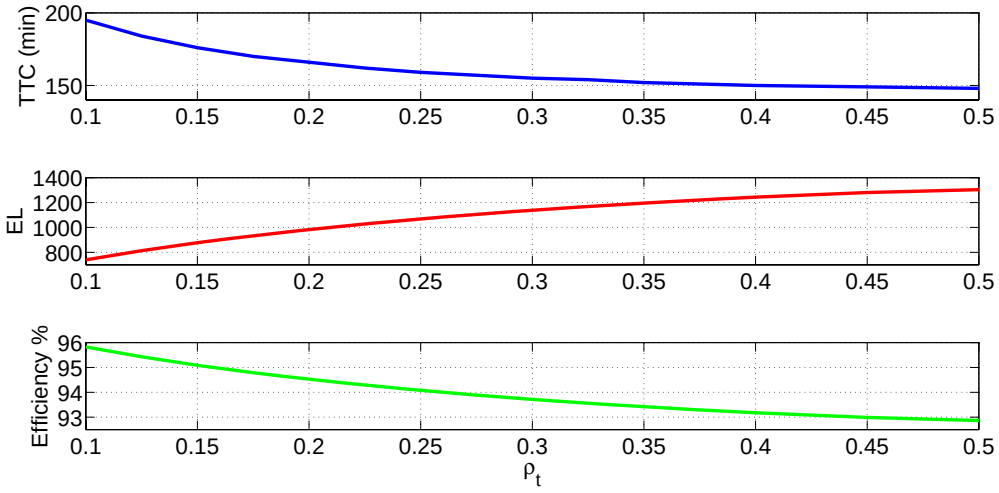

FIGURE 2.5.6: TTC, El and efficiency curves for different values of ρ_t

Fig. 2.5.7 shows the time-to-charge versus efficiency (ratio of effective to total energy) curve. TTC and efficiency are two counteracting objectives. For low values of ρ_t, as less emphasis is put on TTC, the TTC is high; however, high TTC is the result of low current values, which incur low energy losses and hence higher efficiency. For example at $\rho_t = 0.1$, the TTC is 195 minutes, but the efficiency is as high as 95.82%. On the other hand, for high values of ρ_t which place more emphasis on TTC, the TTC is reduced dramatically; however, low TTC is achieved by increasing the current values, which results in high energy losses and hence lower efficiency. For example, at $\rho_t = 0.5$, the TTC is as low as 148 minutes, but the efficiency decreases to 92.87%.

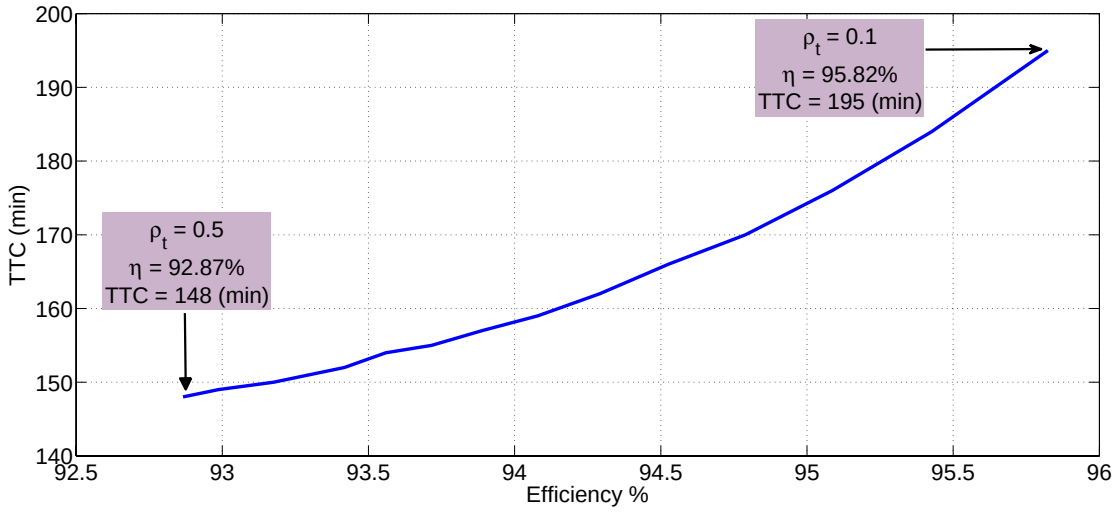

FIGURE 2.5.7: TTC versus efficiency

Temperature Effect

In this section, we consider the effect of temperature rise index (TRI) on optimal charging. The cost function is a weighted sum of TTC (seconds), EL (Joules) and TRI (Kelvin seconds), given by

$$J_{\mathrm{tET}} = \rho_{\mathrm{t}} \times TTC + EL + \rho_{\mathrm{T}} \times TRI \tag{2.5.3}$$

We used two sets of thermal parameters, shown in Table 2.5.1. Parameter set "A" is adopted from [198]. Parameter set "B" is a scaled version of parameter set "A" with m_{batt} set as the weight of Nokia BP-4L. For each set of thermal parameters ("A" or "B"), the weights of the cost function are chosen as $\rho_{\mathrm{t}} = 1$, $\rho_{\mathrm{T}} = 1$ and $\rho_{\mathrm{t}} = 1$, $\rho_{\mathrm{T}} = 4$. Three schemes are used: OtE (equations (2.2.39) and (2.2.40)), OtET (equations (2.3.17) and (2.2.40)), and NOtET (equations (2.3.18) and (2.2.40)). The

cost function in (2.5.3) or (2.3.6) is calculated for the three schemes. Table 2.5.2 shows the cost functions of the three schemes for different weightings. As seen from this table, the cost function for the OtE has the highest value. Also the difference between the cost function of OtET and NOtET is negligible with the OtET being slightly smaller when thermal parameter set "A" is used. For thermal parameter set of "B", there is visually no difference between NOtET and OtET. Due to this negligible difference in the cost function and also since the calculation of NOtET profile is much easier than that of the OtET, it is reasonable to use NOtET rather than the OtET scheme. Also note that the weight on TRI results in a reduction of current, as can be seen from Figure 2.5.8. This reduction in current level results in a lower temperature rise (see Figure 2.5.9). In other words, energy losses with R_{eq} instead of R_0 can be used as a surrogate cost function for the TRI.

TABLE 2.5.1: Battery thermal paramters

Paramter Set	m_{batt} (kg)	R_{Eff} (K/W)	$C_{h,\text{batt}}$ (J/(kg.K))
A	0.37824	7.8146	795
B	0.080	1.6528	168.15

TABLE 2.5.2: Cost function for different schemes

ρ_{t}	ρ_{T}	Thermal Parameters	J_{tET}		
			OtE	NOtET	OtET
1	1	A	26734	22206	22198
1	4	A	72023	38996	38960
1	1	B	14970	14696	14696
1	4	B	24966	21272	21271

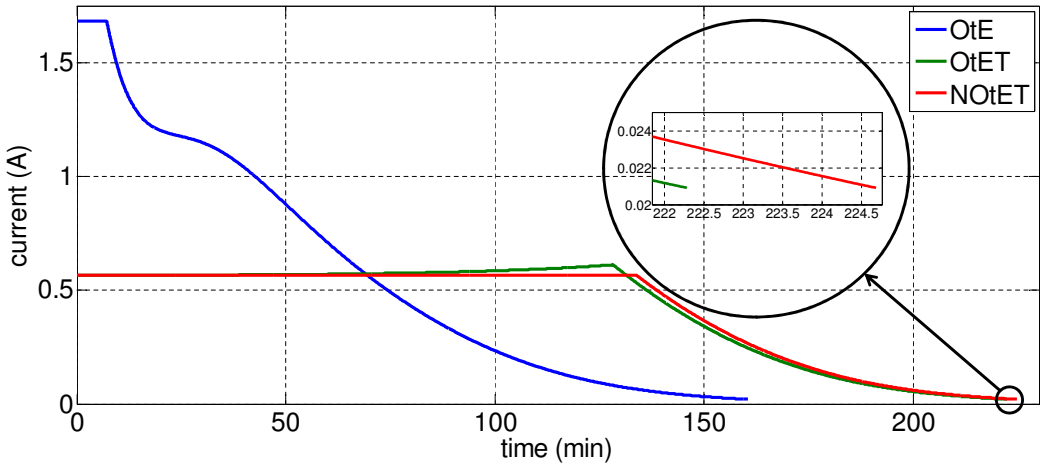

FIGURE 2.5.8: Current profiles for $\rho_{\mathrm{t}} = 1, \rho_{\mathrm{T}} = 1$ and temperature parameter set "A"

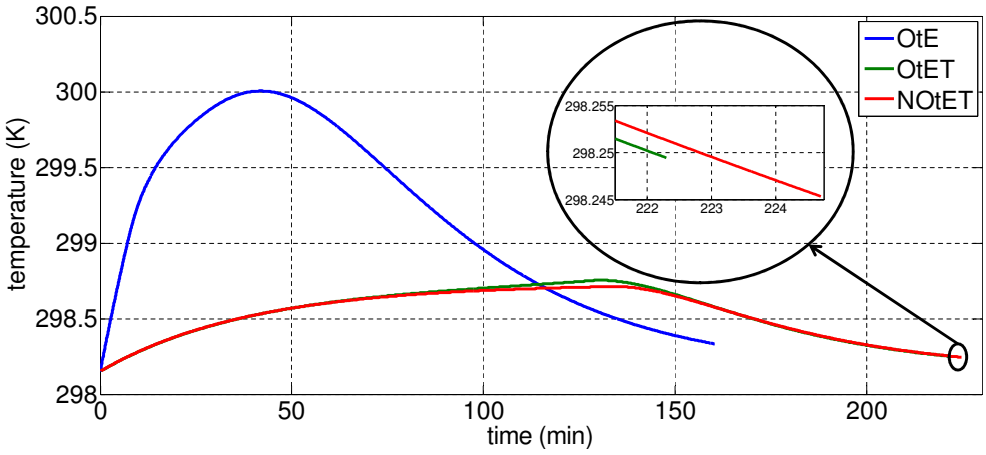

FIGURE 2.5.9: Temperature profiles for $\rho_{\mathrm{t}} = 1, \rho_{\mathrm{T}} = 1$ and temperature parameter set "A"

Analysis of Different Commercial Batteries

In this subsection, we discuss the behavior of different commercial batteries. The parameters of the investigated batteries are given in the "Appendix A". Note that the equivalent electrical circuit parameters given in Table A.0.1 are for model III (see Figure 2.2.3). In simulations, we use the summation of "$R_0 + R_1$" of model III as an estimate of resistance R_0 in model I. The batteries are Samsung EB575152 (four cells), Samsung EB504465 (four cells), Samsung AB463651 (two cells), Nokia BP-4L (four cells), LG LGIP (two cells).

Next, we apply the OtE algorithm with $\rho_{\mathrm{t}} = 0.5$ to 16 commercial batteries to investigate the times-to-charge and efficiencies of the batteries. The parameters of the batteries, i.e., the electrical parameters of the models in Fig. 2.2.2 and 2.2.3, and the parameters of OCV function in (2.5.2), were calculated using experimental data and by applying the BFG algorithms in [20]. These parameters are listed in Tables A.0.1 and A.0.2 in the Appendix. Fig. 2.5.10 shows the TTC versus efficiency for different types of batteries. Among all batteries, Sam-EB575152 (Cell 3) has the lowest efficiency (90.73%). This can be attributed to the high resistance of this battery, which might be due to aging. Sam-EB504465 (Cell 4) has the highest TTC (102 minutes) and Nokia BP-4L (Cell 4) has the highest efficiency. Note that the cells of the same battery are close to each other in terms of efficiency and TTC. Considering all the cells of a battery, we can say that LG-LGIP cells (circle markers) have the highest efficiency (91.4%) . Fig. 2.5.11 shows the cost function values of $J_{\mathrm{tE}} = \rho_{\mathrm{t}} J_{\mathrm{t}} + J_{\mathrm{E}}$. When TTC is weighted with weight value of $\rho_{\mathrm{t}} = 0.5$, Sam-EB575152 (Cell 2) has the best performance.

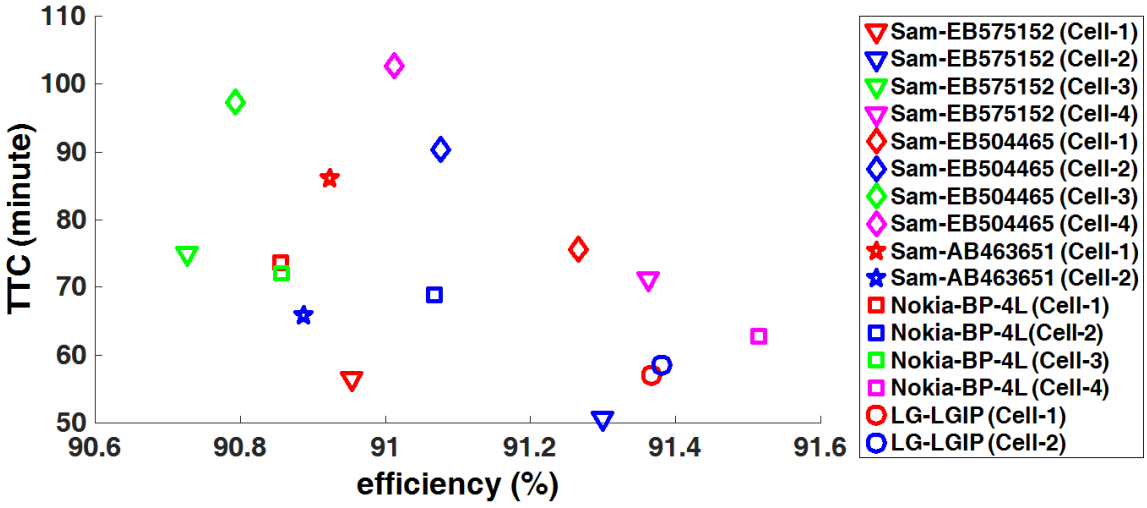

FIGURE 2.5.10: Time-to-charge versus efficiency of different battery types at 25°C

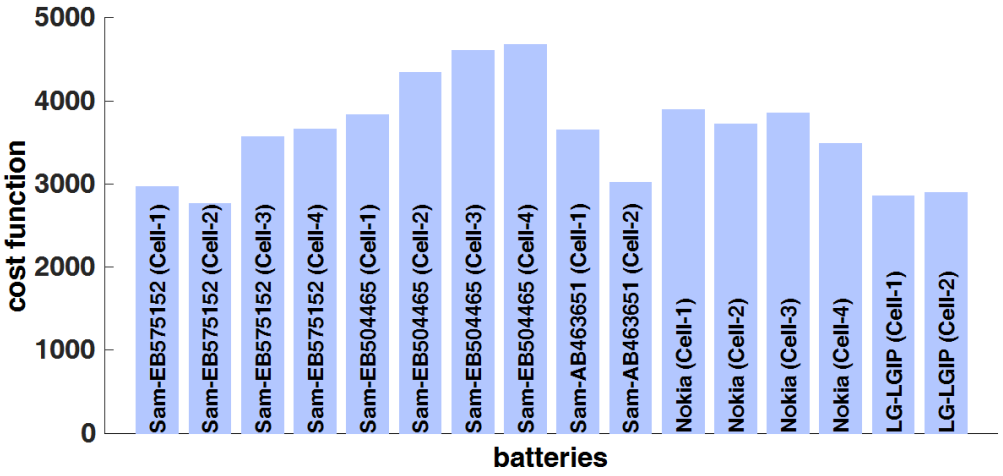

FIGURE 2.5.11: Cost function for different battery types at 25°C, $\rho_t = 0.5$

2.5.2 Model III

Effect of Weights

In this subsection, we use different cost functions and find the corresponding optimal profiles for Model III. First, we set $\rho_s = \rho_T = 0$, and we change the values of ρ_t from 0.1 to 0.5. Figures 2.5.12, 2.5.13, and 2.5.14, respectively, show the profiles of current, state of charge and terminal voltage. Fig. 2.5.12 shows that low values of ρ_t result in low values of current in stage 1 (LQ stage). In other words, a low ρ_t puts less emphasis on charging time and more emphasis on the energy losses; hence, it results in low level of current which provides low energy loss and higher charging efficiency. On the other hand, by increasing ρ_t, more emphasis is placed on the charging time.

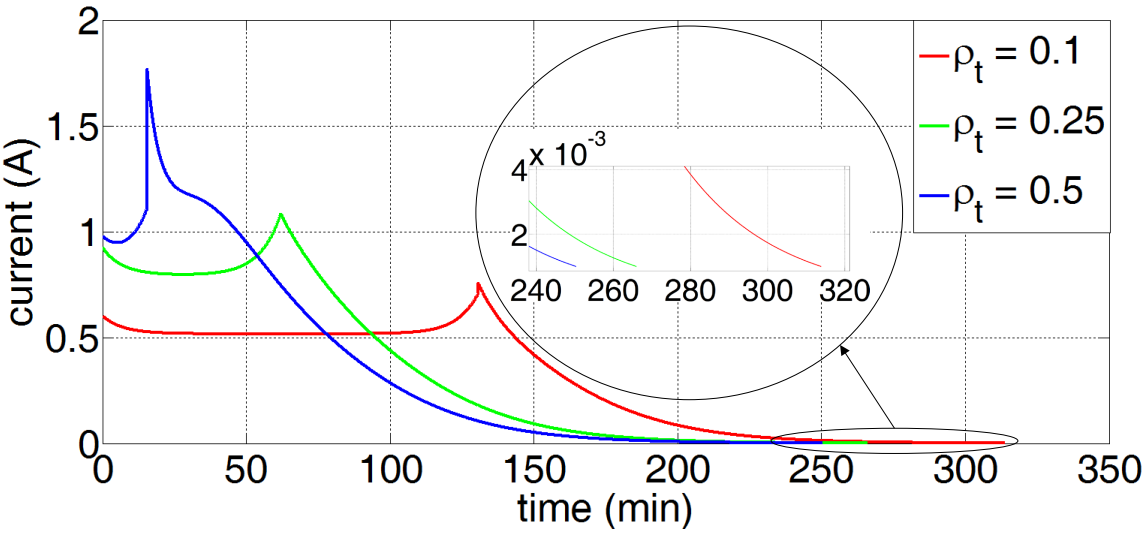

FIGURE 2.5.12: Current profiles for different values of ρ_t

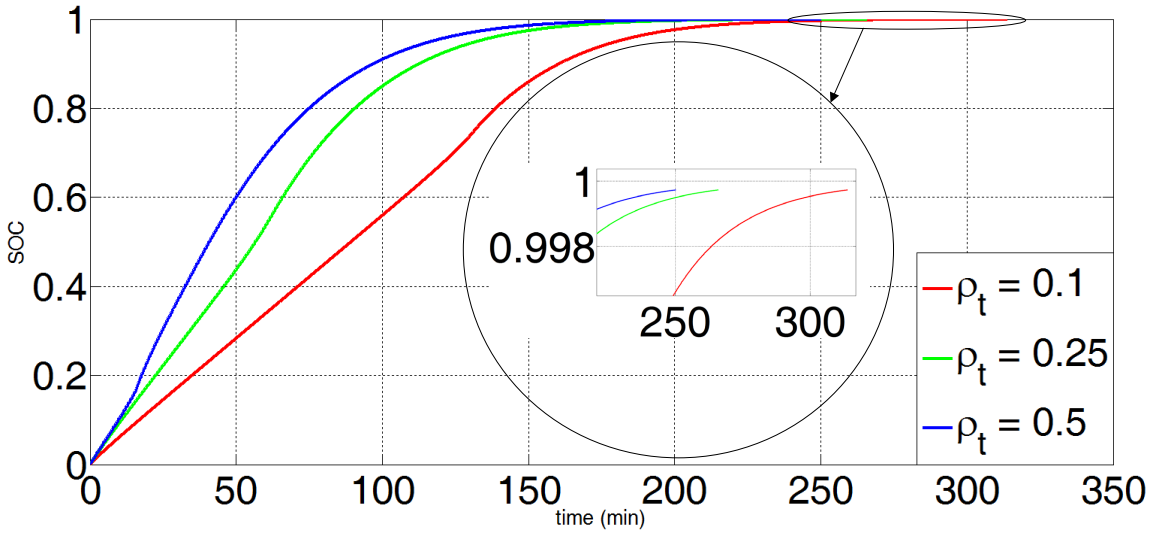

FIGURE 2.5.13: SOC profiles for different values of ρ_t

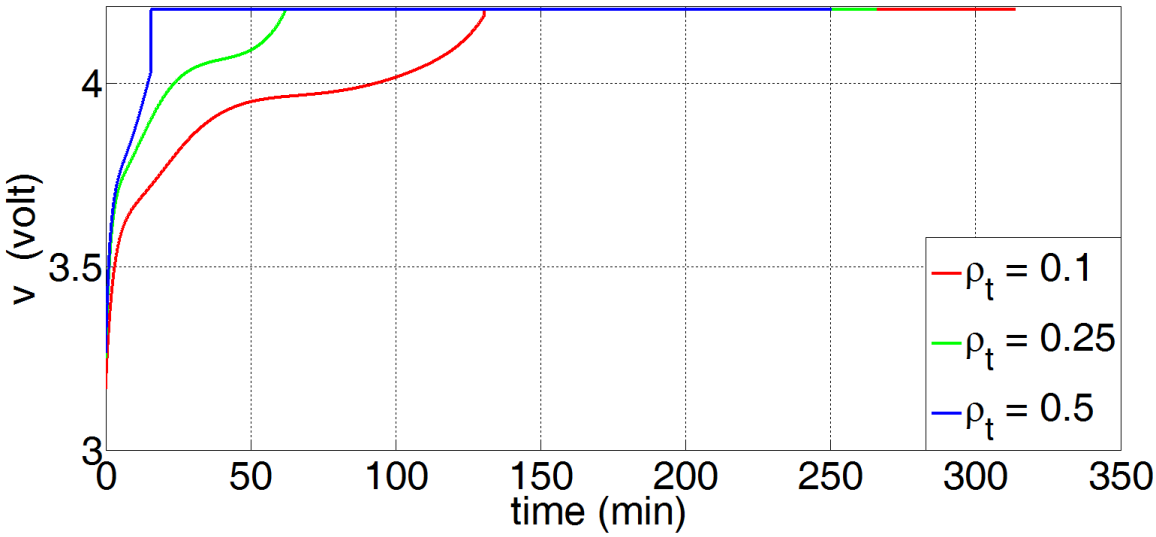

FIGURE 2.5.14: Terminal voltage profiles for different values of ρ_t

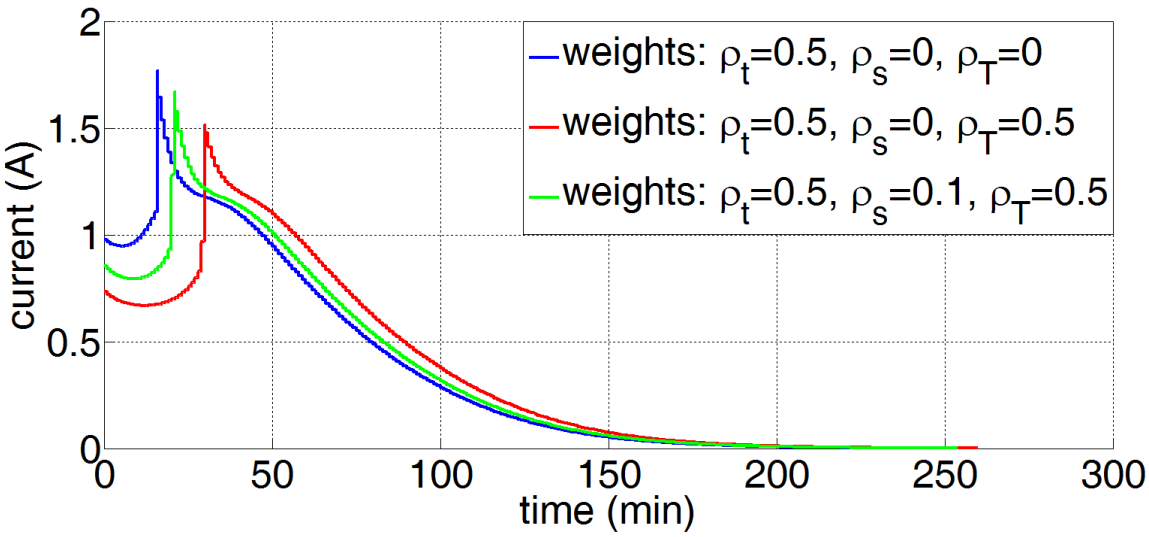

FIGURE 2.5.15: Current profiles for different values of ρ_{T}

Next, we consider the effects of ρ_{T} and ρ_{s}, and we compare the results to the case when these weights are zero. Figure 2.5.15 shows the optimal current profile for three different weight sets. The blue curve represents the optimal profile when $\rho_{\mathrm{t}} = 0.5, \rho_{\mathrm{s}} = 0, , \rho_{\mathrm{T}} = 0$. Here there is no penalty on the temperature rise and the squared difference of the SOC and the final desired SOC (s_{k_f}). When we change ρ_{T} from zero to 0.5, the emphasis on the temperature rise results in a decrease in the magnitude of current, as depicted by the blue and red curves in Fig. 2.5.15. The green curve shows the optimal current profile when we set ρ_{s} to 0.1 as well. Here, the penalty on the squares difference of the SOC and the final desired SOC (s_{k_f}) results in an increase in the current level.

2.6 Summary

The optimal charging problem involving a weighted combination of time-to-charge (TTC), energy loss (EL) and temperature rise index (TRI) was considered. The optimal TTC and EL solution (OtE) is found to be the well-known CC-CV strategy with the value of current in the CC stage being a function of the ratio of weighting on TTC and EL and also the resistance of battery. To the best of our knowledge, this is the first time that it is proved that the well-known CC-CV charging profile is the optimal solution of a particular optimization problem, namely, the problem of minimizing the weighted sum of time-to-charge and energy loss. In addition, an analytical solution for the optimal TTC, EL and TRI, referred to as OtET, was developed. Due to similarity of the structure of the OtE and OtET solutions, a near-optimal version of OtET was developed (referred to as NOtET). The NOtET is a CC-CV strategy with the value of current in the CC stage being a function of the ratio of weighting on TTC and EL, the resistance of the battery and the effective thermal resistance. Then, we presented a linear quadratic optimization approach and its solution to optimally charging a Li-ion battery in a general form. The optimal profile was derived based on a cost function, which is a weighted sum of time-to-charge (TTC), energy loss (EL), sum of the squares of the differences of the state-of-charge (SOC) from the final desired SOC, and temperature rise index (TRI). The presented solution strategy is generic and it is applicable to any equivalent electrical circuit model of a battery. A number of simulations were conducted to evaluate the effect of weighting parameters. Finally, extensive results on industrial batteries from LG, Nokia and Samsung were presented.

Chapter 3

Capacity Fade Modeling

3.1 Introduction

In this chapter, we propose two models, namely LAR-$\alpha\beta\gamma$ and CVD, to estimate the normalized capacity (and, equivalently, the capacity fade) as a function of the cycle number. The motivation for developing a capacity fade model is that, for the level-I control policy (to be presented in the next chapter), we need a capacity model that considers both the current and the terminal voltage as control parameters of the model. In other words, this chapter is a precursor to the next chapter. These models are developed by exploring a number of models with different fitting methods. The development of the models is based on the data obtained from the aging experiments, which are detailed in section 3.2. Let n denote the cycle number. The capacity at cycle n, denoted by $Q[n]$, is calculated by trapezoidal integration of the injected current during the charging process, which is also referred to as the Coulomb counting. In each experiment, the calculated capacities $Q[n]$ are normalized by dividing them by

the capacity of the battery at the first cycle, i.e., $Q[1]$, and the resulting normalized capacities are denoted by $Q_{\text{norm}}[n]$; that is

$$Q_{\text{norm}}[n] = \frac{Q[n]}{Q[1]} \qquad n = 1, 2, \ldots \tag{3.1.1}$$

These normalized capacities are used for fitting the capacity models.

This chapter is organized as follows. In section 3.2, we explain how the aging experiments have been conducted. In section 3.3, we propose LAR-$\alpha\beta\gamma$ model. Then, in section 3.4, we study the LS-BE model. The comparison of the LAR-$\alpha\beta\gamma$ and the LS-BE models is presented in section 3.5. In section 3.6, we present the CVD model, which is a function of control variables $v_{\max}$ and $i_{\max}$. The comparison of the CVD and the LS-BE models is presented in section 3.7. In section 3.8, using the CVD model, we analyze the effect of current and terminal voltage on capacity fade. Finally, in section 3.9, we summarize the chapter.

3.2 Aging Experiments

In order to study the effects of aging on capacity, ten different experiments were performed. The batteries used in these experiments were Samsung GS4 with a capacity of 2600 mAh and a nominal terminal voltage of 4.35 volts. The batteries were exposed to several (from 25 to 200) cycles of charging and discharging with a 10 minute rest after any charge or discharge process. The experiments were performed at room temperature (25 °C) using Keithley 2651A [2]; descriptions of the experiments are provided in Table 3.2.1. Seven different charge profiles (Ch1-Ch7) were used and are described in Table 3.2.2. Note that 1.0C for GS4 battery corresponds to 2.6

amperes. All the charge profiles are terminated once the charge current falls below $\frac{1}{20}$C or, equivalently, 130 mA. Three different discharge profiles, namely Disch1-Disch3, were used. Table 3.2.3 describes the discharge profile Disch1, which has been used in all experiments except 2 and 10. The profile Disch2 is similar to Disch1, except that 0.25C is used for stage 1, 0.5C for stage 2, and 0.2C for stage 3. The profile Disch3 consists of only one stage: discharge at 0.2C until the terminal voltage reaches 2.8V.

TABLE 3.2.1: List of aging experiments

Experiment ID	Charge Profile	Discharge Profile	Number of Cycles
1	Ch1	Disch1	200
2	Ch2	Disch1	125
3	Ch3	Disch1	75
4	Ch3	Disch3	75
5	Ch4	Disch1	50
6	Ch4	Disch2	50
7	Ch5	Disch1	50
8	Ch2	Disch1	50
9	Ch6	Disch1	25
10	Ch7	Disch1	25

TABLE 3.2.2: Description of charging profiles

Charge Profile	Description
Ch1	Multi-level current at 1.25C for 1200 seconds, 0.833C for 1100 seconds then 0.5C until the battery terminal voltage hits 4.35, afterwards the CV stage is activated with 4.35 volts
Ch2	CC-CV with current at CC stage equal to 1.0C and voltage at CV stage equal to 4.35 volts
Ch3	CC-CV with current at CC stage equal to 0.7C and voltage at CV stage equal to 4.35 volts
Ch4	Multi-level CV at 4.45, 4.40, 4.35, 4.30, 4.25 volts each for 0.5 seconds with tapering down the voltage to 4.35 volts after SOC of 70%
Ch5	CC-CV with current at CC stage equal to 1.3C and voltage at CV stage equal to 4.35 volts
Ch6	CC-CV with current at CC stage equal to 1.3C and voltage at CV stage equal to 4.25 volts
Ch7	CC-CV with current at CC stage equal to 1.0C and voltage at CV stage equal to 4.25 volts

TABLE 3.2.3: Description of discharge profile of Disch1

Stage	Description
1	discharge at 0.5C for 1 hour
2	discharge at 1C for 15 minutes
3	discharge at 0.5C for few seconds (6 seconds)
4	discharge at 0.2C until battery terminal voltage hits 2.8 volts

Figure 3.2.1 shows a sample charge-discharge profile for one of the experiments and Figure 3.2.2 shows all of its 125 voltage profiles. It can be seen that, as the battery ages, the time-to-charge and time-to-discharge decrease and hence the total time of a charge-rest-discharge-rest cycle decreases. This decrease in time-to-charge and time-to-discharge is due to capacity fade. For an animation about illustration of capacity fade (via the decreasing time-to-charge and time-to-discharge as the battery ages), the reader may refer to [1].

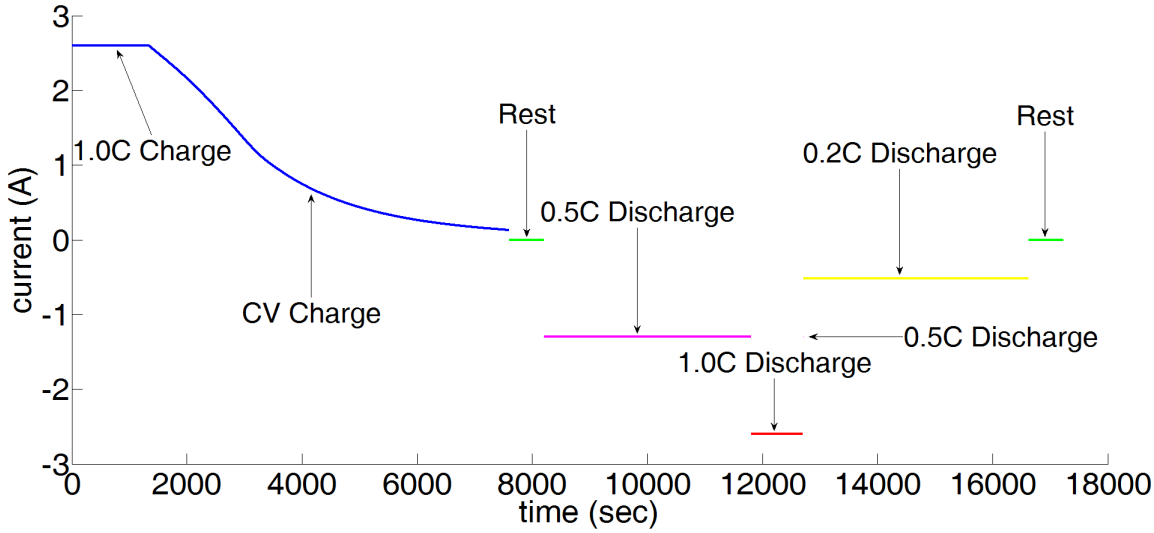

FIGURE 3.2.1: A sample current profile (charge-rest-discharge-rest)

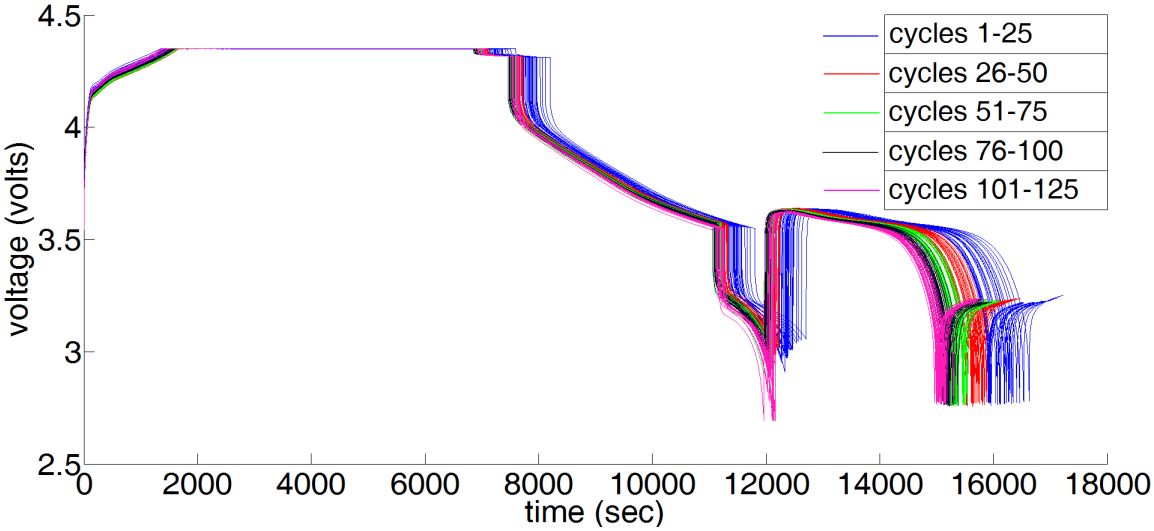

FIGURE 3.2.2: Voltage profiles of 125 cycles (data set 2)

Remark 3.2.1. Note that Fig. 3.2.2 also illustrates power fade in a battery as it ages. A jump in the current results in a jump in the terminal voltage. The series resistance of a battery (R_0) equals to the ratio of the jump in the terminal voltage to the jump in the current. If the jump in the current remains fixed, as the number of

cycles increases, the change in the jump in the terminal voltage is proportional to the change in the series resistance in the battery as it ages. One can see as the current jumps from $-2.6\,A(-1\,\text{Crate})$ to $-130\,mA(-\frac{1}{20}\,\text{Crate})$, the magnitude of the jump in terminal voltage increases as the number of cycles goes up. This demonstrates that the series resistance in the battery increases as the battery ages, which demonstrates power fade in the battery due to aging.

3.3 LAR-$\alpha\beta\gamma$ Model

Among the explored models, the following model with the least absolute residuals (LAR) as its fitting criterion was found to better capture the trend in the normalized capacity. We refer to this model as "LAR-$\alpha\beta\gamma$".

$$Q_{\text{norm}}[n] = \alpha\beta^n n^\gamma \qquad n = 1, 2, \ldots \tag{3.3.1}$$

The LAR method is robust in that it minimizes the sum of the absolute values of the residuals, rather than the squared differences as in ordinary least squares. Therefore, extreme values have substantially smaller influence on the fit, thereby achieving the desired robustness of the fit. The Matlab function of "fit" with the "StartPoint" of [1 1 1] was used for training the model.

3.4 LS-BE Model

For performance comparison with the LAR-$\alpha\beta\gamma$ model, the following bi-exponential model, which is frequently used in the literature [75], [196], [82], was chosen. We used

the least squares approach as the fitting method; hence we refer to it as "LS-BE".

$$Q_{\text{norm}}[n] = \alpha_1\beta_1^n + \alpha_2\beta_2^n \qquad n = 1, 2, \ldots \tag{3.4.1}$$

The estimation of the parameters is performed as follows. First, we can easily verify that the following relation holds.

$$Q_{\text{norm}}[n+1] = x_1 Q_{\text{norm}}[n] - x_2 Q_{\text{norm}}[n-1] \tag{3.4.2}$$

where,

$$x_1 = (\beta_1 + \beta_2) \qquad x_2 = \beta_1\beta_2 \tag{3.4.3}$$

Since we have the profile of normalized capacity, the unknown variables of x_1 and x_2 in (3.4.2) can easily be estimated using LS method. Since x_1 and x_2 are, respectively, the sum and the product of β_1 and β_2, we can find the estimates of β_1 and β_2 by solving the following quadratic equation, once we estimate x_1 and x_2.

$$\beta^2 - x_1\beta + x_2 = 0 \tag{3.4.4}$$

Having the estimates of β_1 and β_2, equation (3.4.1) reduces to a linear equation with unknown variables α_1 and α_2. Hence, by applying the LS method, we can estimate both α_1 and α_2.

Note that since the capacity model is in the normalized form, the capacity

fade (CF), which is defined in (3.4.5), can also be written as in (3.4.6).

$$\mathrm{CF}[n] = \frac{Q[1] - Q[n]}{Q[1]} \qquad n = 1, 2, \ldots \tag{3.4.5}$$

$$\mathrm{CF}[n] = 1 - Q_{\mathrm{norm}}[n] \qquad n = 1, 2, \ldots \tag{3.4.6}$$

3.5 Comparison of LAR-$\alpha\beta\gamma$ Model and LS-BE Model

Figures 3.5.1 and 3.5.2 show the data for normalized capacities in one of the experiments, along with the estimates of LAR-$\alpha\beta\gamma$ and LS-BE models, with 40 and 160 training samples, respectively. In this experiment, as Fig. 3.5.1 and Fig. 3.5.2 show, the LAR-$\alpha\beta\gamma$ is better at capturing the trend in the normalized capacities than LS-BE. While the outliers affect the LS-BE model significantly, they have minor effect on the LAR-$\alpha\beta\gamma$ and hence LAR-$\alpha\beta\gamma$ filters out the outliers. It is seen that predictions of LAR-$\alpha\beta\gamma$ are consistent with the experimental data even when just 40 samples are used in the fitting process.

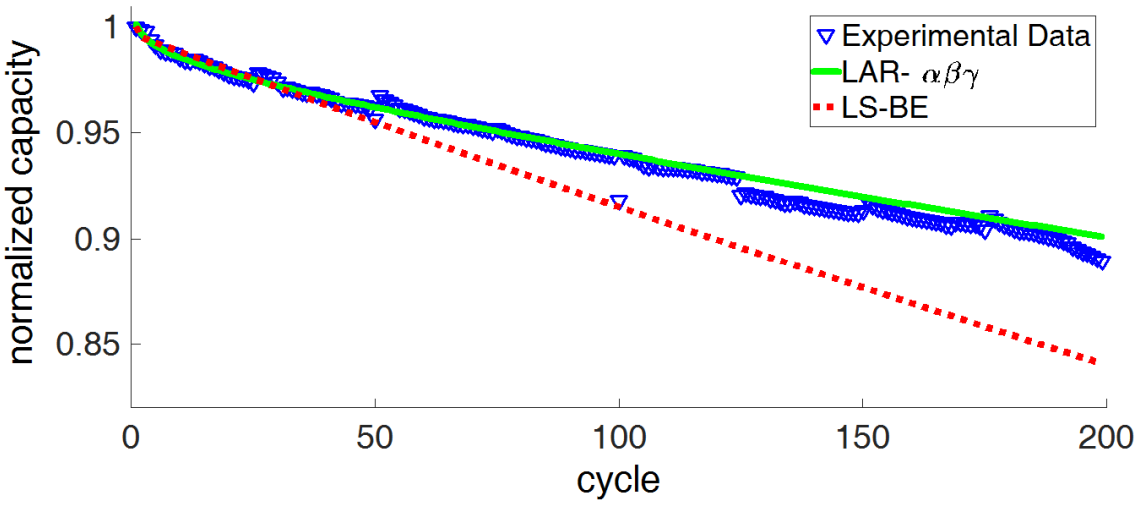

FIGURE 3.5.1: Comparison of LAR-$\alpha\beta\gamma$ model and LS-BE model with 40 training samples

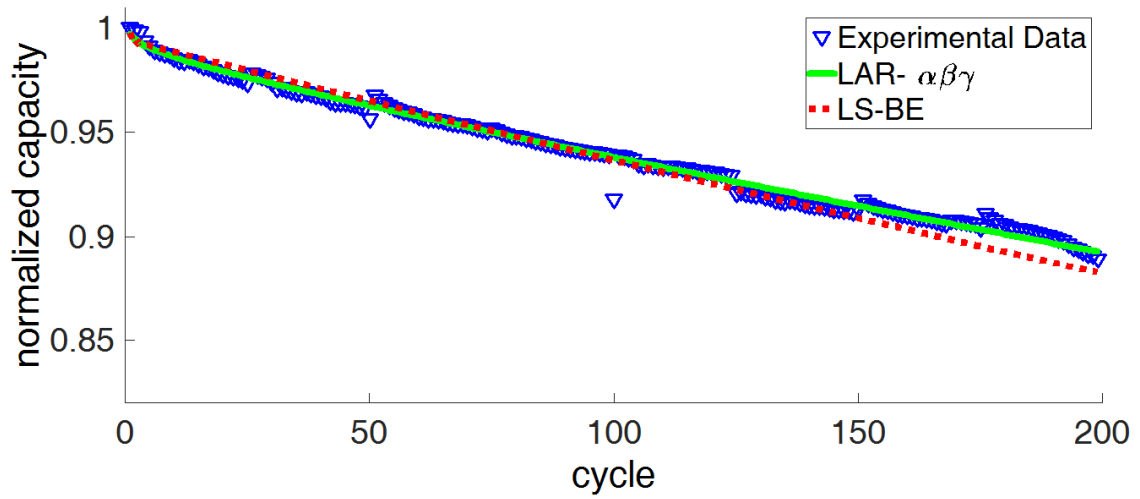

FIGURE 3.5.2: Comparison of LAR-$\alpha\beta\gamma$ model and LS-BE model with 160 training samples

Next, in one of the experiments, we used the data from cycles 1-175 for training the two models, and then we predicted the normalized capacity for cycles

176-200. We found while the average of the relative error of LS-BE prediction is 0.99%, that of LAR-$\alpha\beta\gamma$ is only 0.35%; in addition, the maximum values of relative error for these models are 1.50% and .87%, respectively. This suggests that LAR-$\alpha\beta\gamma$ provides better performance in capturing the trend in capacity fade than LS-BE does. This observation was found to be consistently valid across all the experiments.

Next we compare LAR-$\alpha\beta\gamma$ and the LS-BE models using the Akaike Information Criterion (AIC). The AIC is used to rank multiple models in the Kullback-Leibler information sense [38] and values the goodness-of-fit and parsimony, two often-counteracting factors. However, once a model, with fewer parameters (more parsimonious), provides a better goodness-of-fit than a model with more parameters, the AIC selects the model with less parameters. The number of parameters for the LAR-$\alpha\beta\gamma$ is 3 and for the LS-BE is 4, meaning that the LAR-$\alpha\beta\gamma$ model is more parsimonious than the LS-BE model. As for the goodness-of-fit, Fig. 3.5.3 shows the ratio of MSE (Mean Squared Error) of LAR-$\alpha\beta\gamma$ to that of LS-BE, where in all experiments, this ratio is higher than 1 with it being as high as 3.6 for the first experiment. In ranking models via AIC, what is important is the AIC differences rather than the AIC values themselves [38]. Table 3.5.1 shows the AIC differences ($\Delta\text{AIC} = \text{AIC}_{\text{LS-BE}} - \text{AIC}_{\text{LAR}-\alpha\beta\gamma}$) for the 10 aging experiments. For eight of experiments the AIC difference is greater than 10 and for the remaining two experiments, it is greater than 4. As rule of thumb, the level of empirical support for a model with higher AIC is considerably less when the AIC difference is between 4 and 7 and it is essentially none when the AIC difference is greater than 10 [4]. The relative likelihood of LS-BE model (with respect to LAR-$\alpha\beta\gamma$) can be calculated using the AIC differences as $l_{\text{LS-BE}} = \exp(-\frac{\Delta\text{AIC}}{2})$[38]. These values are shown in Table 3.5.1 and it is seen that the highest value for relative likelihood of LS-BE model is 0.1,

which demonstrates that the LAR-$\alpha\beta\gamma$ model is better than LS-BE model in the Kullback-Leibler information sense.

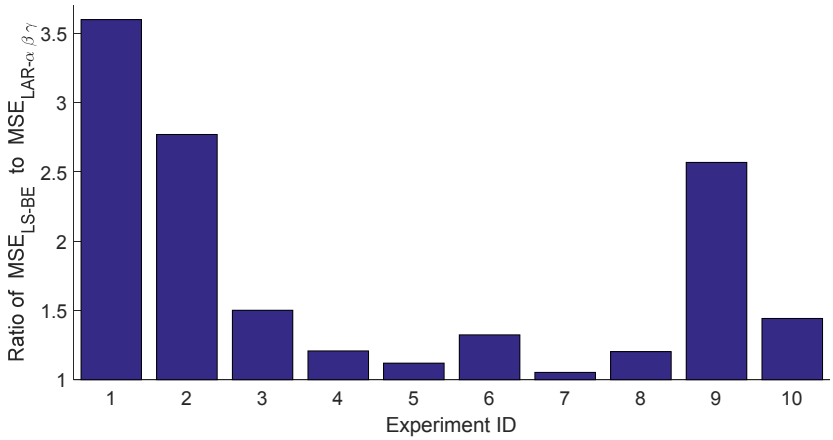

FIGURE 3.5.3: MSE ratio of LS-BE to LAR

TABLE 3.5.1: AIC differences of the LAR-$\alpha\beta\gamma$ and LS-BE models and relative likelihood of LS-BE model for all aging experiments

Experiment ID	1	2	3	4	5	6	7	8	9	10
$\Delta\text{AIC} = \text{AIC}_{\text{LS-BE}} - \text{AIC}_{\text{LAR}-\alpha\beta\gamma}$	257	128	32	16	7.5	16	4.5	11	25	11
$l_{\text{LS-BE}}$ (Relative likelihood)	0.00	0.00	0.00	0.00	0.02	0.00	0.10	0.00	0.00	0.00

Table 3.5.2 shows the parameters of LAR-$\alpha\beta\gamma$ model for the ten experiments.

TABLE 3.5.2: Parameters of LAR-$\alpha\beta\gamma$ model for all experiments

Experiment ID	α	β	γ
1	0.9992	0.9995	-0.0037
2	1.0015	0.9996	-0.0027
3	1.0007	0.9996	-0.0018
4	1.0007	0.9996	-0.0006
5	1.0013	0.9995	-0.0042
6	1.0008	0.9996	-0.0043
7	1.0005	0.9996	-0.0028
8	1.0016	0.9996	-0.0032
9	1.0004	0.9996	-0.0021
10	1.0004	0.9996	-0.0009

3.6 CVD Model

In order to be able to apply the level-I control policy (as described in chapter 4) to select the optimal values for the maximum allowable current and the maximum allowable terminal voltage, we need a capacity fade model that incorporates these two parameters. For this reason, we developed a control variable-dependent model (CVD model), in which the $\alpha\beta\gamma$ parameters are dependent on $v_{\max}$, and $i_{\max}$. The model chosen for this purpose is as follows:

$$Q_{\text{norm},v_{\max},i_{\max}}[n] = (\alpha_1 v_{\max}^{\alpha_2} i_{\max}^{\alpha_3})\,(\beta_1 v_{\max}^{\beta_2} i_{\max}^{\beta_3})^n n^{(\gamma_1+\gamma_2 v_{\max}+\gamma_3 i_{\max})} \qquad n = 1, 2, ... \quad (3.6.1)$$

The fitting of model (3.6.1) is performed in three stages:

❶ The data for each experiment are used to find the corresponding LAR-$\alpha\beta\gamma$ model.

❷ For each experiment, the corresponding LAR-$\alpha\beta\gamma$ is used to generate the normalized capacity data for 500 cycles.

❸ The generated normalized capacity data in stage 2 for all experiments as well as the $v_{\max}$ and $i_{\max}$ of the experiments are used to fit the CVD model using the LS approach.

The CVD model of (3.6.1) can be written as follows:

$$Q_{\text{norm},\underline{u}}[n] = f(\underline{\alpha}, \underline{\beta}, \underline{\gamma}, \underline{u}, n) \tag{3.6.2}$$

$$\underline{\alpha} = \begin{bmatrix} \alpha_1 & \alpha_2 & \alpha_3 \end{bmatrix}^T \tag{3.6.3}$$

$$\underline{\beta} = \begin{bmatrix} \beta_1 & \beta_2 & \beta_3 \end{bmatrix}^T \tag{3.6.4}$$

$$\underline{\gamma} = \begin{bmatrix} \gamma_1 & \gamma_2 & \gamma_3 \end{bmatrix}^T \tag{3.6.5}$$

$$\underline{u} = \begin{bmatrix} v_{\max} & i_{\max} \end{bmatrix}^T \tag{3.6.6}$$

where $\underline{\alpha}$, $\underline{\beta}$, and $\underline{\gamma}$ are fixed parameters, once the model is trained. Therefore, the trend in capacity (and consequently capacity fade) over cycles depends on the values of control variables $\underline{u}$. Note that $v_{\max}$ and $i_{\max}$ are expressed in normalized form with their nominal values being 4.35 V and 2.6 A, respectively.

Table 3.6.1 shows the parameters of the CVD model.

TABLE 3.6.1: Parameters of CVD model

α_1	α_2	α_3
1.0007	0.0539	-0.0051
β_1	β_2	β_3
0.9996	-0.0012	-1.0407×10^{-4}
γ_1	γ_2	γ_3
0.0749	-0.0767	-4.9293×10^{-4}

3.7 Comparison of CVD and LS-BE Models

Figure 3.7.1 shows a comparison of the LAR-$\alpha\beta\gamma$, CVD and LS-BE models in capturing the trend in capacities for two of the experiments. The CVD model and the LAR-$\alpha\beta\gamma$ model are indistinguishable. Figure 3.7.2 shows the relative error of the CVD and the LS-BE models with respect to the LAR-$\alpha\beta\gamma$ model. As is evident from these experiments, compared to LS-BE, the CVD model has a lower relative error.

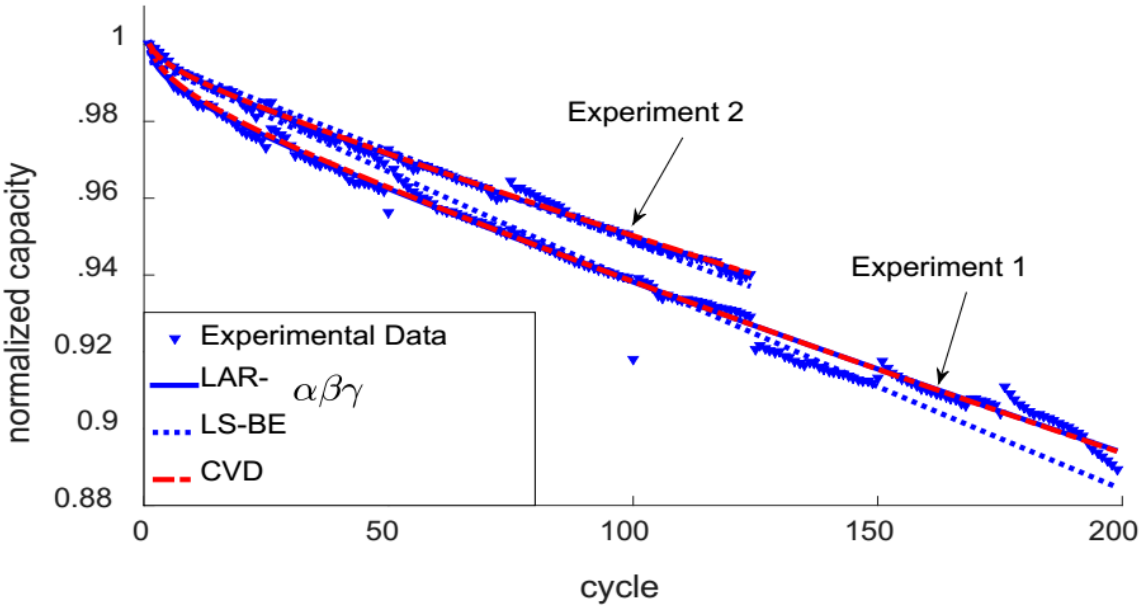

FIGURE 3.7.1: Comparison of LAR-$\alpha\beta\gamma$ model and LS-BE model with different fitting data lengths.

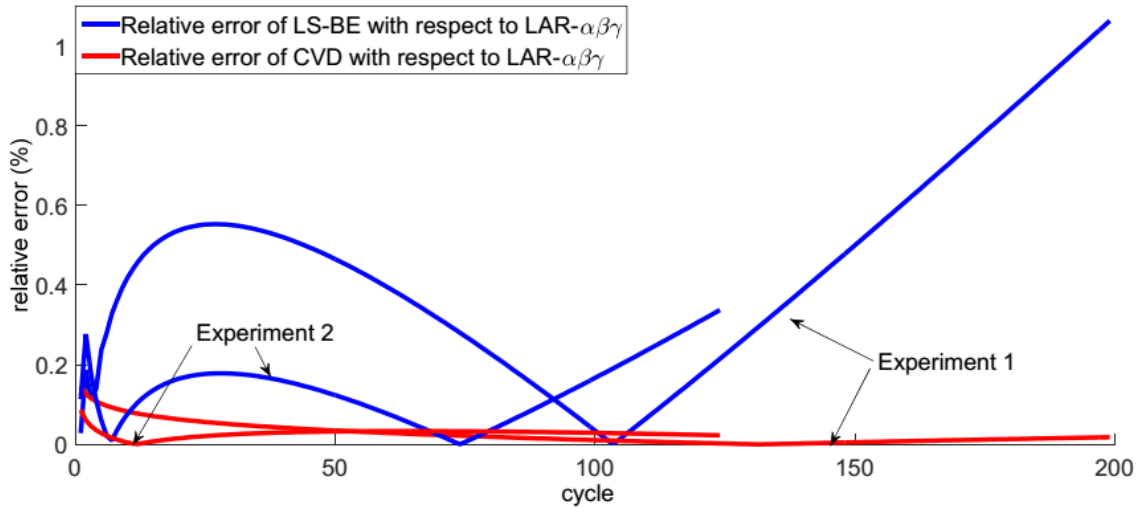

FIGURE 3.7.2: Relative error of LS-BE, and CVD models with respect to LAR-$\alpha\beta\gamma$

3.8 Effect of Terminal Voltage and Current on Battery Capacity

In this section, using the CVD model, we consider the effect of voltage and current on the capacity curves. For this purpose, we use the range $\begin{bmatrix} 0.97 & 1.02 \end{bmatrix}$ for both normalized $v_{\max}$ and normalized $i_{\max}$. Note that these variables are in normalized form with 1 for $v_{\max}$ and $i_{\max}$ representing 4.35 V and 2.6 A, respectively. Figure 3.8.1 shows 80 capacity curves which are obtained by 20 linearly-spaced values in the voltage range and 4 linearly-spaced values in the current range. The red and green curves show the harshest and mildest strategies, respectively, corresponding to $\underline{u} = \begin{bmatrix} 1.02 & 1.02 \end{bmatrix}^T$ and $\underline{u} = \begin{bmatrix} 0.97 & 0.97 \end{bmatrix}^T$. It is seen that these 80 curves span almost all the area between the harshest and mildest strategies. On the other hand, Figure 3.8.2 shows 80 capacity curves which are obtained by 4 linearly-spaced values in the voltage range and 20 linearly-spaced values in the current range. Again, the red and green curves show the harshest and mildest strategies, respectively, corresponding to $\underline{u} = \begin{bmatrix} 1.02 & 1.02 \end{bmatrix}^T$ and $\underline{u} = \begin{bmatrix} 0.97 & 0.97 \end{bmatrix}^T$. It is seen that there is sparsity in the region between the red curves. More specifically, there are four sets (corresponding to the four values of $v_{\max}$) of curves each containing 20 curves (corresponding to the 20 values of $i_{\max}$) and these four sets are separated by empty spaces. In other words, Figures 3.8.1 and 3.8.2 confirm that $v_{\max}$, rather than $i_{\max}$, has a salient effect on capacity fade.

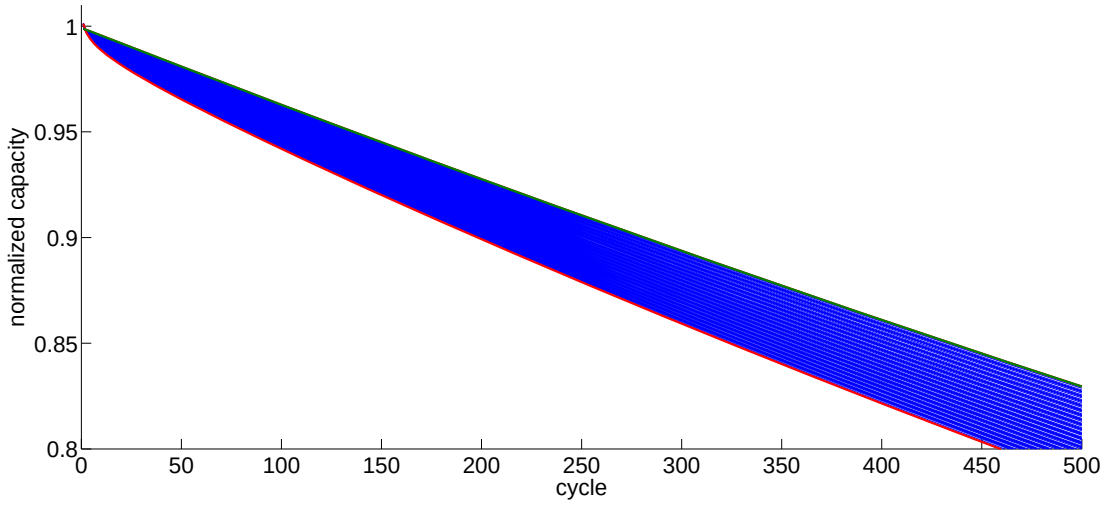

FIGURE 3.8.1: Plot of 80 capacity curves with high resolution in voltage (20 values) and low resolution in current (4 values)

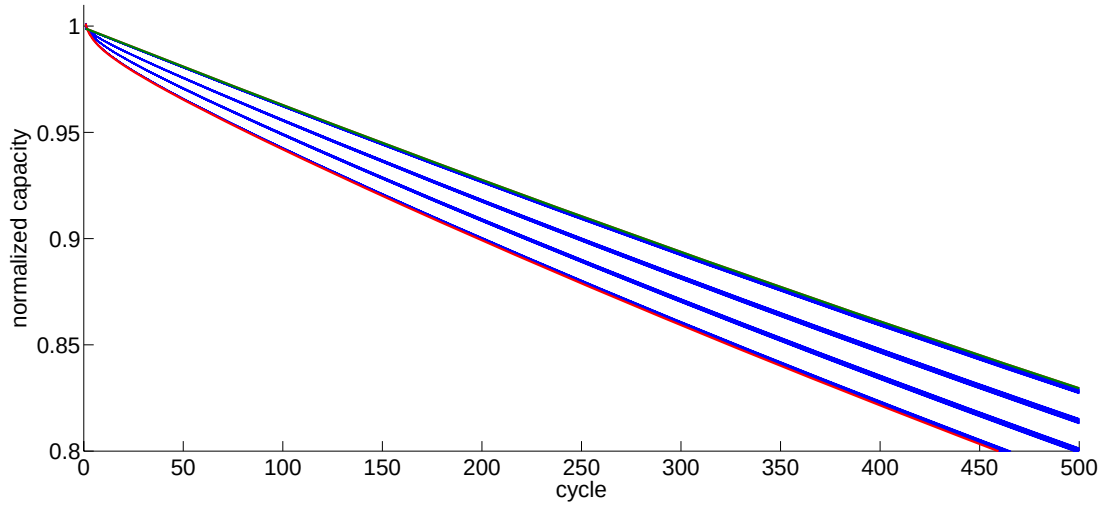

FIGURE 3.8.2: Plot of 80 capacity curves with low resolution in voltage (4 values) and high resolution in current (20 values)

In another simulation, we used the harshest value for $v_{\max}$, i.e., 1.02, and 100 linearly-spaced values for $i_{\max}$ in the region $\begin{bmatrix} 0.97 & 1.02 \end{bmatrix}$. All the 100 curves had normalized capacities of less than 0.80 after 500 cycles. However, by reversing the

scenario, i.e., using the harshest value for $i_{\max}$, i.e., 1.02, and 100 linearly-spaced values for $v_{\max}$ in the region $\begin{bmatrix} 0.97 & 1.02 \end{bmatrix}$, only 36 curves had normalized capacities that are less than 0.80 after 500 cycles. This again confirms the dominant effect of $v_{\max}$ over $i_{\max}$ on capacity fade.

3.9 Summary

In this chapter, we presented two models for estimating the normalized battery capacity, namely, the LAR-$\alpha\beta\gamma$ and the CVD. The former is a function of the number of cycles and the latter is a function of the number of cycles and two charge control parameters, viz., maximum terminal voltage of the battery ($v_{\max}$) and maximum charge current ($i_{\max}$). The accuracies of these models were explored by experimental data gathered from aging experiments performed on Samsung GS4 battery, and their dominance over the bi-exponential capacity model was demonstrated using the experimental data. The statistical dominance of LAR-$\alpha\beta\gamma$ over LS-BE was performed using Akaike Information Criterion (AIC). Using the CVD model, we also analyzed the effect of voltage and current on the capacity curves and we showed that $v_{\max}$, rather than $i_{\max}$, has a salient effect on the capacity fade of a battery.

Chapter 4

Battery Life Management

4.1 Introduction

As mentioned earlier, we analyze the optimal charging problem as a two-level strategy (level-I and level-II) that provides fast charging, while considering the battery life management by achieving a pre-specified desired "useful cycle life". At a lower and more detailed level (level-II), the objective is to find the optimal current profile to minimize the time-to-charge and energy loss during charging. The optimal charging algorithms require two parameters: maximum acceptable terminal voltage of the battery and the maximum current during charge. As observed by other researchers as well [100], these two parameters affect the life of the battery. Other factors that affect the life of the battery include depth of discharge, variations in charge and discharge currents, temperature, and duty cycle and pulse duration in the case of pulse charging, to name a few. In this chapter, we focus on the Level-I optimization, which is in fact battery life management.

The block diagram of level-I optimization is shown in Fig. 4.1.1. The measured capacity data from aging experiments is fed into a capacity fade model that uses the present cycle and the capacity of the battery obtained from the battery fuel gauge (BFG) to select the optimal charging parameters $v_{\max}$ and $i_{\max}$ to be used as control parameters in the charging algorithm.

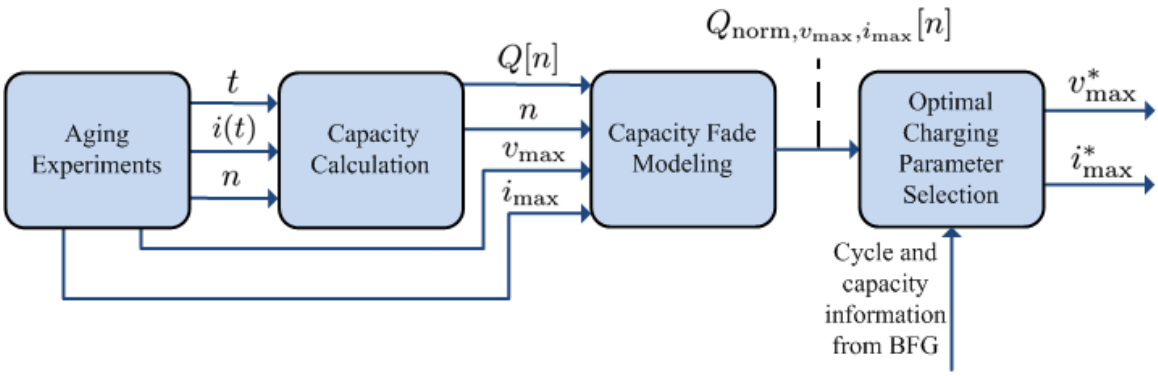

FIGURE 4.1.1: Block diagram of level-I optimization (battery life management)

This chapter is organized as follows. In section 4.2, we present a methodology that combines fast charging and battery life management via optimal charging parameter selection. Then, numerical illustrations for the optimal charging parameter selection are presented in section 4.3. Finally, in section 4.4, we summarize the chapter.

4.2 Fast Charging with Battery Life Management via Optimal Charging Parameter Selection

In this section, we present a battery life management policy, by formulating the problem as one of optimally selecting the control variables, i.e., $v_{\max}$ and $i_{\max}$. The goal is to find the optimal terminal voltage and maximum current so that we preserve the "Least Permissible Normalized Capacity" LPNC (typically 80%) at the end of the

"Nominal Cycle Life" NCL (typically 500) cycles of battery usage, while minimizing the time to charge. In this paper, for illustrative purposes, we use LPNC = 80% and NCL = 500 as the constraints for the optimal charging parameter selection.

Suppose we have K different candidate values for $v_{\max}$ and L different candidate values for $i_{\max}$ as follows:

$$v_{\max} \in \{v_1, v_2, \ldots, v_K\} \tag{4.2.1}$$

$$i_{\max} \in \{i_1, i_2, \ldots, i_L\} \tag{4.2.2}$$

This results in $K \times L$ different curves as follows:

$$Q_{\text{norm},kl}[n] = f(\underline{\alpha}, \underline{\beta}, \underline{\gamma}, \underline{u}_{kl}, n) \tag{4.2.3}$$

Figure 4.2.1 shows a graph of normalized capacity (Q_{norm}) versus cycle number (n).

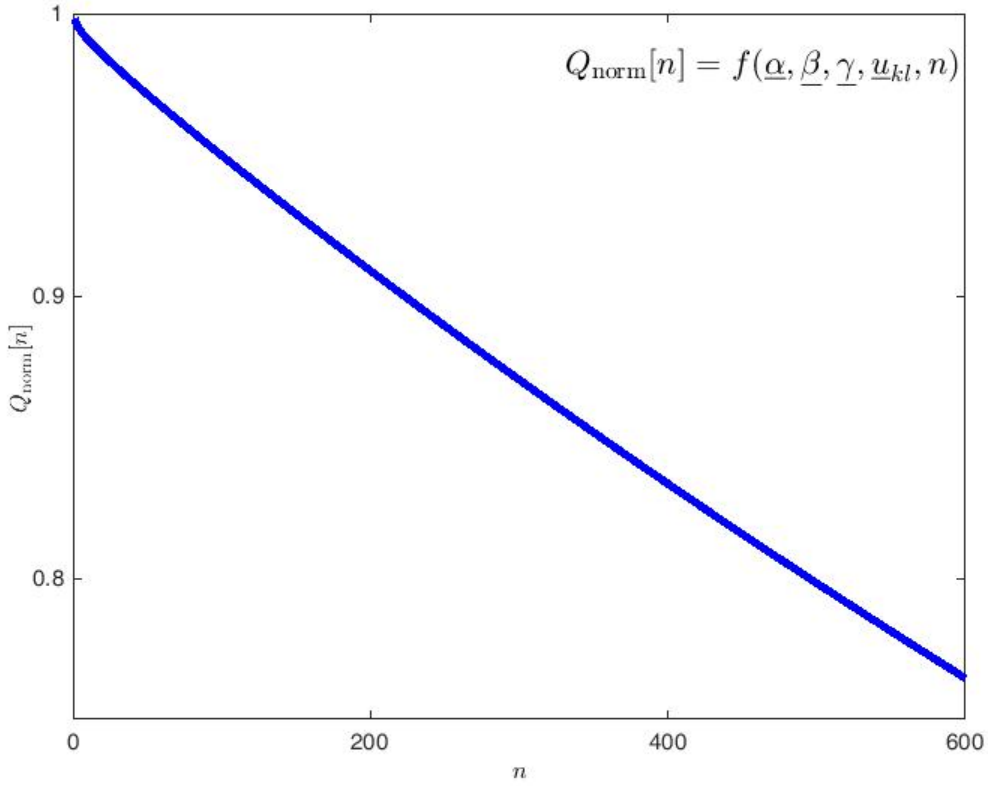

FIGURE 4.2.1: An example of normalized capacity as a function of cycle number

$$\underline{u}_{kl} = \begin{bmatrix} v_k & i_l \end{bmatrix}^T \qquad k \in \{1, 2, ..., K\} \qquad l \in \{1, 2, ..., L\} \tag{4.2.4}$$

Corresponding to curve $Q_{\text{norm},kl}[n]$, we define the "Useful Cycle Life" of UCL_{kl} as the cycle number at which the normalized capacity hits the "Least Permissible

Normalized Capacity" LPNC (say, 80%). Thus,

$$Q_{\text{norm},kl}[n] = f(\underline{\alpha}, \underline{\beta}, \underline{\gamma}, \underline{u}_{kl}, n) \geq \text{LPNC} \qquad \text{for} \quad n \leq \text{UCL}_{kl} \tag{4.2.5}$$

$$Q_{\text{norm},kl}[n] = f(\underline{\alpha}, \underline{\beta}, \underline{\gamma}, \underline{u}_{kl}, n) < \text{LPNC} \qquad \text{for} \quad n > \text{UCL}_{kl} \tag{4.2.6}$$

Figure 4.2.2 illustrates the definition of UCL_{kl}.

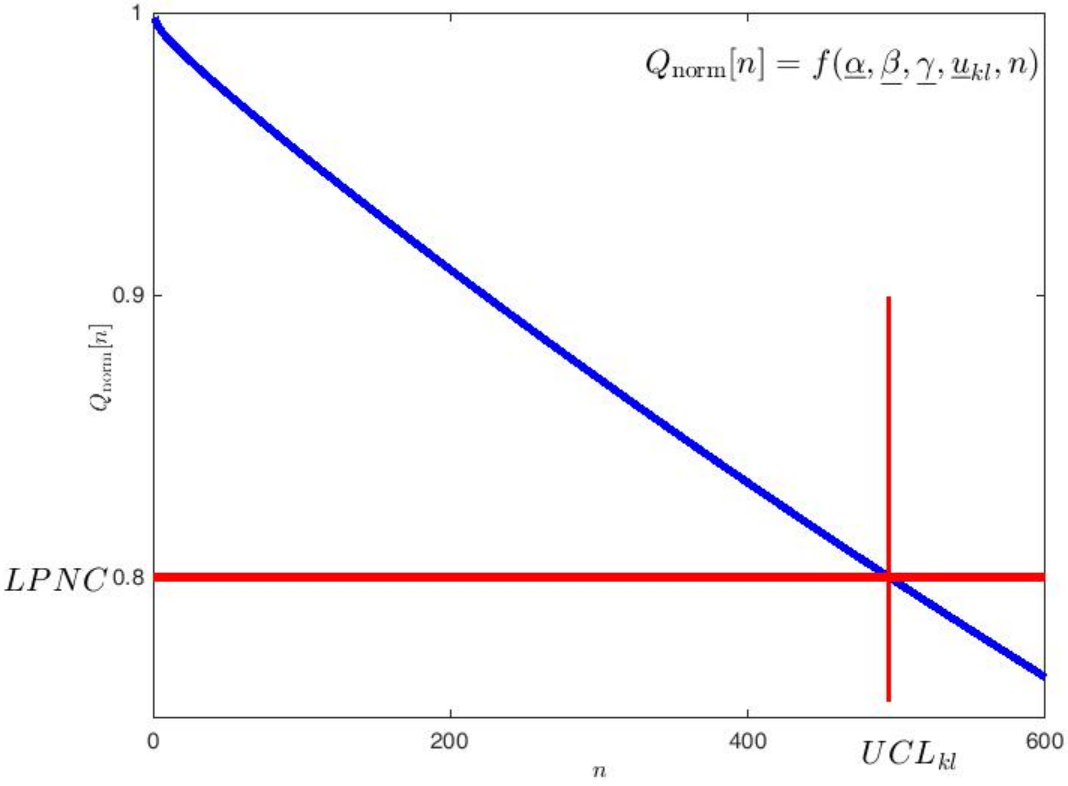

FIGURE 4.2.2: Illustration of Useful Cycle Life (UCL)

Assume that we have estimates of the number of cycles the battery has been exposed to and the normalized capacity of the battery at any time (for example

through BFG). Let PC denote the "Present Cycle" of the battery and let Q_{PC} be the estimated normalized capacity at cycle PC. If this battery is going to be charged using the control setting u_{kl}, its normalized capacity should correspond to the curve $Q_{\text{norm},kl}[n]$. Corresponding to the control setting $\underline{u}_{kl}$ and the normalized capacity of the battery at present cycle (Q_{PC}), we define the "Virtual Present Cycle" of the battery VPC_{kl} as follows:

$$Q_{\text{PC}} = f(\underline{\alpha}, \underline{\beta}, \underline{\gamma}, \underline{u}_{kl}, \text{VPC}_{kl}) \tag{4.2.7}$$

Figure 4.2.3 illustrates the definition of VPC_{kl}.

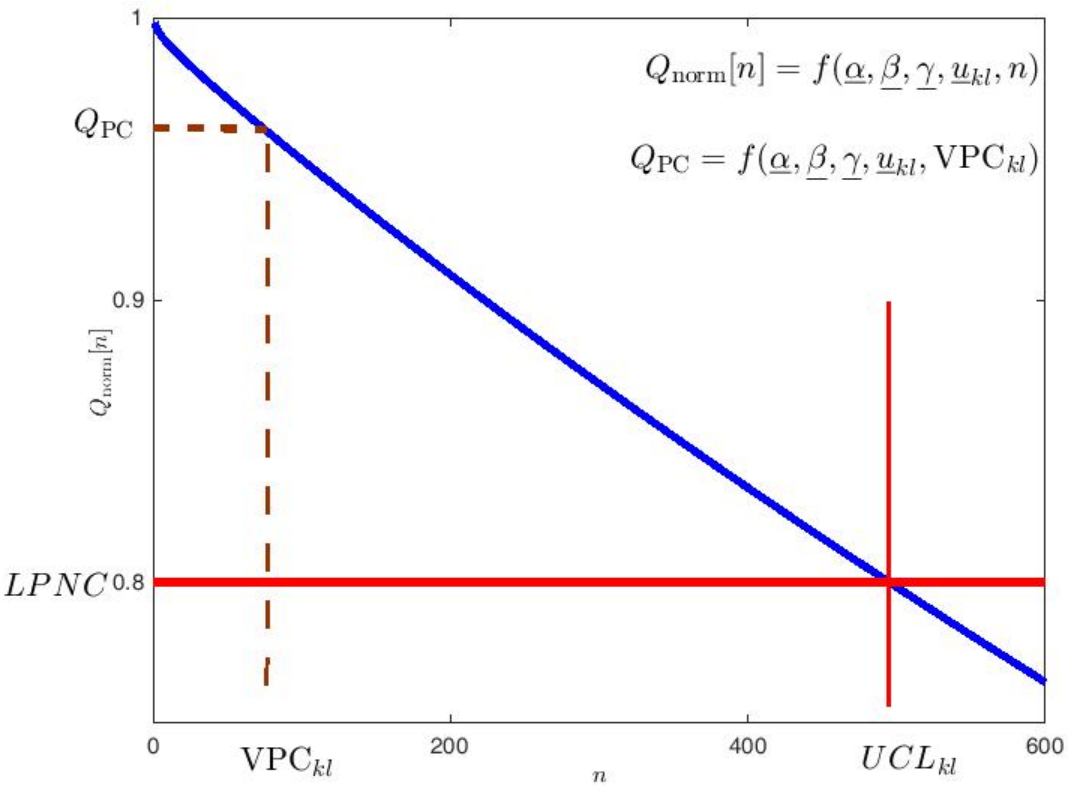

FIGURE 4.2.3: Illustration of Virtual Present Cycle (VPC)

Then, for a charge profile with control setting u_{kl}, the "Remaining Useful Cycle Life" RUCL_{kl} is defined as the difference between useful cycle life and the virtual present cycle; that is

$$\mathrm{RUCL}_{kl} = \mathrm{UCL}_{kl} - \mathrm{VPC}_{kl} \tag{4.2.8}$$

Figure 4.2.4 illustrates the definition of RUCL_{kl}.

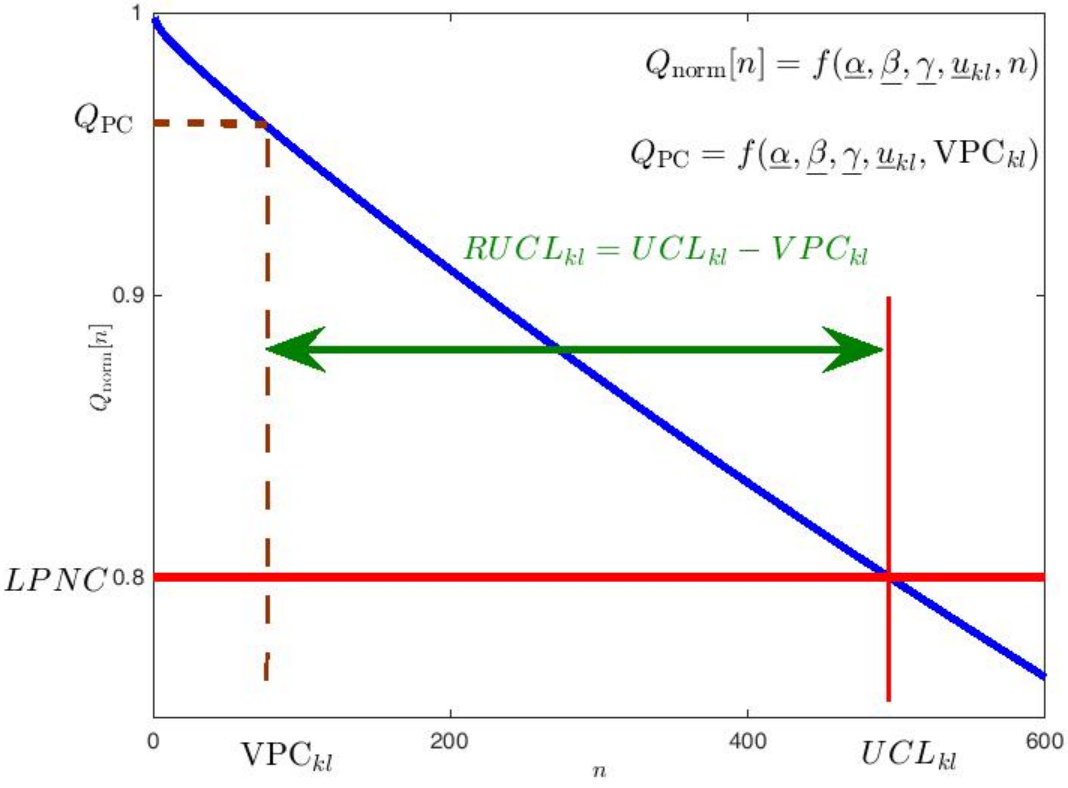

FIGURE 4.2.4: Illustration of Remaining Useful Cycle Life (RUCL)

Since the battery has already experienced PC cycles of usage, the "Expected Useful Cycle Life" of the battery EUCL_{kl} corresponding to the control setting u_{kl} is:

$$\mathrm{EUCL}_{kl} = \mathrm{PC} + \mathrm{RUCL}_{kl} \tag{4.2.9}$$

Inserting (4.2.8) into (4.2.9), we have

$$\mathrm{EUCL}_{kl} = (\mathrm{PC} - \mathrm{VPC}_{kl}) + \mathrm{UCL}_{kl} \tag{4.2.10}$$

The control setting u_{kl} is feasible if its corresponding expected useful cycle life is greater than or equal to "Nominal Cycle Life" NCL (say, 500 cycles); that is

$$\mathrm{EUCL}_{kl} \geq \mathrm{NCL} \tag{4.2.11}$$

Thus, the "Set of Feasible Control Settings" (SFCS) is

$$\mathrm{SFCS} = \{\underline{u}_{kl} | k \in \{1, 2, ..., K\}, l \in \{1, 2, ..., L\}, \mathrm{EUCL}_{kl} \geq \mathrm{NCL}\} \tag{4.2.12}$$

Among all feasible control settings, we select the one that minimizes the time to charge. This can be done as follows by using TTC_{kl}. For this purpose, the model-I [**?**] of the battery is simulated for different values of feasible control parameters, and among them the policy that results in the lowest TTC is selected. In the simulations, the CC-CV charging is used with the current in CC stage is selected as i_l and the terminal voltage in CV stage as v_k. This is equivalent to running the optimal charging algorithm with the objective of weighted sum of time-to-charge (TTC) and energy loss (EL) (referred to as OtE algorithm in section 2.2) with weight on TTC, i.e. ρ_{t},

being equal to $R_0 i_l^2$, where R_0 is the series resistance of the equivalent electrical circuit model. Note that for running model-I we need to know an estimate of the resistance of the battery, i.e. R_0, which can obtained through BFG. In the numerical results of this paper, however, we assume that R_0 is known.

Remark 4.2.1. Note that we can set a threshold SOC, s_{th}, for which we want to have the fastest TTC among all feasible strategies. The s_{th} threshold may be different from the desired final SOC after charging, i.e., s_{k_f}. For example, if we want to find the best policy, which maintains the life cycle constraints and results in the lowest time to charge for reaching an SOC of 50%, then we set $s_{\text{th}} = 0.50$.

Remark 4.2.2. Note that any capacity model can be used in place of the CVD model, as long as the model incorporates the control variables (the maximum terminal voltage and the maximum charge current).

The optimal strategy is then, selecting the control setting (among the SFCS) that provides the lowest time-to-charge:

$$(k^*, l^*) = \arg\limits_{k,l} \left(\min_{\underline{u}_{kl} \in \text{SFCS}} (\text{TTC}_{kl}) \right) \tag{4.2.13}$$

Remark 4.2.3. Another way to select the optimal strategy could be selecting the control setting (among the SFCS) that provides the lowest useful cycle life (UCL):

$$(k^*, l^*) = \arg\limits_{k,l} \left(\min_{\text{SFCS}} (\text{UCL}_{kl}) \right) \tag{4.2.14}$$

The optimal control setting is

$$\underline{u}^* = \begin{bmatrix} v^*_{\max} & i^*_{\max} \end{bmatrix}^T = \begin{bmatrix} v_{k^*} & i_{l^*} \end{bmatrix}^T \tag{4.2.15}$$

Figure 4.2.5 shows the detailed block diagram of battery life management (the level-I optimization problem). The setpoints of the diagram are LPNC and NCL, and s_{th}, the inputs to the optimization algorithm are PC, Q_{PC}, and R_0. These inputs may be estimated by BFG. In the numerical results of this thesis, we assume these inputs as known. The outputs of the diagram are $i^*_{\max}$ and $v^*_{\max}$, which are used in the level-II algorithms.

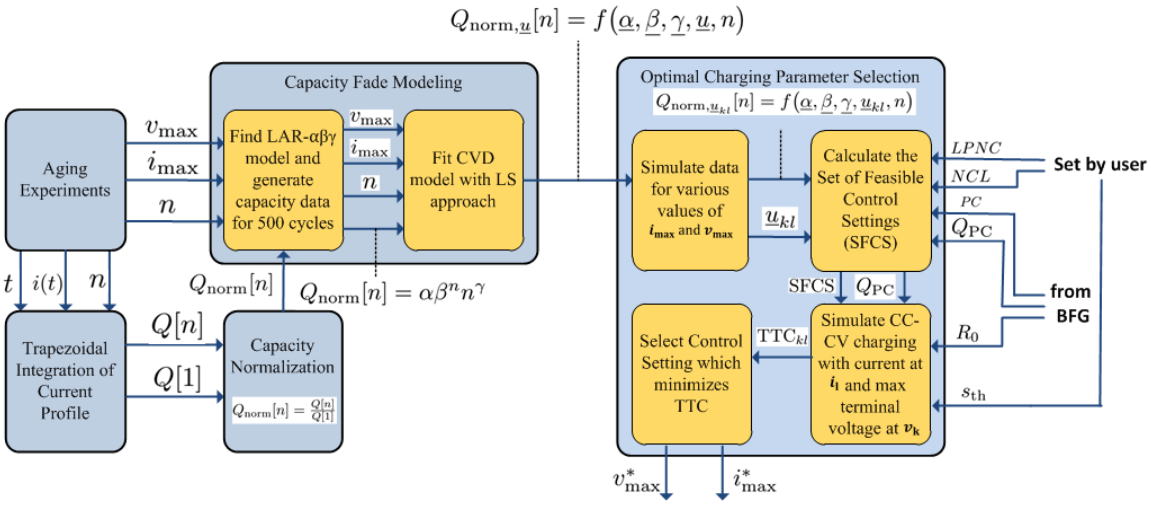

FIGURE 4.2.5: Battery life management block diagram

4.3 Numerical Illustration of Optimal Charging Parameter Selection

In this section, we illustrate the proposed optimal charging parameter selection method by numerical examples. Resolution of candidate values for control variables $v_{\max}$ and

$i_{\max}$ are selected as 0.01 and 0.1, respectively. Note that these control variables are in normalized form with the nominal value of 4.35 V and 2.6 A for voltage and current, respectively. In other words, the resolution of control variables are 0.0435 volts and 0.26 amperes. Eight different scenarios, each specified by four parameters (PC, Q_{PC}, R_0, and s_{th}), are illustrated. In all scenarios, we assume LPNC = 0.80 and NCL = 500. For a fair comparison of the effect of changing battery resistance R_0 and threshold SOC s_{th}, we have used the same PC (that is PC = 50) for all scenarios. The table of expected useful cycle life (EUCL) is shown for each scenario, in which the EUCL's of SFCS are shown in boldface, and the optimal control settings and the corresponding EUCL values are underlined. Note that the values for i_l and v_k are in "normalized (actual)" format and the actual values for currents and voltages (the values inside the parentheses) are in amperes and volts, respectively.

4.3.1 Scenario 1

$PC = 50$, $Q_{\mathrm{PC}} = 0.96$, $R_0 = 150\mathrm{m}\Omega$, and $s_{\mathrm{th}} = 0.50$. Table 4.3.1 shows the expected useful cycle life (EUCL) for this scenario. As seen from Table 4.3.1, the optimal control setpoints for this scenario are

$$\underline{u}^* = \begin{bmatrix} v^*_{\max} & i^*_{\max} \end{bmatrix}^T = \begin{bmatrix} 0.97 & 1.3 \end{bmatrix}^T \tag{4.3.1}$$

TABLE 4.3.1: Expected Useful Cycle Life (EUCL), for Scenario 1: $PC = 50$, $Q_{\mathrm{PC}} = 0.96$, $R_0 = 150\mathrm{m}\Omega$, and $s_{\mathrm{th}} = 0.50$

v_k \ i_l	0.7 (1.82)	0.8 (2.08)	0.9 (2.34)	1.0 (2.6)	1.1 (2.86)	1.2 (3.12)	1.3 (3.38)
0.97 (4.22)	**590**	**568**	**550**	**536**	**523**	**512**	**502**
0.98 (4.26)	**567**	**547**	**531**	**517**	**505**	494	485
0.99 (4.31)	**546**	**527**	**512**	498	488	478	469
1.00 (4.35)	**526**	**508**	495	482	472	462	454
1.01 (4.39)	**507**	491	477	466	456	448	440
1.02 (4.44)	489	474	461	450	442	433	426

Figure 4.3.1 shows the expected useful cycle life (EUCL) for "Scenario 1". The infeasible strategies are shown in red and the optimal strategy is shown in green.

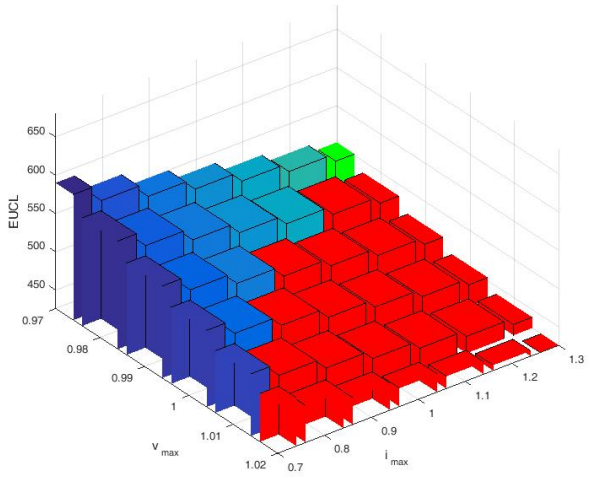

FIGURE 4.3.1: Expected Useful Cycle Life (EUCL) for Scenario 1
infeasible strategies are in red; optimal strategy is in green

4.3.2 Scenario 2

In this scenario, we consider a battery that has been used more mildly than in "Scenario 1".

$PC = 50$, $Q_{\text{PC}} = 0.99$, $R_0 = 150\text{m}\Omega$, and $s_{\text{th}} = 0.50$. Table 4.3.2 shows the expected useful cycle life (EUCL) for this scenario. As seen from Table 4.3.2, the optimal control setpoints for this scenario are

$$\underline{u}^* = \begin{bmatrix} v^*_{\max} & i^*_{\max} \end{bmatrix}^T = \begin{bmatrix} 1.00 & 1.3 \end{bmatrix}^T \tag{4.3.2}$$

As "Scenario 2" describes a battery that has been used very mildly, we see from Table 4.3.2 that the SFCS includes more members. Also note that for any setting, the EUCL corresponding to "Scenario 2" is higher than that of "Scenario 1". Note that compared to "Scenario 1", the optimal control setting in "Scenario 2" has a higher $v^*_{\max}$. This is because the battery has been used mildly before and hence it has more room to be exposed to higher terminal voltage without violating the constraint on useful life.

TABLE 4.3.2: Expected Useful Cycle Life (EUCL), for Scenario 2: $PC = 50$, $Q_{\text{PC}} = 0.99$, $R_0 = 150\text{m}\Omega$, and $s_{\text{th}} = 0.50$

v_k \ i_l	0.7 (1.82)	0.8 (2.08)	0.9 (2.34)	1.0 (2.6)	1.1 (2.86)	1.2 (3.12)	1.3 (3.38)
0.97 (4.22)	**681**	**656**	**635**	**618**	**603**	**590**	**578**
0.98 (4.26)	**652**	**629**	**610**	**593**	**579**	**566**	**556**
0.99 (4.31)	**624**	**603**	**585**	**569**	**556**	**545**	**534**
1.00 (4.35)	**599**	**578**	**561**	**547**	**534**	**523**	**513**
1.01 (4.39)	**573**	**555**	**538**	**525**	**513**	**503**	493
1.02 (4.44)	**549**	**532**	**517**	**504**	493	483	474

Figure 4.3.2 shows the expected useful cycle life (EUCL) for "Scenario 2". The infeasible strategies are shown in red and the optimal strategy is shown in green.

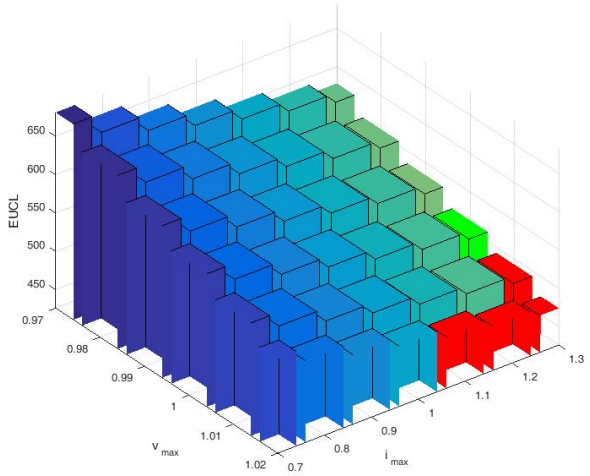

FIGURE 4.3.2: Expected Useful Cycle Life (EUCL) for Scenario 2
infeasible strategies are in red; optimal strategy is in green

In both "Scenario 1" and "Scenario 2", among all members of SFCS, the ones with higher current were selected. This may not always be the case if we increase s_{th} or if the resistance of the battery increases. Note that for low values of s_{th}, the charging time is inversely proportional to the injected current as all the strategies are in the CC stage, but for higher s_{th} some of the strategies may experience the CV stage as well; hence the best policy may not be the one with the highest current.

4.3.3 Scenario 3

In this scenario, we change s_{th} form 0.50 to 0.80 and all other conditions remain the same as in "Scenario 1".

$PC = 50$, $Q_{\text{PC}} = 0.96$, $R_0 = 150\text{m}\Omega$, and $s_{\text{th}} = 0.80$. Table 4.3.3 shows the expected useful cycle life (EUCL) for this scenario. As seen from Table 4.3.3, the optimal control setpoints for this scenario are

$$\underline{u}^* = \begin{bmatrix} v^*_{\max} & i^*_{\max} \end{bmatrix}^T = \begin{bmatrix} 0.98 & 1.1 \end{bmatrix}^T \tag{4.3.3}$$

TABLE 4.3.3: Expected Useful Cycle Life (EUCL), for Scenario 3: $PC = 50$, $Q_{\text{PC}} = 0.96$, $R_0 = 150\text{m}\Omega$, and $s_{\text{th}} = 0.80$

v_k \ i_l	0.7 (1.82)	0.8 (2.08)	0.9 (2.34)	1.0 (2.6)	1.1 (2.86)	1.2 (3.12)	1.3 (3.38)
0.97 (4.22)	**590**	**568**	**550**	**536**	**523**	**512**	**502**
0.98 (4.26)	**567**	**547**	**531**	**517**	**505**	494	485
0.99 (4.31)	**546**	**527**	**512**	498	488	478	469
1.00 (4.35)	**526**	**508**	495	482	472	462	454
1.01 (4.39)	**507**	491	477	466	456	448	440
1.02 (4.44)	489	474	461	450	442	433	426

Figure 4.3.3 shows the expected useful cycle life (EUCL) for "Scenario 3". The infeasible strategies are shown in red and the optimal strategy is shown in green.

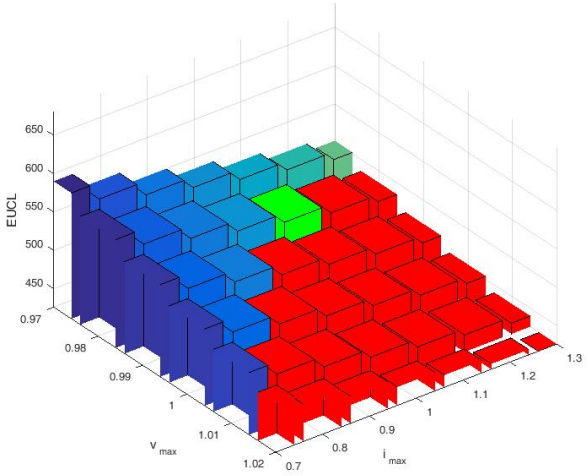

FIGURE 4.3.3: Expected Useful Cycle Life (EUCL) for Scenario 3
infeasible strategies are in red; optimal strategy is in green

4.3.4 Scenario 4

In this scenario, we assume that the resistance of the battery is 200mΩ instead of 150mΩ as used in "Scenario 1" and we assume that all the other conditions remain the same as in "Scenario 1".

$PC = 50$, $Q_{\text{PC}} = 0.96$, $R_0 = 200\text{m}\Omega$, and $s_{\text{th}} = 0.50$. Table 4.3.4 shows the expected useful cycle life (EUCL) for this scenario. As seen from Table 4.3.4, the optimal control setpoints for this scenario are the same as in "Scenario 3":

$$\underline{u}^* = \begin{bmatrix} v^*_{\text{max}} & i^*_{\text{max}} \end{bmatrix}^T = \begin{bmatrix} 0.98 & 1.1 \end{bmatrix}^T \tag{4.3.4}$$

TABLE 4.3.4: Expected Useful Cycle Life (EUCL), for Scenario 4: $PC = 50$, $Q_{\mathrm{PC}} = 0.96$, $R_0 = 200\mathrm{m}\Omega$, and $s_{\mathrm{th}} = 0.50$

v_k \ i_l	0.7 (1.82)	0.8 (2.08)	0.9 (2.34)	1.0 (2.6)	1.1 (2.86)	1.2 (3.12)	1.3 (3.38)
0.97 (4.22)	**590**	**568**	**550**	**536**	**523**	**512**	**502**
0.98 (4.26)	**567**	**547**	**531**	**517**	**505**	494	485
0.99 (4.31)	**546**	**527**	**512**	498	488	478	469
1.00 (4.35)	**526**	**508**	495	482	472	462	454
1.01 (4.39)	**507**	491	477	466	456	448	440
1.02 (4.44)	489	474	461	450	442	433	426

Figure 4.3.4 shows the expected useful cycle life (EUCL) for "Scenario 4". The infeasible strategies are shown in red and the optimal strategy is shown in green.

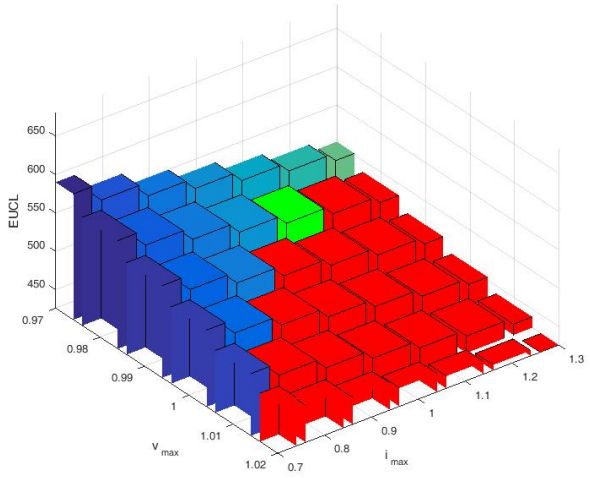

FIGURE 4.3.4: Expected Useful Cycle Life (EUCL) for Scenario 4
infeasible strategies are in red; optimal strategy is in green

4.3.5 Scenario 5

In this, we assume that the resistance is higher (250mΩ) than that of Scenario 4 (200mΩ). Comparing Table 4.3.5 with Table 4.3.4, we can see that the level of optimal current decreases further, and the optimal strategy moves down along the boundary between the feasible and infeasible control settings.

$PC = 50$, $Q_{\mathrm{PC}} = 0.96$, $R_0 = 250\mathrm{m}\Omega$, and $s_{\mathrm{th}} = 0.50$. Table 4.3.5 shows the expected useful cycle life (EUCL) for this scenario. As seen from Table 4.3.5, the optimal control setpoints for this scenario are

$$\underline{u}^* = \begin{bmatrix} v^*_{\max} & i^*_{\max} \end{bmatrix}^T = \begin{bmatrix} 0.99 & 0.9 \end{bmatrix}^T \tag{4.3.5}$$

TABLE 4.3.5: Expected Useful Cycle Life (EUCL), for Scenario 5: $PC = 50$, $Q_{\mathrm{PC}} = 0.96$, $R_0 = 250\mathrm{m}\Omega$, and $s_{\mathrm{th}} = 0.50$

v_k \ i_l	0.7 (1.82)	0.8 (2.08)	0.9 (2.34)	1.0 (2.6)	1.1 (2.86)	1.2 (3.12)	1.3 (3.38)
0.97 (4.22)	**590**	**568**	**550**	**536**	**523**	**512**	**502**
0.98 (4.26)	**567**	**547**	**531**	**517**	**505**	494	485
0.99 (4.31)	**546**	**527**	**512**	498	488	478	469
1.00 (4.35)	**526**	**508**	495	482	472	462	454
1.01 (4.39)	**507**	491	477	466	456	448	440
1.02 (4.44)	489	474	461	450	442	433	426

Figure 4.3.5 shows the expected useful cycle life (EUCL) for "Scenario 5". The infeasible strategies are shown in red and the optimal strategy is shown in green.

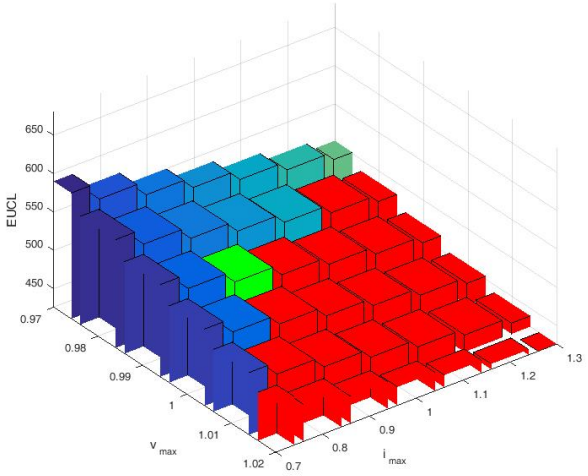

FIGURE 4.3.5: Expected Useful Cycle Life (EUCL) for Scenario 5
infeasible strategies are in red; optimal strategy is in green

4.3.6 Scenario 6

In this scenario, we assume that the resistance is even higher (300mΩ) than that of Scenario 5 (250mΩ). Comparing Table 4.3.6 with Table 4.3.5, we can see that the level of optimal current decreases further, and the optimal strategy moves down along the boundary between the feasible and infeasible control settings.

$PC = 50$, $Q_{\text{PC}} = 0.96$, $R_0 = 300\text{m}\Omega$, and $s_{\text{th}} = 0.50$. Table 4.3.5 shows the expected useful cycle life (EUCL) for this scenario. As seen from Table 4.3.5, the optimal control setpoints for this scenario are

$$\underline{u}^* = \begin{bmatrix} v^*_{\text{max}} & i^*_{\text{max}} \end{bmatrix}^T = \begin{bmatrix} 1.00 & 0.8 \end{bmatrix}^T \tag{4.3.6}$$

TABLE 4.3.6: Expected Useful Cycle Life (EUCL), for Scenario 6: $PC = 50$, $Q_{\text{PC}} = 0.96$, $R_0 = 300\text{m}\Omega$, and $s_{\text{th}} = 0.50$

v_k \ i_l	0.7 (1.82)	0.8 (2.08)	0.9 (2.34)	1.0 (2.6)	1.1 (2.86)	1.2 (3.12)	1.3 (3.38)
0.97 (4.22)	**590**	**568**	**550**	**536**	**523**	**512**	**502**
0.98 (4.26)	**567**	**547**	**531**	**517**	**505**	494	485
0.99 (4.31)	**546**	**527**	**512**	498	488	478	469
1.00 (4.35)	**526**	**508**	495	482	472	462	454
1.01 (4.39)	**507**	491	477	466	456	448	440
1.02 (4.44)	489	474	461	450	442	433	426

Figure 4.3.6 shows the expected useful cycle life (EUCL) for "Scenario 6". The infeasible strategies are shown in red and the optimal strategy is shown in green.

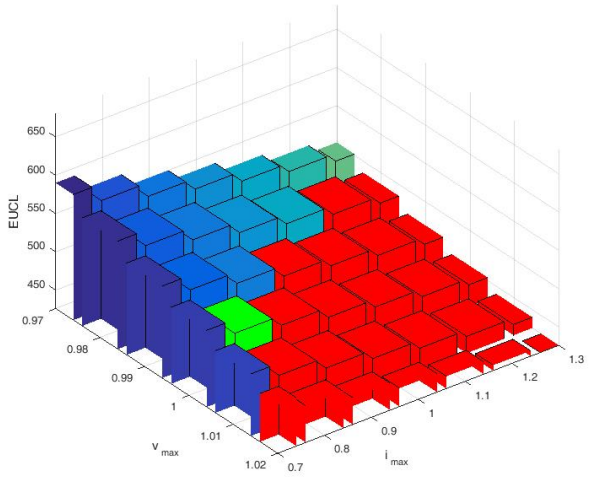

FIGURE 4.3.6: Expected Useful Cycle Life (EUCL) for Scenario 6
infeasible strategies are in red; optimal strategy is in green

4.3.7 Scenario 7

$PC = 50$, $Q_{\mathrm{PC}} = 0.97$, $R_0 = 150\mathrm{m}\Omega$, and $s_{\mathrm{th}} = 0.50$. Table 4.3.7 shows the expected useful cycle life (EUCL) for this scenario. As seen from Table 4.3.7, the optimal control setpoints for this scenario are

$$\underline{u}^* = \begin{bmatrix} v^*_{\max} & i^*_{\max} \end{bmatrix}^T = \begin{bmatrix} 0.98 & 1.3 \end{bmatrix}^T \tag{4.3.7}$$

TABLE 4.3.7: Expected Useful Cycle Life (EUCL), for Scenario 7: $PC = 50$, $Q_{\mathrm{PC}} = 0.97$, $R_0 = 150\mathrm{m}\Omega$, and $s_{\mathrm{th}} = 0.50$

v_k \ i_l	0.7 (1.82)	0.8 (2.08)	0.9 (2.34)	1.0 (2.6)	1.1 (2.86)	1.2 (3.12)	1.3 (3.38)
0.97 (4.22)	**620**	**598**	**579**	**563**	**550**	**538**	**527**
0.98 (4.26)	**596**	**575**	**558**	**543**	**530**	**519**	**510**
0.99 (4.31)	**573**	**554**	**538**	**523**	**512**	**502**	492
1.00 (4.35)	**552**	**533**	**518**	**505**	494	484	475
1.01 (4.39)	**531**	**514**	499	488	477	468	460
1.02 (4.44)	**512**	496	482	471	462	452	445

Figure 4.3.7 shows the expected useful cycle life (EUCL) for "Scenario 7". The infeasible strategies are shown in red and the optimal strategy is shown in green.

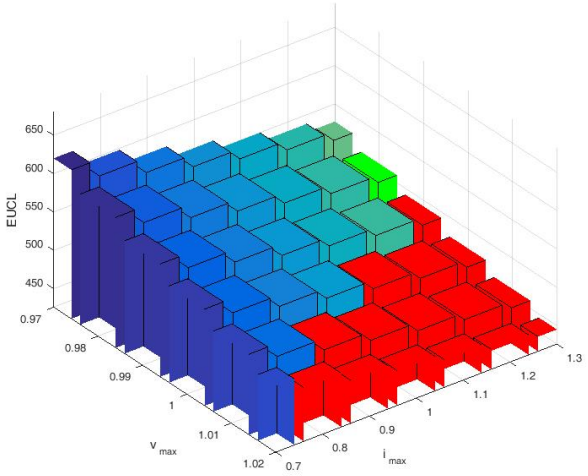

FIGURE 4.3.7: Expected Useful Cycle Life (EUCL) for Scenario 7
infeasible strategies are in red; optimal strategy is in green

4.3.8 Scenario 8

$PC = 50$, $Q_{\text{PC}} = 0.98$, $R_0 = 150\text{m}\Omega$, and $s_{\text{th}} = 0.50$. Table 4.3.8 shows the expected useful cycle life (EUCL) for this scenario. As seen from Table 4.3.8, the optimal control setpoints for this scenario are

$$\underline{u}^* = \begin{bmatrix} v^*_{\text{max}} & i^*_{\text{max}} \end{bmatrix}^T = \begin{bmatrix} 0.99 & 1.3 \end{bmatrix}^T \tag{4.3.8}$$

TABLE 4.3.8: Expected Useful Cycle Life (EUCL), for Scenario 8: $PC = 50$, $Q_{\mathrm{PC}} = 0.98$, $R_0 = 150\mathrm{m}\Omega$, and $s_{\mathrm{th}} = 0.50$

v_k \ i_l	0.7 (1.82)	0.8 (2.08)	0.9 (2.34)	1.0 (2.6)	1.1 (2.86)	1.2 (3.12)	1.3 (3.38)
0.97 (4.22)	**651**	**627**	**607**	**591**	**577**	**564**	**553**
0.98 (4.26)	**624**	**603**	**584**	**568**	**555**	**543**	**533**
0.99 (4.31)	**599**	**579**	**562**	**547**	**535**	**524**	**514**
1.00 (4.35)	**576**	**557**	**541**	**527**	**515**	**505**	496
1.01 (4.39)	**553**	**536**	**520**	**508**	497	487	479
1.02 (4.44)	**532**	**516**	**501**	489	479	470	462

Figure 4.3.8 shows the expected useful cycle life (EUCL) for "Scenario 8". The infeasible strategies are shown in red and the optimal strategy is shown in green.

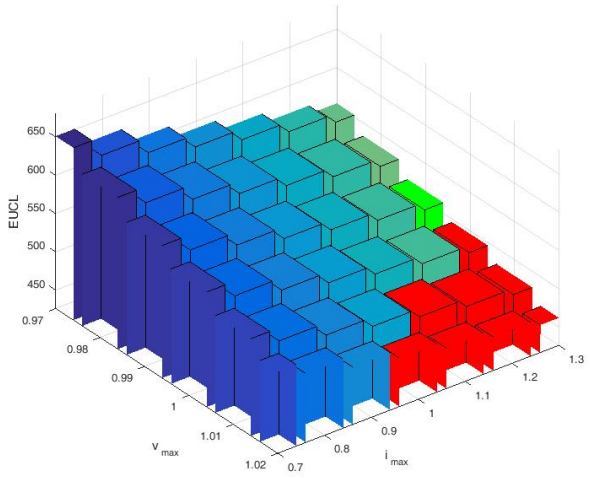

FIGURE 4.3.8: Expected Useful Cycle Life (EUCL) for Scenario 8
infeasible strategies are in red; optimal strategy is in green

Remark 4.3.1. That in Scenarios 4-6, increasing the resistance resulted in an optimal policy with lower current. This suggests that $i_{\max}$, rather than $v_{\max}$, has a salient effect on power fade. Figure 4.3.9 shows the effect of power fade (increase in the series resistance) on the expected useful cycle life (EUCL) of battery.

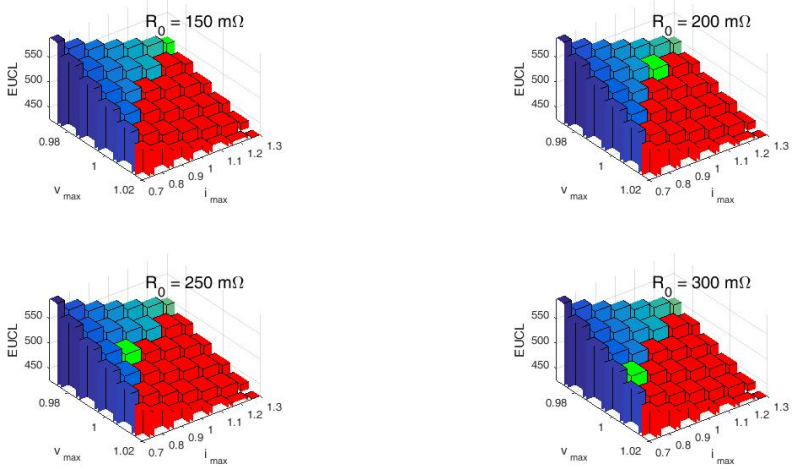

FIGURE 4.3.9: Effect of power fade (increase in the series resistance) on the expected useful cycle life (EUCL) of battery

The animation of the effect of power fade on EUCL can be downloaded from [1].

Remark 4.3.2. That in Scenarios 1-2 and 7-8, increasing the present capacity (Q_{PC}) resulted in an optimal policy with higher voltage. This suggests that $v_{\max}$, rather than $i_{\max}$, has a salient effect on capacity fade. This is consistent with the results from section 3.8. Figure 4.3.10 shows the effect of capacity fade on the expected useful cycle life of battery.

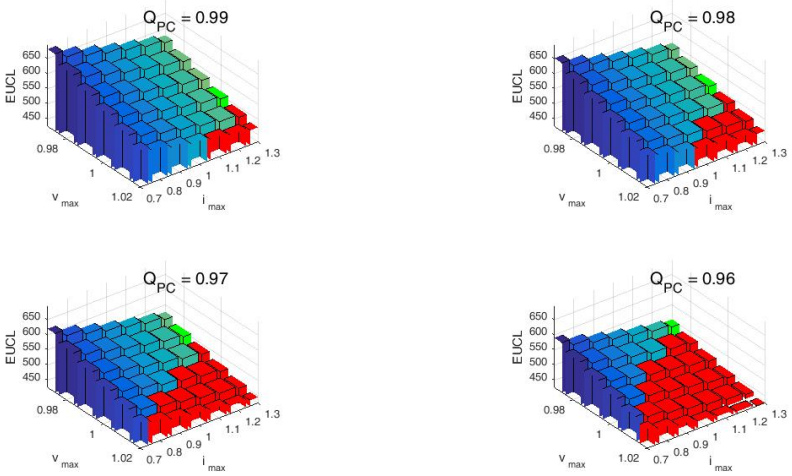

FIGURE 4.3.10: Effect of capacity fade on the expected useful cycle life (EUCL) of battery

The animation of the effect of capacity fade on EUCL can be downloaded from [1].

Figure 4.3.11 summarizes the above remarks visually. The width of the causal arrows represents their strength.

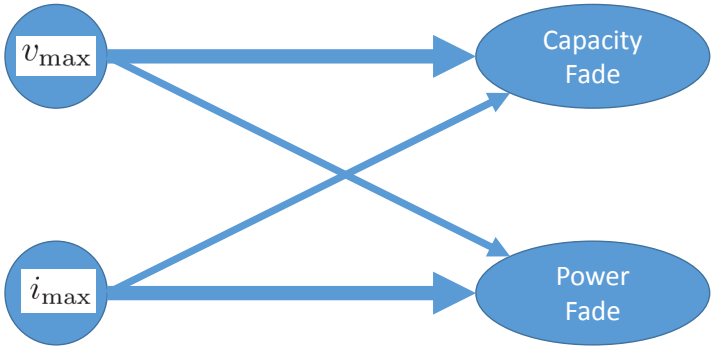

FIGURE 4.3.11: Effect of $v_{\max}$ and $i_{\max}$ on power fade and capacity fade

Since the main cause of increasing the resistance is solid-electrolyte interphase (SEI) formation and the main cause of decreasing capacity is Li plating, we can say that higher currents are significant causal factors for SEI formation, while higher terminal voltages are major causes of Li plating.

4.3.9 Summary of Scenarios and Some Insights

Table 4.3.9 shows the parameters and the optimal policy for each scenario.

TABLE 4.3.9: Scenarios: parameters and optimal policy

Scenario	Parameters				Optimal Policy (normalized)		Optimal Policy (actual)	
	PC	Q_{PC}	$R_0(\text{m}\Omega)$	s_{th}	v^*_{max}	i^*_{max}	v^*_{max}(V)	i^*_{max}(A)
1	50	0.96	150	0.50	0.97	1.3	4.22	3.38
2	50	0.99	150	0.50	1.00	1.3	4.35	3.38
3	50	0.96	150	0.80	0.98	1.1	4.26	2.86
4	50	0.96	200	0.50	0.98	1.1	4.26	2.86
5	50	0.96	250	0.50	0.99	0.9	4.31	2.34
6	50	0.96	300	0.50	1.00	0.8	4.35	2.08
7	50	0.97	150	0.50	0.98	1.3	4.26	3.38
8	50	0.98	150	0.50	0.99	1.3	4.31	3.38

The following insights can be drawn form Tables 4.3.1 through 4.3.9:

1. For scenarios with mild usage of battery and low values of s_{th} (as in "Scenario 1" and "Scenario 2"), the optimal strategy is the one among the feasible candidates (members of SFCS) that has the highest current.

2. If the battery is treated mildly, the optimal strategy yields higher values of v^*_{max} and i^*_{max}. For example, the battery in "Scenario 2" is treated more mildly than

the battery in "Scenario 1", and consequently, the $v^*_{\max}$ (1.00 normalized or 4.35 volts) in "Scenario 2" is higher than that (0.97 normalized or 4.22 volts) of "Scenario 1".

3. For scenarios with higher values of s_{th} (as in "Scenario 3"), the optimal strategy yields lower values of $i^*_{\max}$ and higher values of $v^*_{\max}$.

4. The increase in battery resistance (compare Scenarios 4, 5, and 6) results in lower values of $i^*_{\max}$ and higher values of $v^*_{\max}$.

5. $i_{\max}$, rather than $v_{\max}$, has a salient effect on power fade.

6. $v_{\max}$, rather than $i_{\max}$, has a salient effect on capacity fade. This is consistent with the results from section 3.8.

4.4 Summary

In this chapter, we presented a battery life management policy by developing a procedure for optimal charging parameter selection. The proposed approach finds the best $v_{\max}$ and $i_{\max}$ to achieve a desired cycle life (for example, 500 cycles), while maintaining the normalized capacity above a desired threshold (for example, 80%) and attaining the fastest possible time-to-charge. The method was illustrated via numerical results. The optimal setpoint depends on the desired state of charge (denoted by s_{th}) for which we aim to attain the fastest charging time. It also depends on the resistance of the battery, i.e., R_0. Simulation results show that a low threshold on state of charge (s_{th}) and a low battery resistance result in an optimal setpoint with the highest $i_{\max}$ among the set of feasible control settings, while increasing s_{th} and the

battery resistance result in moving the optimal setpoint to lower values of $i_{\max}$ and higher values of $v_{\max}$. From the discussion of the different scenarios, we concluded that $i_{\max}$, rather than $v_{\max}$, has a salient effect on power fade, and $v_{\max}$, rather than $i_{\max}$, has a salient effect on capacity fade. The latter is consistent with the results from section 3.8.

Chapter 5

Fault Detection, Diagnosis and Prognosis

5.1 Introduction

With increasing number of subsystems and components in complex engineered systems, the need for system monitoring, anomaly (fault) detection and root cause analysis is paramount for improved system availability. However, the process of detecting and isolating faults in complex systems is challenging. This is because:

- The numbers of faults and monitoring signals ("processed sensor measurements", "tests", "symptoms", "visual observations") in these systems are large (running into tens of thousands).
- Each test outcome may be caused by faults in multiple components of possibly multiple subsystems ("many-to-many" fault-test relationships).

- Faults propagate from one subsystem to another ("cross-subsystem fault propagation") with delays.
- Test outcomes, which are uncertain, are observed with delays caused by fault propagation, computation and communication.
- Simultaneous occurrence of multiple faults is frequent.

This makes traditional single-fault diagnosis approaches untenable. Uncertain test outcomes pose particularly difficult challenges to fault diagnosis: while, in a perfect binary test outcome situation, a passed test indicates the normal status of its associated components and a failed test implies the existence of at least one faulty component associated with the test, neither can be inferred when the tests are imperfect. In the binary test outcome case, an imperfect test outcome may be reported as *passed*, even when there are faulty component(s) associated with the test, a situation referred to as *imperfect (missed) detection*. On the other hand, an imperfect test outcome may be reported as *failed*, even though there is no faulty component associated with the test, a condition referred to as a *false alarm*.

In broad terms, fault diagnosis problems can be categorized into two groups: passive monitoring and active monitoring ("probing"). In passive monitoring, the fault diagnosis subsystem ("diagnoser") relies on synchronous or asynchronous availability of test outcomes to detect abnormal conditions in the system and to isolate the faulty component or components in the system. This is also termed *abductive reasoning*. One application of passive monitoring is in disease diagnosis, such as Quick Medical Reference Decision-Theoretic (QMR-DT) problem, wherein bi-partite belief networks are used to model the probabilistic cause-effect relations of a set of diseases and a set of findings [169], [200]. On the other hand, in active probing, the aim is to adaptively

sequence the application of tests based on the outcomes of previously applied tests in order to minimize the expected troubleshooting time or the expected testing cost. Evidently, hybrid passive and active monitoring (e.g., passive monitoring followed by active probing to troubleshoot problems) is a common practice in complex system diagnosis.

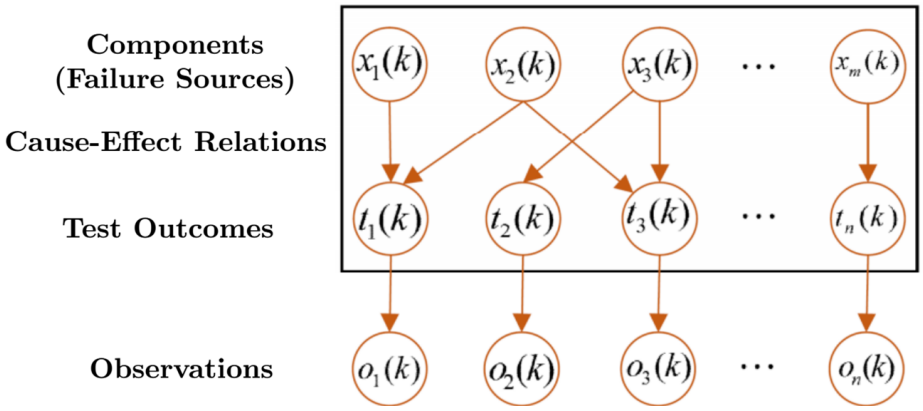

FIGURE 5.1.1: Tripartite digraph of fault diagnosis system

Graphical models combine graph theory and probability theory into an elegant formalism for visualizing models, gaining insights into conditional independence properties, inference and learning. Since fault diagnosis is inherently an inference problem, it is natural to employ graphical models for fault diagnosis. In this vein, a fault diagnosis system can be conceptualized as a tripartite directed graph (digraph) as shown in Fig. 5.1.1. The first (top) layer contains the components (failure modes or failure sources) and the second (middle) layer is comprised of test outcomes. The cause-effect relations between the component health states (herein termed failure source states) and the test outcomes may be perfect or imperfect (probabilistic). The third

(bottom) layer encompasses the observations of test outcomes, which may be perfect or imperfect, observed synchronously or asynchronously and, in the synchronous case, not all observations of test outcomes may be available at each epoch. Note that the observations may be different from the test outcomes, for example, due to uncertainty and communication errors. When the observations are perfect, we have $o_j(k) = t_j(k)$ and the tri-partite digraph is reduced to a bipartite one. In the following, we assume that observations are perfect and represent the system as a bipartite digraph. Also in the case of static fault diagnosis, the dependence on time is omitted in the bipartite digraph.

The problem has three basic elements, namely, failure sources (associated with components), tests, and dependency relations between failure sources and tests. Each of these elements can be abstracted in various ways to capture the nature of fault diagnosis problem in a complex system. For example, failure sources associated with a component can be permanent (static) or intermittent (dynamic). They may have binary states (normal, abnormal) or multi-valued states (nominal and various degraded modes of operation). The failure sources may be independent or coupled (see Fig. 5.1.2). In the same vein, a test can be categorized as having binary or multi-valued outcomes, and the relationship between the failure sources and test outcomes can be perfect or imperfect, as alluded to earlier.

For ease of exposition and simplicity of notation, we consider failure sources and test outcomes with binary states. Fig. 5.1.3(a) shows a component having binary (0-1) states and a test outcome also with binary (0-1) states having a perfect dependency relationship. Evidently, in this case, with probability one, $x_i = 1$ is mapped to $t_j = 1$, and $x_i = 0$ to $t_j = 0$.

Fig. 5.1.3(b) shows the dependency relationship of a failure source and a test

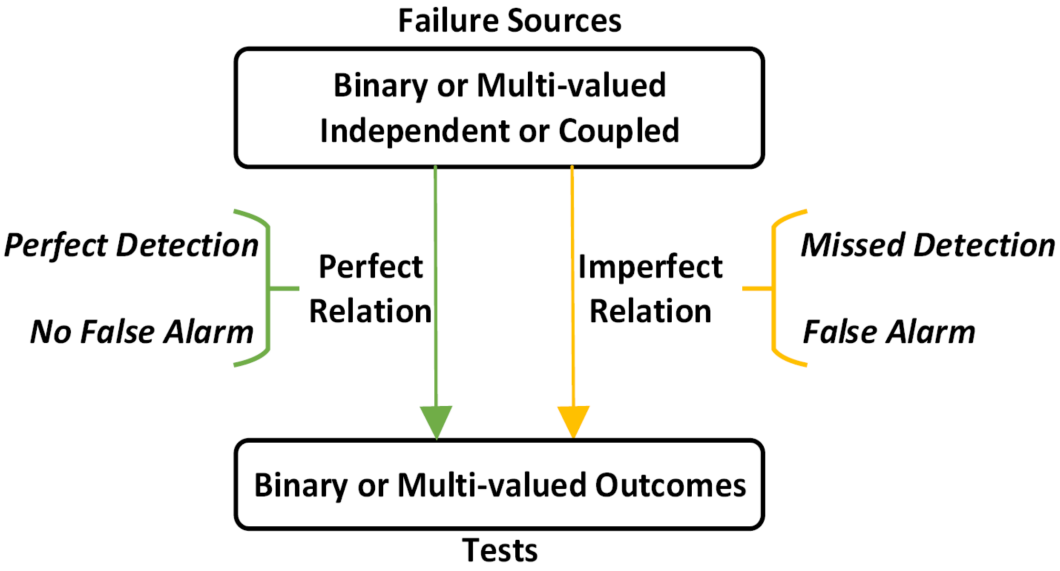

FIGURE 5.1.2: Modeling abstractions in fault diagnosis subsystems

outcome in an imperfect test setting. An imperfect binary relation can be represented by probability of detection and probability of false alarm as follows.

Probability of Detection: If $x_i = 1$, then there is a probability Pd_{ij} that test t_j fails. Here, Pd_{ij} denotes the probability of detection. Formally, $Pd_{ij} = \Pr(t_j = 1 | x_i = 1)$.

Probability of False Alarm: If $x_i = 0$, then there is a probability Pf_{ij} that test t_j fails. Here, Pf_{ij} denotes the probability of false alarm. Formally, $Pf_{ij} = \Pr(t_j = 1 | x_i = 0)$.

In the sequel, we discuss the static and dynamic form of multiple fault

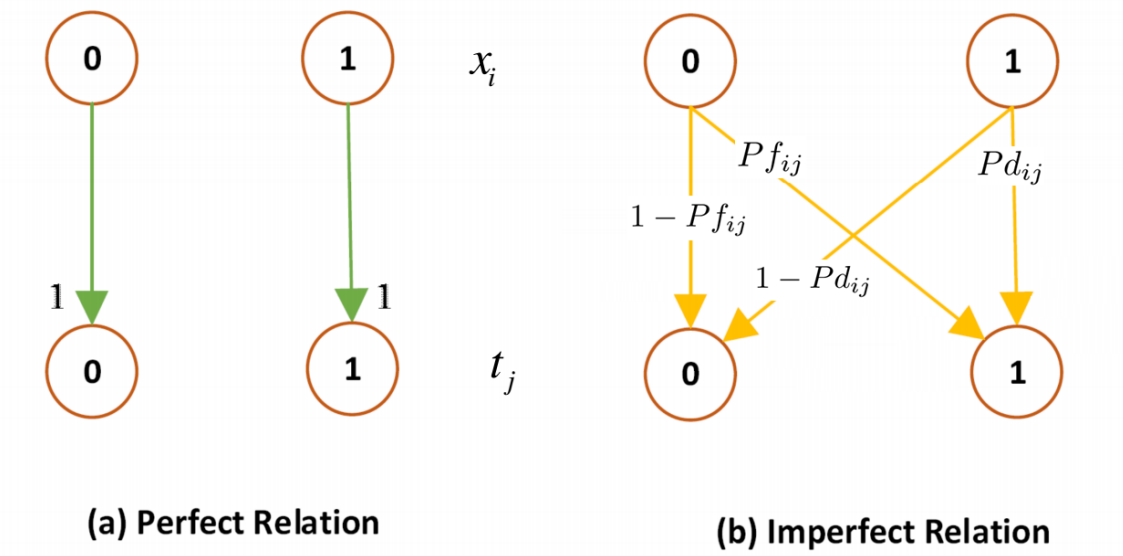

FIGURE 5.1.3: Perfect and imperfect relations of a failure source and a test outcome

diagnosis and also passive and active monitoring using this simplified model. Extensions of the method to coupled and delayed failure source state propagation, and delayed observations can be found in [170], [103], [180], [104], and [204].

5.2 Static Multiple Fault Diagnosis

In this section, we consider the multiple fault diagnosis problem in a static context, and we refer to it as static multiple fault diagnosis (SMFD). The SMFD problem is comprised of the following:

- The system consists of m components c_1, c_2, $\cdots$, c_m. Without loss of generality, a single failure mode is associated with each component. The failure modes are assumed to be conditionally independent. We let $S = \{s_1, s_2, \ldots, s_m\}$ be the set of independent potential failure modes (failure sources), respectively, associated

with the system components c_1, c_2, $\cdots$, c_m.

- To each component (potential failure source), c_i (s_i) is assigned a binary state variable x_i, where $x_i = 1$ represents the fault state of the component and $x_i = 0$ represents the normal state of the component.

- Each potential failure source is assumed to have a prior probability p_{s_i} of being faulty; in other words, $\Pr(x_i = 1) = p_{s_i}$.

- The system is assumed to have n tests, $\mathbf{t} = \{t_1, t_2, \cdots, t_n\}$.

- Tests are assumed to be independent.

- When test t_j has a pass outcome, it is represented by $t_j = 0$, otherwise by $t_j = 1$.

- The cause-effect relation between the potential failure sources and the tests are assumed to be probabilistic with detection probabilities and false alarm probabilities, as discussed in the previous section.

- In a real-world system, if component c_i is associated with test t_j , the detection probability Pd_{ij} is a number close to 1, for example, in the range $[0.75, 1]$ and the false alarm probabilityPf_{ij} is a number close to 0, for example, in the range $[0, 0.20]$. The situation that the component c_i is not associated with test t_j is represented by $Pd_{ij} = Pf_{ij} = 0$.

- We represent the states of failures sources as $\mathbf{x}$. In other words $\mathbf{x} = \{x_1, x_2, \ldots, x_m\}$.

Based on the above assumptions, the problem of SMFD is defined as follows:

Static Multiple Fault Diagnosis (SMFD) Problem: Given T, a subset of all test outcomes $\mathbf{t}$, i.e., $T \subseteq \mathbf{t}$, what are the most likely states of failure sources, $\mathbf{x}$?

Formally, we can represent the problem as follows:

$$\hat{\mathbf{x}} = \arg \max_{\mathbf{x}} \Pr(\mathbf{x}|T). \tag{5.2.1}$$

Using Bayes' rule, we can write $\Pr(\mathbf{x}|T)$ as

$$\Pr(\mathbf{x}|T) = \frac{\Pr(T|\mathbf{x})\Pr(\mathbf{x})}{\Pr(T)}. \tag{5.2.2}$$

Since maximization of $\Pr(\mathbf{x}|T)$ is equivalent to maximization of $\Pr(T|\mathbf{x})\Pr(\mathbf{x})$, we can simplify the problem further by maximizing the logarithm of $\Pr(T|\mathbf{x})\Pr(\mathbf{x})$. Thus, the problem is:

$$\hat{\mathbf{x}} = \arg \max_{\mathbf{x}} \ln(\Pr(T|\mathbf{x})\Pr(\mathbf{x})). \tag{5.2.3}$$

In tackling the problem, we first classify the given tests T into two subsets of passed tests and failed tests, respectively, represented by T_p and T_f. Since the test outcomes are assumed to be conditionally independent, we have $\Pr(T|\mathbf{x}) = \Pr(T_p|\mathbf{x})\Pr(T_f|\mathbf{x})$. Therefore, by converting the logarithm of the product to the sum of logarithms, we can write (5.2.3) as follows:

$$\hat{\mathbf{x}} = \arg \max_{\mathbf{x}} \{\ln(\Pr(T_f|\mathbf{x})) + \ln(\Pr(T_p|\mathbf{x})) + \ln(\Pr(\mathbf{x}))\}. \tag{5.2.4}$$

Since the potential failure sources are assumed to be independent, we have

$$\Pr(\mathbf{x}) = \prod_{i=1}^{m} \Pr(x_i). \tag{5.2.5}$$

Based on problem assumptions, we have $\Pr(x_i = 1) = p_{s_i}$; therefore $\Pr(x_i) = (p_{s_i})^{x_i}(1 - p_{s_i})^{1-x_i}$, which by defining $p_i = \frac{p_{s_i}}{1-p_{s_i}}$ can be simplified as:

$$\Pr(x_i) = (p_i)^{x_i}(1 - p_{s_i}). \tag{5.2.6}$$

Taking the logarithm of (5.2.5) and using (5.2.6), we have

$$\ln(\Pr(\mathbf{x})) = \sum_{i=1}^{m} \ln(p_i)x_i + \sum_{i=1}^{m} \ln(1 - p_{s_i}). \tag{5.2.7}$$

Note that $\sum_{i=1}^{m} \ln(1 - p_{s_i})$ is a known constant. The next term to calculate is $\ln(\Pr(T_p|\mathbf{x}))$. Since the test outcomes are assumed to be conditionally independent, we can write:

$$\Pr(T_p|\mathbf{x}) = \prod_{t_j \in T} \Pr(t_j = \text{pass}|\mathbf{x}) = \prod_{t_j \in T_p} \Pr(t_j|\mathbf{x}). \tag{5.2.8}$$

In order that test t_j has pass outcome conditioned on $\mathbf{x}$, it should pass conditioned on each component state. In other words,

$$\Pr(t_j = \text{pass}|\mathbf{x}) = \prod_{i=1}^{m} \Pr(t_j = \text{pass}|x_i). \tag{5.2.9}$$

From Fig. 5.1.3(b), we have

$$\Pr(t_j = \text{pass}|x_i) = \begin{cases} 1 - Pf_{ij} & x_i = 0 \\ 1 - Pd_{ij} & x_i = 1 \end{cases}. \tag{5.2.10}$$

Equation (5.2.10), can compactly be written as follows

$$\Pr\left(t_j = \text{pass}|x_i\right) = (1 - Pd_{ij})^{x_i}(1 - Pf_{ij})^{1-x_i} \tag{5.2.11}$$

By defining $\overline{Pd_{ij}} = 1 - Pd_{ij}$ and $\overline{Pf_{ij}} = 1 - Pf_{ij}$, we can write (5.2.11) as follows

$$\Pr\left(t_j = \text{pass}|x_i\right) = \overline{Pf_{ij}}\left(\overline{Pd_{ij}}/\overline{Pf_{ij}}\right)^{x_i}. \tag{5.2.12}$$

Inserting (5.2.12) into (5.2.9) and taking the logarithm, we have

$$\ln\left(\Pr\left(t_j = \text{pass}|\mathbf{x}\right)\right) = \ln\left(y_j\right) = h_j + \sum_{i=1}^{m} \beta_{ij} x_i, \tag{5.2.13}$$

where $\beta_{ij} = \ln\left(\frac{\overline{Pd_{ij}}}{\overline{Pf_{ij}}}\right)$, $h_j = \sum_{i=1}^{m} \ln\left(\overline{Pf_{ij}}\right)$, and the continuous variable y_j is defined as

$$y_j = \Pr\left(t_j = \text{pass}|\mathbf{x}\right). \tag{5.2.14}$$

Note that β_{ij} and h_j are known constants. By taking the logarithm of both sides of (5.2.8) and then using relation (5.2.13), we can write:

$$\ln\left(\Pr\left(T_p|\mathbf{x}\right)\right) = \sum_{t_j \in T_p} \ln\left(y_j\right) = \sum_{t_j \in T_p} h_j + \sum_{t_j \in T_p} \sum_{i=1}^{m} \beta_{ij} x_i. \tag{5.2.15}$$

Note that the summation $\sum_{t_j \in T_p} h_j$ is simply a constant. The last term to be characterized from (5.2.4) is $\ln\left(\Pr\left(T_f|\mathbf{x}\right)\right)$. Similarly to the passed tests, for failed tests we have $\Pr\left(T_f|\mathbf{x}\right) = \prod_{t_j \in T} \Pr\left(t_j = \text{fail}|\mathbf{x}\right) = \prod_{t_j \in T_f} \Pr\left(t_j|\mathbf{x}\right)$ and as $\Pr\left(t_j = \text{fail}|\mathbf{x}\right) =$

$1 - \Pr(t_j = \text{pass}|\mathbf{x}) = 1 - y_j$, we have the following relation:

$$\Pr(T_f|\mathbf{x}) = \prod_{t_j \in T_f} (1 - y_j), \tag{5.2.16}$$

where based on (5.2.13) and the definition of y_j, we have

$$\ln(y_j) = h_j + \sum_{i=1}^{m} \beta_{ij} x_i. \tag{5.2.17}$$

By taking the logarithm of (5.2.16), we have:

$$\ln(\Pr(T_f|\mathbf{x})) = \sum_{t_j \in T_f} \ln(1 - y_j). \tag{5.2.18}$$

Now inserting (5.2.7), (5.2.15), and (5.2.18) into (5.2.4), and discarding the constant terms of $\sum_{i=1}^{m} \ln(1 - p_{s_i})$ and $\sum_{t_j \in T_p} h_j$, the SMFD problem simplifies to:

$$\begin{aligned} &\hat{\mathbf{x}} = \arg \max_{\mathbf{x},\mathbf{y}} J(\mathbf{x}, \mathbf{y}), \\ &\text{subject to :} \\ &\ln(y_j) = h_j + \sum_{i=1}^{m} \beta_{ij} x_i \quad \forall t_j \in T_f. \end{aligned} \tag{5.2.19}$$

where $J(\mathbf{x}, \mathbf{y})$, the primal objective function, is as follows:

$$J(\mathbf{x}, \mathbf{y}) = \sum_{t_j \in T_f} \ln(1 - y_j) + \sum_{t_j \in T_p} \sum_{i=1}^{m} \beta_{ij} x_i + \sum_{i=1}^{m} \ln(p_i) x_i. \tag{5.2.20}$$

Before we proceed to solve this problem, let us consider the case where the

tests are perfect, i.e., $Pd_{ij} = 1$ and $Pf_{ij} = 0$, for components associated with tests.

Property 1: If tests are perfect, for any passed test t_j, i.e., $t_j \in T_p$, the set of all components that are associated with test t_j should be healthy.

Proof. Using the definition of perfect test, if a component c_i is faulty, i.e., $x_i = 1$, and if it is associated with test t_j, i.e., $Pd_{ij} = 1$, then test t_j should fail. In other words, $x_i = 1 \;\; \Rightarrow \;\; t_j = \text{fail}$, whose contrapositive is: $t_j = \text{pass} \;\; \Rightarrow \;\; x_i = 0$. Therefore, $x_i = 0 \;\; \forall t_j \in T_p \;\&\; Pd_{ij} > 0$; in other words, for any test t_j where $t_j \in T_p$, the set of all components that are associated with test t_j, i.e., $Pd_{ij} > 0$, should be healthy. □

Property 1 substantially reduces the cardinality of failure sources, S, by discarding the failure sources covered by passed tests. Let the reduced set of failure sources be denoted by S^-.

Property 2: If tests are perfect, for any failed test t_j, i.e., $t_j \in T_f$, among all components associated with the failed test, i.e. $Pd_{ij} > 0$, at least one should be faulty.

Proof. Since, for perfect tests, we have $Pf_{ij} = 0 \; \forall i, j$, $h_j = \sum_{i=1}^{m} \ln\left(\overline{Pf_{ij}}\right) = \sum_{i=1}^{m} \ln(1) = 0$, the constraints in (5.2.17) are reduced to $\ln(y_j) = \sum_{i=1}^{m} \beta_{ij} x_i \;\; \forall t_j \in T_f$. Suppose all components that are associated with the failed test t_j are healthy, that is $x_i = 0 \;\; \forall x_i, \, Pd_{ij} > 0$, then, $\ln(y_j) = 0$. Equivalently, $\ln(1 - y_j)$ in the objective function (5.2.20) will be unbounded. Therefore, for any $t_j \in T_f$, for all $Pd_{ij} > 0$ at least one of the x_i's should be 1. □

This condition can be compactly expressed as $\sum_{x_i \in S^-} Pd_{ij} x_i \geq 1 \;\; \forall t_j \in T_f$. Note that for any $t_j \in T_f$, and for any $Pd_{ij} > 0$, we have $\beta_{ij} = \ln\left(\frac{\overline{Pd_{ij}}}{\overline{Pf_{ij}}}\right) = \ln\left(\frac{1-1}{1-0}\right) =$

$-\infty$. Since at least one of the corresponding x_i's is 1, $\ln(y_j) = -\infty \ \forall t_j \in T_f$ or $y_j = 0 \ \forall t_j \in T_f$, hence $\sum_{t_j \in T_f} \ln(1 - y_j) = \sum_{t_j \in T_f} \ln(1) = 0$.

Therefore, the SMFD problem reduces to the following set covering problem:

$$\begin{aligned} &\max \sum_{i \in S^-} \ln(p_i) x_i, \\ &\text{such that} \\ &\sum_{i \in S^-} x_i P d_{ij} \geq 1, \quad \forall t_j \in T_f. \end{aligned} \tag{5.2.21}$$

Since the set covering problem is NP-hard, the general problem in (5.2.19) is NP-hard as well. We solve the problem in (5.2.19) using Lagrangian relaxation. Note that in (5.2.19) and in the following discussion, the tests are in general imperfect. By relaxing the constraints in (5.2.19), performing some simple manipulations, and defining $\alpha_i = \ln(p_i) + \sum_{t_j \in T_p} \beta_{ij}$, $c_i(\lambda) = \alpha_i - \sum_{t_j \in T_f} \lambda_j \beta_{ij}$, the relaxed objective function will be as follows:

$$L(\mathbf{x}, \mathbf{y}, \lambda) \ = \sum_{t_j \in T_f} \{\ln(1 - y_j) + \lambda_j \ln(y_j) - h_j \lambda_j\} + \sum_{i=1}^{m} c_i(\lambda) x_i. \tag{5.2.22}$$

The advantage of (5.2.22) is that the maximization with respect to $\mathbf{x}$ and $\mathbf{y}$ can be done separately. As $\lambda_j \geq 0$, by taking derivative with respect to y_j and equating to zero, we obtain $y_j^* = \frac{\lambda_j}{1+\lambda_j}$, where y_j^* denotes the optimal value of y_j. By inserting y_j^* into (5.2.22) and simplifying, we obtain:

$$L(\lambda, \mathbf{x}) = \sum_{t_j \in T_f} \{\lambda_j \ln(\lambda_j) - (1 + \lambda_j) \ln(1 + \lambda_j) - h_j \lambda_j\} + \sum_{i=1}^{m} c_i(\lambda) x_i. \tag{5.2.23}$$

In [167], the above problem is solved iteratively by initializing λ_j's to unity, obtaining the optimal solution $\mathbf{x}^*$ of (5.2.23) via a set covering algorithm and then updating λ_j's via a subgradient approach until a stopping condition is met. For details, the reader is referred to [167]. Here, we discuss a purely dual approach to the problem in (5.2.23). For any given value of λ, the first summation in (5.2.23) is just a constant and therefore can be discarded, and the maximization of the second summation completely depends on the sign of $c_i(\lambda)$ terms. For any component c_i, if $c_i(\lambda)$ is positive, then $x_i^* = 1$, and if it is negative, $x_i^* = 0$. Therefore:

$$x_i^*(\lambda) = u\left(c_i(\lambda)\right) = u\left(\alpha_i - \sum_{t_j \in T_f} \lambda_j \beta_{ij}\right). \tag{5.2.24}$$

where $u(.)$ is the unit step function. Hence, the SMFD problem in the dual form is as follows:

$$
\begin{aligned}
&Q(\lambda) = L(\lambda, x^*) = Q_1(\lambda) + Q_2(\lambda), \\
&Q_1(\lambda) = \sum_{t_j \in T_f} q_j(\lambda_j), \quad q_j(\lambda_j) = \lambda_j \ln(\lambda_j) - (1+\lambda_j)\ln(1+\lambda_j) - h_j\lambda_j, \\
&Q_2(\lambda) = \sum_{i=1}^{m} c_i(\lambda) u\left(c_i(\lambda)\right) = \sum_{i=1}^{m} \max\left(0, c_i(\lambda)\right).
\end{aligned} \tag{5.2.25}
$$

Note that $c_i(\lambda)$ is negative with a high magnitude, if

- Failure source s_i has a low *a priori* probability, i.e., p_{s_i} is close to zero.
- Passed tests have high detection probabilities as long as false alarm probabilities are reasonable (less than 0.25).
- Failed tests have low detection probabilities as long as false alarm probabilities are reasonable (less than 0.25).

Next we characterize some properties of the SMFD problem using the dual cost function.

Property 3: In a real-world system, any failure source which is not associated with any of the failed tests, is healthy based on maximum likelihood estimation.

Proof. Since in a real-world system the probability of a failure source being faulty, i.e. p_{s_i}, is small (for example around 0.01 to 0.2), $\ln(p_i) < 0$ and since $\beta_{ij} \leq 0 \ \forall i, j$, $\alpha_i = \ln(p_i) + \sum_{t_k \in T_p} \beta_{ik} < 0$. If a failure source x_i is not related to any of the failed tests ($t_j \in T_f$), it is equivalent to saying that it gives neither a false alarm nor a detection to test $t_j \in T_f$, that is, $Pf_{ij} = Pd_{ij} = 0$, therefore $\beta_{ij} = \ln\left(\overline{Pd_{ij}}/\overline{Pf_{ij}}\right) = \ln(1/1) = 0 \ \ \forall t_j \in T_f$. Evidently, $c_i(\lambda) = \alpha_i$, which is always negative. As a result, $x_i^* = u\left(c_i(\boldsymbol{\lambda}^*)\right) = u(\alpha_i) = 0$. □

Property 3 can be used to substantially reduce the size of the fault diagnosis problem. Let $N = \{1, 2, \cdots, m\}$ and remove any failure source which is not related to any of the failed tests. Let us call the remaining indices as $S' \subseteq N$. Consequently, $Q_2(\lambda)$ can be simplified as $\sum_{i \in S'} c_i(\lambda) u\left(c_i(\lambda)\right)$. Since $\alpha_i < 0 \ \forall i$ and $\beta_{ij} \leq 0 \ \forall i, j$, for a failure source to be inferred faulty, the norm $\|\lambda^*\|$ should be sufficiently large. As a result for a given λ^*, the more negative α_i is, the more likely component c_i is healthy. Since $\alpha_i = \ln(p_i) + \sum_{t_k \in T_p} \beta_{ik}$ if a component c_i is associated with some failed tests (that is, $i \in S'$) and if it is not associated with any passed tests (that is $\sum_{t_k \in T_p} \beta_{ik} = 0$) then $\alpha_i = \ln(p_i) < 0$. However, if the failure source is associated with some of the passed tests (that is $\sum_{t_k \in T_p} \beta_{ik}$) then $\alpha_i < \ln(p_i) < 0$; hence, in this case the probability of $x_i^* = 1$ reduces even further. In other words, the more passed tests a failure source s_i is associated with, the more negative α_i becomes and consequently, the less likely failure source s_i is in state 1.

Property 4: In a real-world system, for any $t_j \in T_f$, we have $\lambda_j^* \leq \lambda_j^{\max}$, where $\lambda_j^{\max} = \frac{e^{h_j}}{1 - e^{h_j}}$.

Proof. Note that $Q_1(\lambda)$ is composed of $|T_f|$ separate elements, each equal to $q_j(\lambda_j)$, and each $q_j(\lambda_j)$ is a convex function whose minimum value occurs at $\frac{e^{h_j}}{1-e^{h_j}}$. As $Q_2(\lambda)$ does not contribute a decrease in $Q(\lambda)$, increasing λ_j at most up to $\frac{e^{h_j}}{1-e^{h_j}}$ may help in decreasing $Q(\lambda)$; thus, $\lambda_j^{\max} = \frac{e^{h_j}}{1-e^{h_j}}$. □

Property 5: In a real-world system, for any $i \in S'$ if we have $\alpha_i < \sum_{t_j \in T_f} \frac{\beta_{ij} e^{h_j}}{1 - e^{h_j}}$, then $x_i^* = 0$.

Proof. Since $\lambda_j^* \leq \lambda_j^{\max}$ based on property 4, therefore if $\alpha_i < \sum_{t_j \in T_f} \beta_{ij} \lambda_j^{\max}$ or $\alpha_i < \sum_{t_j \in T_f} \frac{\beta_{ij} e^{h_j}}{1 - e^{h_j}}$, then $c_i(\lambda^*) \leq c_i(\lambda^{\max}) < 0$. Thus, $x_i^* = u\left(c_i(\lambda^*)\right) = 0$. □

Based on Property 5, we can exclude from S' any i such that $\alpha_i < \sum_{t_j \in T_f} \frac{\beta_{ij} e^{h_j}}{1-e^{h_j}}$, call the remaining indices S'' and search for failure sources among S''. Therefore, $Q_2(\lambda)$ can be simplified as $\sum_{i \in S''} c_i(\lambda) u\left(c_i(\lambda)\right)$.

In the remainder of this section, we consider a simple example to gain insights into the SMFD problem. Consider a system with three components and two tests, where test t_1 is affected by components c_1 and c_2; test t_2 is affected by components c_2 and c_3. The prior probabilities are $\mathbf{p_s} = [0.15, 0.10, 0.05]^T$, and the non-zero detection and false alarm probabilities are $Pd_{11} = 0.85$, $Pd_{21} = 0.90$, $Pd_{22} = 0.80$, $Pd_{32} = 0.95$, $Pf_{11} = 0.06$, $Pf_{21} = 0.03$, $Pf_{22} = 0.07$, $Pf_{32} = 0.08$.

In the sequel, we consider the individual terms in the dual function to gain insights into the nature of the dual function. First, consider the function $f_1 = \lambda_j \ln(\lambda_j)$, $\lambda_j > 0$. At $\lambda_j = 1$, $f_1 = 0$. For the extreme value of $\lambda_j \to 0^+$, we have $f_1 \to 0^-$ and for the other extreme value of $\lambda_j \to +\infty$, we have $f_1 \to +\infty$. Therefore, for $\lambda_j \in (0, 1)$, the convex function f_1 is negative (see Fig. 5.2.1(a)) with the minimum value of $f_1^* = -e^{-1}$ occurring at $\lambda_j^* = e^{-1}$, and for $\lambda_j \in [1, \infty)$, the function monotonically increases from zero to infinity (see Fig. 5.2.1(a)).

Next, we consider $f_2 = -(\lambda_j + 1) \ln(\lambda_j + 1)$, which is the negative and time-shifted version of f_1. Note that f_2 can be sketched by shifting graph of f_1 by one unit to the left and then flipping it around the x-axis; thus it is evident that for positive λ_j, the function f_2 is always negative (see Fig. 5.2.1(a) and 5.2.1(b)). Therefore, for $\lambda_j \in (0, 1)$ as both f_1 and f_2 are negative, the summation of these two functions, i.e. $f_3 = f_1 + f_2$, is also negative (see Fig. 5.2.1). For $\lambda_j \in [1, \infty)$, the magnitude of f_2 is always bigger than the magnitude of f_1 and as f_2 is always negative, therefore f_2 dominates f_1. Thus, f_3 is negative for all positive values of λ_j and it goes unboundedly

to $-\infty$ as $\lambda_j \to +\infty$. In fact, it can be shown that as $\lambda_j \to +\infty$, the function f_3 asymptotically approaches $f_3^{\text{asymptotic}} = -1 - \ln(\lambda_j + 1)$ (see Fig. 5.2.1(b)). Note that in the case of multiple faults, there exist multiple Lagrangian multipliers. First, we look into the $Q_1(\lambda)$ part of the dual function. For now, we consider $\sum_{t_j \in T_f} \{\lambda_j \ln(\lambda_j)\}$, which is actually $\sum_{t_j \in T_f} f_1(\lambda_j)$ and $\sum_{t_j \in T_f} \{\lambda_j \ln(\lambda_j) - (1+\lambda_j)\ln(1+\lambda_j)\}$, which is actually $\sum_{t_j \in T_f} f_3(\lambda_j)$. From the equations, it is clear that both of these functions are symmetric with respect to the Lagrange multipliers. Figures 5.2.1(c) and 5.2.1(d) show the plots of these functions in a two dimensional space (which corresponds to a two-failed-tests scenario). The plot of $\sum_{t_j \in T_f} f_1(\lambda_j)$ has a cup-shape surface which first heads down and reaches the minimum value of $-2e^{-1}$ at $\lambda^* = [e^{-1}, e^{-1}]^T$, and thereafter, it heads up and monotonically goes to infinity (see Fig. 5.2.1(c)).

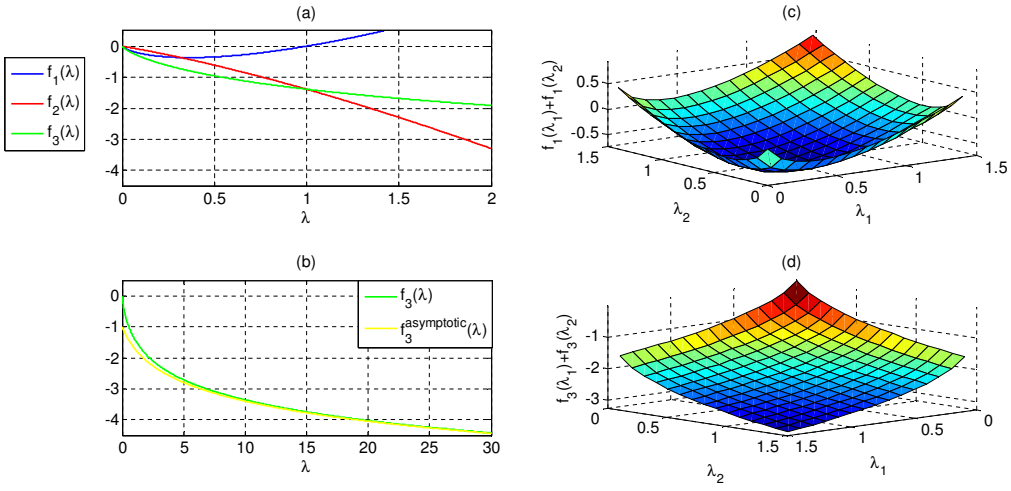

FIGURE 5.2.1: Some plots regarding the dual function

As we saw, $f_3(\lambda)$ is a monotonically decreasing function (Fig. 5.2.1(b)). Thus $\sum_{t_j \in T_f} f_3(\lambda_j)$ is also a monotonically decreasing function. The function for the case of the two-failed-tests scenario is shown in Fig. 5.2.1(d). For clarity of presentation, the direction of λ_1 and λ_2 in Fig. 5.2.1(d) is chosen to be opposite of those in Fig. 5.2.1(c).

Next, we consider the effects of $-h_j\lambda_j$ in the $Q_1(\lambda)$ part of the dual function. Note that $h_j = \sum_{i=1}^{m} \ln\left(\overline{Pf_{ij}}\right)$ is always negative, and in the above example $|h_2| > |h_1|$, because false alarm probabilities form components to test t_2 are greater than those to t_1 ($h_1 = -0.092$, $h_2 = -0.156$). The line $-h_j\lambda_j$ has always a positive slope, and it finally dominates f_3, because f_3 is asymptotic to the logarithmic function $-1-\ln(\lambda_j+1)$; thus $(f_3 - h_j\lambda_j) \to +\infty$ as $\lambda_j \to +\infty$. Figure 5.2.2(a) shows the plots of $f_3(\lambda), -h_1\lambda, -h_2\lambda, f_3(\lambda) - h_1\lambda$, and $f_3(\lambda) - h_2\lambda$. Figure 5.2.2(b) shows the $Q_1(\lambda)$ part of the dual cost function, which is asymmetric in the Lagrangian dimensions due to unequal h_j's, with a sharper slope in the direction of λ_2, because $|h_2| > |h_1|$. Intuitively, if the probabilities of the false alarms from different failure sources to the failed tests are high, the magnitudes of h_j's are high, which in turn results in an increase in the slope of $-h_j\lambda_j$ line and this results in λ_j^*'s to have low values. As the parameters α_i and β_{ij} are always negative, the low values of λ_j^*'s result in more arguments of $c_i(\lambda^*)$ to become negative; hence more components will likely be healthy.

Next, we consider the $Q_2(\lambda)$, which is $\sum_{i \in S''} (c_i(\lambda))\, u\,(c_i(\lambda))$. Note that for each failure source of this summation, $c_i(\lambda) = 0$ is a hyperplane in $|T_f|$ dimensions; the failure source makes no contribution to the dual cost function if $c_i(\lambda) \leq 0$ (because $u\,(c_i(\lambda)) = 0$), while it makes a positive linear contribution if $c_i(\lambda) > 0$; thus sharp corners are created in the dual cost function and make the dual cost function non-differentiable. In our example, as we have three components (failure sources), there

exist three hyperplanes (here they are just lines because $|T_f| = 2$), one for each component. Figure 5.2.2(c) shows these three lines and also the place where the minimum dual cost occurs. Figure 5.2.2(d) shows the dual cost function, which is obtained by adding the contributions of the non-differentiable function $Q_2(\lambda)$ to the differentiable function $Q_1(\lambda)$ shown in Fig. 5.2.2(b).

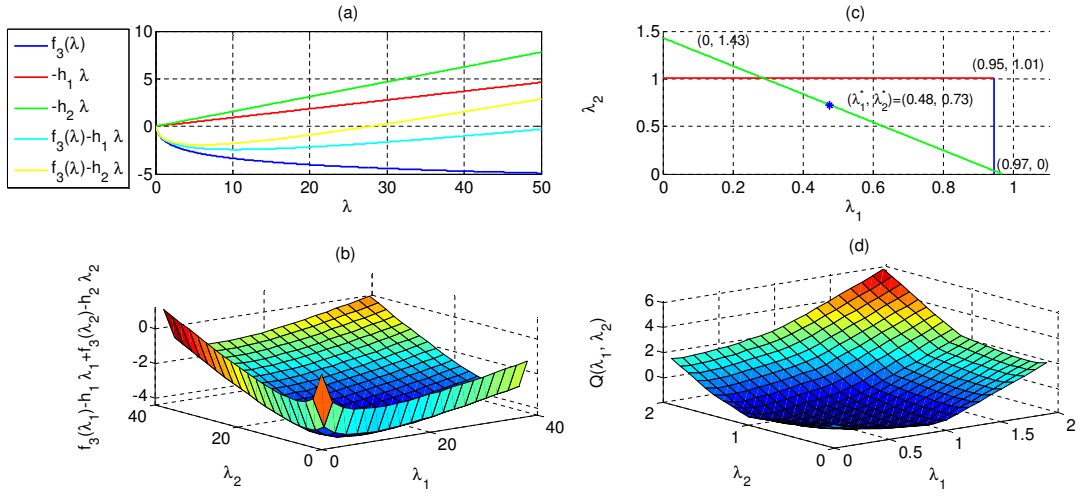

FIGURE 5.2.2: Dual cost function analysis

Note that, at the optimal point λ^*, if $c_i(\lambda^*)$ is negative, then $x_i^* = 0$ and if it is positive, then $x_i^* = 1$. However, for some components, we may have $c_i(\lambda^*) = 0$, and we cannot decisively assign a value to x_i^* because the contribution of $(c_i(\lambda^*))\, x_i^*$ to $Q(\lambda)$ is zero irrespective of x_i^* being one or zero. For these cases, we should either check the primal cost function or use the set-covering ideas. Note that for the following reasons, there are not many cases of this kind:

1. In practice, the number of failed tests $|T_f|$ is not large. As a result, the probability that $c_i(\lambda^*) = 0$ tends to be low.

2. In practice, the cause-effect relation of failure sources and tests is sparse (not all failure sources affect all tests). Therefore, not all hyperplanes have full dimension ($|T_f - 1|$).

3. As we saw in the illustrative example, the optimal point may occur on one hyperplane or few hyperplanes whose intersection is not a point but lower dimensioned hyperplanes.

4. The possibility of the optimal point being on a low-dimension hyperlane dramatically restricts the number of hyperplanes that include the optimal point. For example, given that the optimal point is on a hyperplane with dimension one (a line), then there exist only two generic possibilities: a) the only hyperplane that includes the optimal point, is that line, b) a line generally can intersect only a full-dimension (with dimension $|T_f| - 1$) hyperplane.

In our example, the optimal Lagrange multipliers (to three digits of accuracy) are $\lambda_1^* = 0.476$, $\lambda_2^* = 0.726$. The evaluation of $c_i(\lambda^*)$ for the three components are, respectively, -0.86, 7.2×10^{-5}, and -0.83. Evidently, $x_1^* = 0$ and $x_3^* = 0$. Since for x_2, the argument is very close to zero, we should either evaluate the primal cost for both candidates of $x_2 = 1$ and $x_2 = 0$, or use the set-covering idea for deciding on the assignment for x_2^*. Thus, we need to evaluate the primal cost for $x_1x_2x_3 = 000$ and $x_1x_2x_3 = 010$ and choose the one with the maximum value. The primal cost function for these two candidates are, respectively, -4.36 and -2.50, therefore $x_1x_2x_3 = 010$ is the most likely candidate. Also, since component c_2 covers both failed tests, it should

be faulty; thus we reach the same conclusion either way.

The non-differentiability of dual cost function demands the use of numerical optimization tools, such as subgradient algorithm, to find its optimal point. Recently, surrogate Lagrangian relaxation (SLR) method [37], which provides a general purpose rapidly converging algorithm for mixed-integer programming problems, has been proposed. The method, fundamentally, is based on two key ideas: a) decreasing the distance between Lagrange multipliers in consecutive iterations, by selecting appropriate step sizes, and b) preventing the algorithm from premature termination, by keeping step sizes sufficiently large. This algorithm has been used for solving the dual problem in (5.2.25).

5.3 Dynamic Multiple Fault Diagnosis

In this section, we discuss the dynamic multiple fault diagnosis (DMFD) problem. The difference between the DMFD and SMFD is that the states of the potential failure sources and the tests and their observations are functions of time. The additional assumptions for DMFD are the following:

- Time epochs of the system evolve in a discrete manner, from $k = 0$ to $k = K$.
- At any time epoch k, the state variable of component c_i (or failure source s_i) is $x_i(k)$ and the test outcomes are $t_j(k)$.
- Prior probability p_{s_i} is defined as $p_{s_i} = \Pr(x_i(0) = 1)$.
- The dynamics of states of components are assumed to be Markovian; in other words, there is a probability of fault appearance and probability of fault vanishing

(disappearance) as follows:

Probability of Fault Appearance: $Pa_i(k) = \Pr\left(x_i(k) = 1 | x_i(k-1) = 0\right)$.

Probability of Fault Vanishing: $Pv_i(k) = \Pr\left(x_i(k) = 0 | x_i(k-1) = 1\right)$.

Based on the above assumptions, the DMFD problem is defined as follows:

Dynamic Multiple Fault Diagnosis (DMFD) Problem : Given a set of test observations in $K+1$ epochs (namely, T^K) where $T^K \subseteq \mathbf{t}^K$, and given the initial states of components (namely, $\mathbf{x}(0)$),what is the most likely evolution of state sequence $\mathbf{x}^K$ of each potential failure source?

Note that the observed test outcome sequence T^K may not include all of the test outcomes. Formally, we can represent the problem as follows:

$$\hat{\mathbf{x}}^K = \arg \max_{\mathbf{x}^K} \Pr\left(\mathbf{x}^K | T^K, \mathbf{x}(0)\right). \tag{5.3.1}$$

As before, using Bayes' rule, the problem is equivalent to

$$\hat{\mathbf{x}}^K = \arg \max_{\mathbf{x}^K} \Pr\left(T^K | \mathbf{x}^K, \mathbf{x}(0)\right) \Pr\left(\mathbf{x}^K | \mathbf{x}(0)\right). \tag{5.3.2}$$

Using the assumptions that (i) passed and failed tests at a given epoch and the tests at different epochs are conditionally independent, (ii) invoking the Markovian nature of failure source state evolution, and (iii) using the fact that maximizing the posterior is equivalent to maximizing the log-posterior, we can simplify (5.3.2) as follows:

$$\hat{\mathbf{x}}^K = \arg \max_{\mathbf{x}^K} \sum_{k=1}^{K} f_k\left(\mathbf{x}(k), \mathbf{x}(k-1)\right), \tag{5.3.3}$$

where

$$f_k\left(\mathbf{x}(k),\, \mathbf{x}(k-1)\right) = \ln\left(\Pr\left(T_p(k)|\, \mathbf{x}(k)\right)\right) + \ln\left(\Pr\left(T_f(k)|\, \mathbf{x}(k)\right)\right) + \ln\left(\Pr\left(\mathbf{x}(k)|\mathbf{x}(k-1)\right)\right). \tag{5.3.4}$$

Now, let us find each of the three elements in the right hand side of (5.3.4). The first two terms are similar to the SMFD case. Therefore,

$$\ln\left(\Pr\left(T_p(k)|\mathbf{x}(k)\right)\right) = \ln(y_j(k)) = \gamma(k) + \sum_{t_j(k)\in T_p(k)} \sum_{i=1}^{m} \beta_{ij} x_i(k), \tag{5.3.5}$$

where

$$\gamma(k) = \sum_{t_j(k)\in T_p(k)} h_j, \tag{5.3.6}$$

$$\ln\left(\Pr\left(T_f(k)|\, \mathbf{x}(k)\right)\right) = \sum_{t_j(k)\in T_f(k)} \ln\left(1 - y_j(k)\right). \tag{5.3.7}$$

The third term in (5.3.4), using the Markov property, can be computed as follows:

$$\ln\left(\Pr\left(\mathbf{x}(k)|\mathbf{x}(k-1)\right)\right) = \sum_{i=1}^{m} \ln\left(\Pr\left(x_i(k)|x_i(k-1)\right)\right). \tag{5.3.8}$$

As each of $x_i(k-1)$ and $x_i(k)$ has two possible values, there exist four combinations for $\Pr\left(x_i(k)|x_i(k-1)\right)$. Therefore, $\Pr\left(x_i(k)|x_i(k-1)\right)$ can be compactly represented

as follows:

$$\begin{aligned}\Pr\left(x_i(k)|x_i(k-1)\right) = &\left(1-Pa_i(k)\right)^{(1-x_i(k-1))(1-x_i(k))}\left(Pa_i(k)\right)^{(1-x_i(k-1))x_i(k)}\\ &\left(1-Pv_i(k)\right)^{x_i(k-1)(1-x_i(k))}\left(Pv_i(k)\right)^{x_i(k-1)x_i(k)}.\end{aligned} \tag{5.3.9}$$

Inserting (5.3.9) into (5.3.8), and after some simplifications, we get the following formula:

$$\begin{aligned}\ln\left(\Pr\left(\mathbf{x}(k)|\mathbf{x}(k-1)\right)\right) &= \sum_{i=1}^{m}\mu_i(k)x_i(k)+\sum_{i=1}^{m}\sigma_i(k)x_i(k-1)\\ &\quad+\sum_{i=1}^{m}h_i(k)x_i(k)x_i(k-1)+g(k),\\ \mu_i(k) &= \ln\left(\tfrac{Pa_i(k)}{1-Pa_i(k)}\right), \qquad \sigma_i(k) = \ln\left(\tfrac{Pv_i(k)}{1-Pa_i(k)}\right),\\ h_i(k) &= \ln\left(\tfrac{(1-Pa_i(k))(1-Pv_i(k))}{Pa_i(k)Pv_i(k)}\right), \qquad g(k) = \sum_{i=1}^{m}\ln\left(1-Pa_i(k)\right).\end{aligned} \tag{5.3.10}$$

Thus, the DMFD problem is as follows:

$$\begin{aligned}\hat{X}^K &= \arg\max_{X^K}\sum_{k=1}^{K}f_k\left(\mathbf{x}(k),\,\mathbf{x}(k-1),\mathbf{y}(k)\right),\\ f_k\left(\mathbf{x}(k),\,\mathbf{x}(k-1)\right) &= \sum_{t_j(k)\in T_p(k)}\sum_{i=1}^{m}\beta_{ij}x_i(k)+\gamma(k)+\sum_{t_j(k)\in T_f(k)}\ln\left(1-y_j(k)\right)\\ &\quad+\sum_{i=1}^{m}\mu_i(k)x_i(k)+\sum_{i=1}^{m}\sigma_i(k)x_i(k-1)\\ &\quad+\sum_{i=1}^{m}\varphi_i(k)x_i(k)x_i(k-1)+g(k),\end{aligned} \tag{5.3.11}$$

subject to

$$\ln\left(y_j(k)\right) = h_j+\sum_{i=1}^{m}\ln(\beta_{ij})x_i(k). \tag{5.3.12}$$

The next step, as we did in SMFD, is to use Lagrangian relaxation. For this purpose, the constraint (5.3.12) is relaxed using Lagrange multipliers $\lambda_j(k)$. The resulting

Lagrangian function is:

$$L(\mathbf{x},\mathbf{y},\lambda)=\sum_{k=1}^{K} f_k\left(\mathbf{x}(k),\,\mathbf{x}(k-1),\mathbf{y}(k)\right) + \sum_{t_j(k)\in T_f(k)} \lambda_j(k)\left(\ln\left(y_j(k)\right)-h_j-\sum_{i=1}^{m}\ln(\beta_{ij})x_i(k)\right), \tag{5.3.13}$$

where $\lambda=\{\lambda_j(k)\geq 0, k\in\{1,...,K\}, t_j(k)\in T_f(k)\}$ is the set of Lagrange multipliers.

The dual of primal DMFD problem can be written as

$$\begin{aligned}&\min_{\lambda} Q(\lambda),\\ &\text{subject to: } \lambda=\{\lambda_j(k)\geq 0, k\in\{1,...,K\}, t_j(k)\in T_f(k)\},\end{aligned} \tag{5.3.14}$$

where the dual function is

$$Q(\lambda)=\max_{\mathbf{x},\mathbf{y}} L(\mathbf{x},\mathbf{y},\lambda). \tag{5.3.15}$$

Taking derivative of $L(\mathbf{x},\mathbf{y},\lambda)$ with respect to $y_j(k)$ and equating it to zero yields the optimal $y_j^*(k)$ as $\frac{\lambda_j(k)}{1+\lambda_j(k)}$. Inserting $\mathbf{y}^*(k)$ into (5.3.15), we get $Q(\mathbf{x},\lambda)=L(\mathbf{x},\mathbf{y}^*,\lambda)$, which, after some manipulation, yields:

$$Q(\lambda)=\max_{\mathbf{x}}\sum_{i=1}^{m} Q_i(x_i,\lambda), \tag{5.3.16}$$

where,

$$Q_i(x_i,\lambda)=\sum_{k=1}^{K}\left\{\xi_i\left(x_i(k),\,x_i(k-1),\lambda_j(k)\right)+\frac{1}{m}\omega_k(\lambda)\right\}, \tag{5.3.17}$$

$$\xi_i\left(x_i(k),\, x_i(k-1), \lambda_j(k)\right) = \left(\sum_{t_j(k)\in T_p(k)} \beta_{ij} + \mu_i(k) + \sum_{t_j(k)\in T_f(k)} \beta_{ij}\lambda_j(k)\right) x_i(k) + \sigma_i(k)x_i(k-1) + \varphi_i(k)x_i(k)x_i(k-1), \tag{5.3.18}$$

$$\omega_k(\lambda) = \gamma(k) + g(k) + \sum_{t_j(k)\in T_f(k)} \lambda_j(k)\ln\left(\lambda_j(k)\right) - \lambda_j(k)h_j - \sum_{t_j(k)\in T_f(k)} (1+\lambda_j(k))\ln\left(1+\lambda_j(k)\right). \tag{5.3.19}$$

Note that the original problem has been converted to a separable problem in (5.3.16), where the problem is one of solving m (one problem per component) much simpler problems. The dual problem can be solved in an iterative two-level strategy where separable problems of maximization $Q_i(x_i, \lambda)$ with respect to x_i is performed using the Viterbi algorithm (dynamic programming) and then the Lagrange multipliers are updated using surrogate subgradient methods. For more details about the implementation of the algorithm, extensions of this method to coupled, delayed failure source state propagation, and delayed observations, the reader is referred to [170], [103], [180], [104], and [204].

5.4 Fault Diagnosis in Active Probing (Sequential Fault Diagnosis) and Fault Diagnosis Applications

Passive monitoring, discussed as SMFD and DMFD in the previous sections, may still result in residual ambiguity as to sources of failure. The diagnosis from passive monitoring is followed by active probing to troubleshoot the source of failures. In this

section, we consider the active probing problem used for sequential fault diagnosis and point to the applications of fault diagnosis in a number of industrial contexts, including automotive, aerospace, and power systems. In the context of a static single fault diagnosis problem with perfect binary tests and failure sources with binary outcomes, the test sequencing problem can be conceptualized as a four-tuple $(S, \mathbf{p}, T, \mathbf{c})$, where S is the finite set of system states composed of the fault-free state s_0 and m failure sources denoted by $s_1, s_2, \ldots, s_m$. Associated with each failure source s_i and fault-free state s_0 is the *a priori* probability denoted by $\mathbf{p} = [p_0, p_1, \ldots, p_m]^T$. The vector $\mathbf{p}$ is therefore the *a priori* probability vector. The test set T is composed of n tests, i.e., $T = \{t_1, t_2, \ldots, t_n\}$ and the cost vector $\mathbf{c} = [c_1, c_2, \ldots, c_n]^T$ associates a cost to each test. The diagnostic dictionary (code book) matrix D has the dimension of $(m+1) \times n$ whose ij-th element is one if test t_j is able to detect the fault state of s_i (i.e., s_i is associated with t_j) and zero otherwise. The problem is to design a sequential testing algorithm that unambiguously identifies the fault states using the set of tests, while minimizing the expected test cost given by

$$J = \mathbf{p}^T A \mathbf{c} = \sum_{i=0}^{m} \sum_{j=1}^{n} a_{ij} p_i c_j, \tag{5.4.1}$$

where A is an $(m+1) \times n$ matrix whose ij-th element is one if test t_j is used in the path leading to the identification of failure source s_i and zero otherwise. The problem is a perfectly observed Markov decision problem (MDP), whose solution is a deterministic AND/OR binary decision tree. In this tree, each OR node is labeled by a subset of S, which is called the ambiguity subset (state in an MDP), and each AND node denotes a test at an OR node (control or action in an MDP), and divides its input ambiguity subset into two disjoint ambiguity subsets at the output. As shown in

[87], however, the construction of the optimal decision tree is NP-complete. Therefore, a way of tackling the problem is to use heuristic search strategies with tight bounds on the cost-to-go [55], [62], [138].

In [138], the test sequencing problem (TSP) is solved using an ordered, best-fit search on an AND/OR graph using different heuristic evaluation functions (HEF) based on Huffman coding and entropy. It is shown that among the HEFs used [138], a HEF based on Hufmann code length is the best choice for medium-sized problems ($m < 100$) and that a HEF based on entropy plus one is suitable for larger problems. Rollout strategies have been employed to extend the range of applicability to even larger problems [179]. Reference [139] generalizes the test sequencing problem (TSP) [138] to modular diagnosis, wherein testing stops when a faulty module is isolated. The dynamic programming recursion for this generalized TSP is derived in [139] and lower bounds on the optimal cost-to-go are derived based on information theory. The problem is generalized to include test setups, precedence constraints on tests, multiple test outcomes, multiple system modes, and hierarchical test sequencing in [154], [161], [36]. In [155], the TSP was extended to consider the following cases:

- Minimize the maximum test cost.
- TSP with an upper bound on expected test time.
- TSP that achieves the lowest average ambiguity group size subject to a constraint on the number of tests.
- TSP that achieves the lowest expected test storage cost.

Reference [156] extends the test sequencing problem to the case where the tests are imperfect. Optimal and near-optimal test sequence construction methods for

multiple fault diagnosis are discussed in [168]. The test sequencing problem becomes even more difficult in hybrid systems with multiple modes of operation. This is because, in a multimode system, the availability of tests depends on the mode of the system and even the same test may have different diagnostic capabilities in different modes. The multimode test sequencing problem is discussed in detail in [161]. TEAMS (Testability Engineering And Maintenance System) [137], [57] is a package designed for automatic test sequencing and testability analysis of complex modular systems for multi-mode systems with multi-valued failure source states and multi-valued test outcomes [3].

Before we close this section, we mention some of the real world applications of fault diagnosis. Two of the applications of passive monitoring appear in tools such as QMR-DT [169], [200] and ARES-I [3]. Some of the Aerospace applications of active probing include UH-60, SH-60B, and Sikorsky S92 helicopters (transmission system, engine subsystem, landing gear control unit) and a receiver synthesizer (e.g. JTIDS-RS). A few of these applications can be found in [179], [180]. Fault diagnosis in automotive systems (engine control systems, antilock breaking systems, electric power generation and storage systems) is discussed in [120], [46], [119], [105]. Model-based diagnosis of an automotive engine is discussed in [133]. In [18], the fault diagnosis technique is used for identifying and evaluating power quality problems. Ref. [45] discusses fault diagnosis in Heating, Ventilation and Air Conditioning (HVAC) systems. Application of hierarchical test sequencing in a lithographic machine can be found in [36]. TSP has been effectively used to troubleshoot problems in semiconductor fabrication facilities as well.

5.5 Relevant Work

In this section, we place passive monitoring and active probing discussed in the previous sections in the context of literature on fault detection and diagnosis (FDD). FDD methods have mainly evolved upon three major paradigms, viz., model-based, data-driven and knowledge-based approaches. The FDD model-based approaches require mathematical representation of the system, hence, they are effectively applicable when satisfactory physics-based models of the system and an adequate number of sensors for state observation are available. Most applications of model-based diagnosis are restricted to systems with a relatively small number of inputs, outputs, and states. The main advantage of a model-based approach is incorporating a physical understanding into the process monitoring scheme. However, it is difficult to apply the model-based approach to large-scale systems because it requires detailed analytical models of failures in order to be effective.

The FDD data-driven approaches are preferred when system models are not available, but instead system monitoring data is available. This situation arises frequently when subsystem vendors seek to protect their intellectual property by not providing internal system details to the system integrators. In these cases, experimental data from an operating system or simulated data from a black-box simulator will be the major source of system knowledge for FDD. Neural network and statistical classification methods are illustrative of data-driven techniques. Significant amount of data is needed from monitored variables under nominal and faulty scenarios for data-driven analysis.

The FDD knowledge-based approaches require qualitative models for process monitoring and troubleshooting. These approaches are especially well-suited for sys-

tems for which detailed mathematical models are not available. Most knowledge-based techniques are based on casual analysis, expert systems, and/or ad hoc rules. Because of the qualitative nature of these models, knowledge-based approaches have been applied to many complex systems. Graphical models such as Petri nets, multi-signal flow graphs and Bayesian networks are applied for diagnostic knowledge representation and inference in automotive systems. Bayesian Networks subsume the deterministic fault diagnosis models embodied in the Petri net and multi-signal models. Model based, data-driven and knowledge-based approaches provide the sand box that test designers can use to experiment with, and systematically select relevant models or combinations thereof to satisfy the requirements on diagnostic accuracy, computational speed, memory, on-line versus off-line diagnosis, and so on. Ironically, no single technique alone can serve as the diagnostic approach for complex systems. Thus, an integrated diagnostic process that naturally employs data-driven techniques, graph-based dependency models and mathematical/physical models is necessary for fault diagnosis, thereby enabling efficient maintenance of these systems.

The graphical methods we discussed in previous sections belong to knowledge-based methods using cause-effect relations between the failure sources and test outcomes using false-alarm and detection probabilities. When the false alarm probabilities of all tests are zero, the problem simplifies to the parsimonious covering theory [56], [158], [144], [145]. In [144], based on probabilistic causal methods, a competition-based connectionist method is proposed to overcome the combinatorial explosion of computing the posterior probability of all possible combinations of failure sources. This method, however, does not guarantee a global optimum and is computationally expensive, even for small problems (e.g., $m = 26$). Genetic algorithm-based methods for MFD are used in [127], [31]. These algorithms, however, converge extremely slowly

and have been applied to small-size problems (e.g., $m = 20, n = 20$). In [197], a symptom clustering method is used which exploits the weak causal intersections in partially decomposable diagnosis structures. This approach, however, does not scale to systems with large numbers of non-decomposable causes and symptoms. In [167], the MFD problem is formulated as one of maximizing the log of the posterior probability of the hypothesized faults and the resulting constrained optimization problem is solved using Lagrangian relaxation [27], [64] and a subgradient method [29], [30]. It is shown that when tests are perfect (no false alarms and no missed detections), the MFD is reduced to a set covering problem [167]. However, it is well-known that set covering problem (SCP) is NP-hard [72], and different algorithms have been proposed for SCP, including tree-search procedures [182], [26] , genetic algorithm [28] , and greedy heuristics [48].

The dynamic fault diagnosis problem is discussed in [172], [173], using linear difference equations relating HMM and neural network based pattern recognition. The drawback of this approach is that building a neural network for a large number of classes (here, faults) is difficult [131], [189]. Graph theory has been widely used in fault diagnosis and safety-critical systems can be modeled at an abstract level as directed graphs [157], [106], [99], [44]. In [52], [63], the multiple fault diagnosis algorithms are proposed, assuming that at most k components in the system are faulty (the system is k-diagnosable). In [53], [33], [19], probabilistic models are proposed for fault diagnosis in these contexts.

The fault diagnosis problem has also been extensively studied in the control and estimation literature. A classic survey on the traditional model-based fault detection techniques is by Willsky [194]. Here, a system is represented by two sets of

equations: system dynamics and sensor equations.

$$\mathbf{x}(k+1) = \Phi(k)\mathbf{x}(k) + B(k)\mathbf{u}(k) + \mathbf{w}(k), \tag{5.5.1}$$

$$\mathbf{z}(k) = H(k)\mathbf{x}(k) + J(k)\mathbf{u}(k) + \mathbf{v}(k), \tag{5.5.2}$$

where $\mathbf{x}$, $\mathbf{u}$, and $\mathbf{z}$ are, respectively, the state vector, input vector, and measurement vector, Φ, B, H, and J are matrices, $\mathbf{w}$ and $\mathbf{v}$ are zero-mean, independent, white Gaussian noise processes, defined by the following covariances [194]:

$$E\left\{\mathbf{w}(k)\mathbf{w}^T(j)\right\} = Q\delta(k,j), \qquad E\left\{\mathbf{v}(k)\mathbf{v}^T(j)\right\} = R\delta(k,j), \tag{5.5.3}$$

where $\delta(k,j)$ is the Kronecker delta function, which is "one" if $k = j$ and "zero" otherwise. Equations (5.5.1)-(5.5.2) represent the "normal operation" or "no failure" model of the system [194]. A failure is defined as an abrupt change in the behavior of the system which could be caused, for example, by a malfunction in actuators, plant, or sensors. The failure diagnosis problem here is comprised of three tasks: alarm, isolation, and estimation [194]. The alarm task is a binary decision of existence or nonexistence of failure in the system. The isolation task is determining the source of failure, and the estimation task is to evaluate the extent of failure; for example is it a complete failure such as a sensor burn-out or is it a partial failure such as a sensor bias? [194]. In recent terminology, however, "alarm" is often referred to as "detection", and "isolation with or without estimation" as "diagnosis". Among elementary algorithms for failure detection are the Shewhart control chart, geometric moving average (GMA), finite moving average (FMA), filtered derivative algorithm, and some more advanced

approaches such as cumulative sum (CUSUM)-type algorithms, Bayes-type algorithms, and generalized likelihood ratio (GLR) test [24]. The traditional approaches discussed in [194] include "failure-sensitive" filters [61], [176], [94], [95], [101], [25], [98], voting systems (for systems with high degree of redundancy in parallel hardware), multiple hypothesis filter-detectors [111], [16], [50], jump process techniques [35], [34], and innovation-based detection systems [123], [125], [166], [80], [149], [193].

The failure-sensitive filters are categorized into two groups: indirect and direct approaches. Indirect failure detection approaches, such as exponentially age-weighted filter [61], [176], limited memory filter [94], noise covariance increase [95], respond faster than a normal filter and one can make failure detection decision by abrupt changes in state estimates. Direct failure detection approaches, however, assign "failure states" to failure modes (e.g., bias onset in a sensor), and failure is detected once a failure state deviates notably from its nominal value [101]. This method provides failure alarm, isolation, and estimation, all at once, at the cost of dimensionality enlargement and also performance degradation during normal conditions [194]. A systematic direct approach, which is applicable to a wide variety of abrupt changes in linear time-invariant (LTI) systems, is discussed in [25], [98], where a filter, with the dynamical form of (5.5.4), is assigned to the LTI system of $\dot{\mathbf{x}}(t) = A\mathbf{x}(t) + B\mathbf{u}(t)$ with the measurement equation of $\mathbf{z}(t) = C\mathbf{x}(t)$.

$$\frac{d}{dt}\hat{\mathbf{x}}(t) = A\hat{\mathbf{x}}(t) + D\left(\mathbf{z}(t) - C\hat{\mathbf{x}}(t)\right) + B\mathbf{u}(t). \tag{5.5.4}$$

Here, the gain matrix D is designed in a manner to highlight the effects of certain failures in the residuals of $\mathbf{z}(t) - C\hat{\mathbf{x}}(t)$. In other words, D is chosen so that specific failure modes have distinct directions ("signatures") in the space of residuals

[194].

A geometrical formulation of the filter is presented in [121]. The method in [25], [98] was reformulated as an eigensystem assignment problem in [190], which greatly simplifies the design process. Multiple hypothesis filter-detectors are based on using a bank of filters based on different hypotheses for the system behavior; innovations from these hypothesized models are used to find the most likely model [194]. A simple innovation-based detection approach is the chi-squared test [123], [195]. The chi-squared test is an alarm method with a binary decision output and it is useful in detecting failure modes that have noticeable effects on innovations, but is not sensitive in detecting subtle failure modes [194]. The drawbacks of the simple chi-squared test was partly the motivation for developing the generalized likelihood ratio (GLR) test [193], [195]; a modified version of GLR test was proposed in [23] to overcome the two drawback of GLR, namely, the coupling effect between the window size and hypothesis testing threshold and the possibly high sensitivity to the hypothesis testing threshold [22]. Since both faults and model uncertainties affect the residuals, the task of a "robust" FDI system is to be sensitive to faults and insensitive to uncertainties [142]. The various aspects of robustness in fault diagnosis systems are discussed in [47], [142], [67].

Another line of attack for fault diagnosis is the knowledge-based approaches using artificial intelligence techniques, such as qualitative reasoning, fuzzy systems and neural networks [69], [129]. The QSIM algorithm is a purely qualitative algorithm that is used in the medical context [108], [109], [110]. An example of the use of qualitative reasoning in the automotive industry is [174]. Fault diagnosis using fuzzy and neuro-fuzzy methods are discussed in [58], [17], [112], [91], [141]. Both shallow knowledge and deep knowledge fuzzy models are used for fault diagnosis [58]. The

neural network is another fault diagnosis method, which acts as a mapping from observations of sensor outputs and the alarms (which themselves are the outputs of some fault detection systems) to the faults or the hypothesized failure modes. However, the use of neural networks as a fault diagnosis tool is viable only in the absence of an accurate system model and abundance of process history data [181].

Another work related to the diagnosis problem is discriminability, diagnosability and optimal sensor placement [178], [107]. Discriminability level of a system is the number of faults that can be discriminated given a set of sensors [178]. Diagnosabilty degree is how the discriminability level is related to the total anticipated faults in the system [178], and sensor placement deals with optimal placement of sensors to increase the diagnosability of the system.

Another direction in the literature is diagnosis approaches for discrete-even system (DES) [171], [163], [164], [96], which are based on the hypothesis that any executed faulty event in a DES is diagnosed within a bounded number of state-transitions/events [96].

For more information on fault diagnosis methods, the interested reader is referred to the following papers and books: [194], [47], [90], [126], [129], [22], [73], [65], [140], [66], [67], [93], [142], [70], [184], [185], [183], [13], [92], [203], [86], [54], [71], [163], [24], [74], [143], [95], [40].

5.6 Summary

In this chapter, we discussed the problem of fault diagnosis in complex systems using knowledge-based probabilistic graphical models in two different contexts: static and

dynamic. The fault diagnosis problem is represented using a tri-partite probabilistic graphical model. The first layer of this tri-partite graph is composed of components of the system, which are the potential sources of failures. The healthy or faulty condition of each component is represented by a binary state variable which is zero if the component is healthy and one otherwise. The second layer is composed of tests with binary outcomes (pass or fail) and the third layer is the noisy observations associated with the test outcomes. The cause-effect relations between the states of the components and the test outcomes can be compactly modeled in terms of detection and false alarm probabilities. When the probability of fault detection is one and the probability of false alarm is zero, the test is termed perfect; otherwise it is deemed imperfect. In the case of perfect tests, the static multiple fault diagnosis (SMFD) problem reduces to a set-covering problem, which itself is an NP-hard problem. We discussed the SMFD problem in its general form by maximizing the posterior probability of component states given the fail or pass outcomes of tests. Since the solution to this problem is known to be NP-hard, we used a Lagrangian (dual) relaxation technique to find near-optimal diagnostic solutions, which has the desirable property of providing a measure of sub-optimality in terms of the approximate duality gap. Indeed, the solution would be optimal if the approximate duality gap is zero. The static problem is discussed in detail and a pure dual cost function is derived. By presenting some graphical illustrations, we provided insights into the properties of the non-differentiable dual function.

We also discussed the multiple fault diagnosis in a dynamic context (DMFD), where it is assumed that the states of components evolve as independent Markov chains and that, at each time epoch, we have access to some of the test outcomes. Finally, we discussed the fault diagnosis problem in the context of active probing

(also termed sequential testing or troubleshooting), where information is sequentially acquired to isolate the faults in minimum time, cost or other economic factors, and we briefly mentioned some of the applications of fault diagnosis.

Chapter 6

Unification of Leaky Noisy OR and Logistic Regression Test Models

6.1 Introduction

In this chapter, we discuss two widely-used graphical test models for fault diagnosis, namely, Detection-False Alarm (DFA) and leaky noisy OR (LNOR) test models, and we prove that they are equivalent. Two realizations of logistic regression (LR) are also discussed and their similarities with DFA and LNOR test models are discussed. Then, we propose a unified test model that includes LNOR and LR test models, and define the resulting fault diagnosis problem as one of MAP inference in a bi-partite digraph. The MAP problem is solved using the Lagrangian relaxation method and a dual cost function is derived. Comparisons of the LNOR and LR test models are presented using a simple example.

This chapter is organized as follows. In section 6.2, we discuss two test

models based on probabilistic graphical models, viz., Detection-False Alarm (DFA) and leaky noisy OR (LNOR), that are used for fault diagnosis, and we prove that for each DFA test model, there exists a unique LNOR test model. Then, in section 6.3, we discuss logistic representation of test models for fault diagnosis and present the logistic combinatorial, restricted logistic, and logistic regression (LR) test models. We show that restricted and regression versions of logistic test models are equivalent in a way that is reminiscent of DFA and LNOR test models. In section 6.4, we present a unified test model that includes the LNOR and the LR test models as special cases. In section 6.5, we present the *maximum a posteriori* (MAP) inference problem for the unified test model, and derive its solution using the Lagrangian relaxation method, and then we derive the dual cost function for the MAP problem. In section 6.6, we present the simulation results, where we compare the performance of the LNOR and LR test models and also discuss the dual cost function of the MAP inference problem for the unified test model. Finally, in section 6.7, we summarize the chapter.

6.2 Equivalence of Detection-False Alarm (DFA) and Leaky Noisy OR (LNOR) Test Models

In this section, we show the equivalence of two widely-used graphical models in fault diagnosis. In the binary case, the probabilistic relation between a failure source and a test outcome can be represented in terms of detection and false alarm probabilities [167], [11]. The detection probability (Pd_{ij}) is the probability that test t_j has a *fail* outcome, given that the failure source x_i is in a *failure* state; mathematically,

$$Pd_{ij} = \Pr\{t_j = 1 | x_i = 1\}. \tag{6.2.1}$$

False alarm probability (Pf_{ij}) is the probability that test t_j has a *fail* outcome, given that the failure source x_i is in a *non-failure* state; mathematically,

$$Pf_{ij} = \Pr\{t_j = 1 | x_i = 0\}. \tag{6.2.2}$$

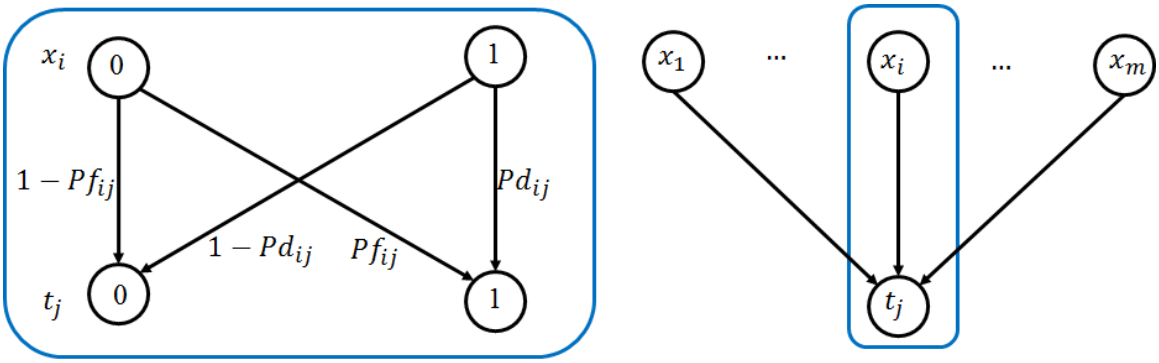

FIGURE 6.2.1: Detection-False Alarm (DFA) test model

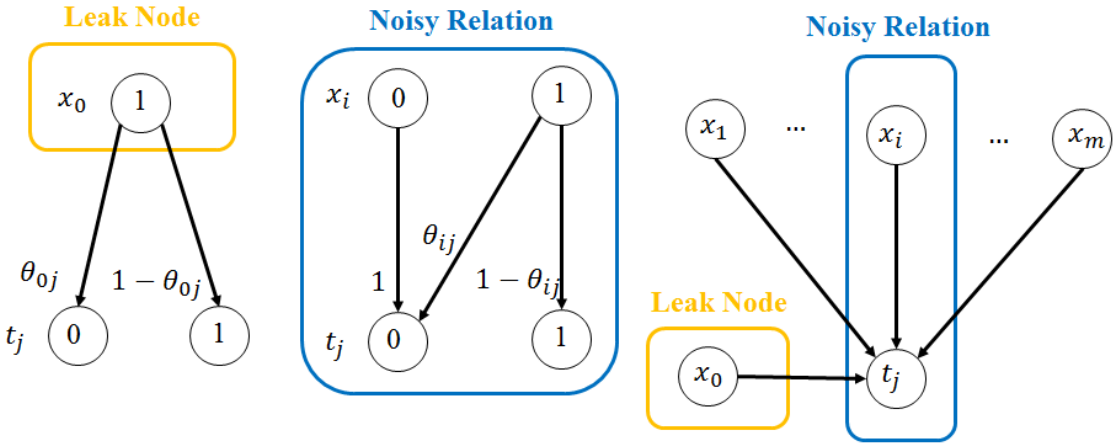

FIGURE 6.2.2: Leaky Noisy OR (LNOR) test model

Figure 6.2.1 shows the Detection-False Alarm (DFA) test model for a system

with m failure sources and one test t_j. In this model, in order for the test t_j to *pass*, all failure sources should be in *no-failure* state. Based on conditional independence assumption of test outcomes given the states of failure sources, we can write:

$$\Pr\{t_j = 0|\mathbf{x}\} = \prod_{i=1}^{m} (1 - Pf_{ij})^{1-x_i}(1 - Pd_{ij})^{x_i}. \tag{6.2.3}$$

Figure 6.2.2 shows the LNOR test model. In this model, for failure sources x_1 to x_m a value of zero leads to test outcome t_j of *pass*; that is,

$$\Pr\{t_j = 0|x_i = 0\} = 1. \tag{6.2.4}$$

However, when $x_i = 1$, the test outcome would be zero with probability θ_{ij} so that

$$\Pr\{t_j = 0|x_i = 1\} = \theta_{ij}. \tag{6.2.5}$$

Thus far, it is called noisy OR. In fact, if $\theta_{ij} = 0$ for $i = 1, 2, ..., m$, then it is a logical OR for which the output (t_j) is 1, if at least one of the inputs (x_i) is 1. However, when $\theta_{ij} \neq 0$, the output (t_j) could be 0 even when one or more inputs (x_i) are 1. Hence, it is called a noisy OR model. For this model, however, if all inputs are equal to 0, the output would be 0. To inject the possibility of the output being 1 even when all the inputs are 0, a leaky node is added (shown as x_0), whose value is always 1. The noisy OR test model with a leaky node is called a leaky noisy OR (LNOR) test model and the leaky node in fact represents the unmodeled dynamics in the system

[130]. For a LNOR test model

$$\Pr\{t_j = 0|\mathbf{x}\} = \theta_{0j} \prod_{i=1}^{m} \theta_{ij}^{x_i}. \tag{6.2.6}$$

Proposition 6.2.1. *For a DFA test model with m failure sources and n tests, and with detection probabilities Pd_{ij} and false alarm probabilities Pf_{ij}, there exist a unique LNOR test model with the following parameters:*

$$\theta_{0j} = \prod_{i=1}^{m} (1 - Pf_{ij}), \tag{6.2.7}$$

$$\theta_{ij} = \frac{1 - Pd_{ij}}{1 - Pf_{ij}}, \quad i = 1, 2, \ldots, m. \tag{6.2.8}$$

Proof. The following relation proves the existence of a unique LNOR test model for each DFA test model.

$$\begin{aligned} &\Pr\{t_j = 0|\mathbf{x}\} = \prod_{i=1}^{m} (1 - Pf_{ij})^{1-x_i} (1 - Pd_{ij})^{x_i} \\ &= \prod_{i=1}^{m} (1 - Pf_{ij}) \left(\tfrac{1-Pd_{ij}}{1-Pf_{ij}}\right)^{x_i} \\ &= \left(\prod_{i=1}^{m} (1 - Pf_{ij})\right) \prod_{i=1}^{m} \left(\tfrac{1-Pd_{ij}}{1-Pf_{ij}}\right)^{x_i} = \theta_{0j} \prod_{i=1}^{m} \theta_{ij}^{x_i}. \end{aligned} \tag{6.2.9}$$

□

Remark 6.2.2. The mapping from the LNOR parameters to the DFA parameters is not unique.

Note that false alarms occur for two reasons: errors in sensor measurements and processing, or unmodeled parameters. The DFA test model views the occurrence

of false alarms from a sensor measurement and processing error perspective, while the LNOR test model views them from an unmodeled dynamics perspective. However, in both models, once the parameters are learned from the fault injection-test output observations, both sensor measurement processing error and unmodeled parameter effects are reflected in the parameters of the respective models.

6.3 Logistic Representation of Test Models

The problem of fault diagnosis in the binary case can be formulated in the following form using the logistic function.

$$\Pr(t_j = 0|\mathbf{x}) = \frac{\exp\left(f_j(\mathbf{x})\right)}{1 + \exp\left(f_j(\mathbf{x})\right)}, \tag{6.3.1}$$

Since the sum of probabilities of all possible outcomes must add up to 1, it is required that:

$$\Pr(t_j = 1|\mathbf{x}) = \frac{1}{1 + \exp\left(f_j(\mathbf{x})\right)}, \tag{6.3.2}$$

By dividing equations (6.3.1) and (6.3.2), and taking the logarithm, we obtain:

$$f_j(\mathbf{x}) = \ln\left(\frac{\Pr(t_j = 0|\mathbf{x})}{\Pr(t_j = 1|\mathbf{x})}\right) \tag{6.3.3}$$

6.3.1 Logistic Combinatorial Test Models

The simplest way of modeling $f_j(\mathbf{x})$ is to assign a weight ω_j for each configuration of failure states as[1]:

$$\Pr(t_j = 0|\mathbf{x}) = \frac{\exp\left(\omega_j(x_m, \ldots, x_1)\right)}{1 + \exp\left(\omega_j(x_m, \ldots, x_1)\right)}, \tag{6.3.4}$$

That is

$$f_j(\mathbf{x}) = \omega_j(x_m, \ldots, x_1) \tag{6.3.5}$$

Another way of constructing a logistic combinatorial model is to use a polynomial of degree m for $f_j(\mathbf{x})$, as follows:

$$f_j(\mathbf{x}) = \sum_{k_m=0}^{1} \cdots \sum_{k_1=0}^{1} \nu_{k_m \cdots k_1 j} x_m^{k_m} \cdots x_1^{k_1} \tag{6.3.6}$$

6.3.2 Restricted Logistic Test Model

A method to reduce the number of parameters is to assign a weighting to each failure source and *restricting* its dependency on the state of that failure source; that is,

$$\Pr\left(t_j = 0|\mathbf{x}\right) = \frac{\exp\left(\sum_{i=1}^{m} \omega_{ij}(x_i)\right)}{1 + \exp\left(\sum_{i=1}^{m} \omega_{ij}(x_i)\right)} \tag{6.3.7}$$

As an example, consider two failure sources x_1, x_2 and one test t_j. The state

[1] Indexing in reverse order is intentional for decimal representation of the configuration states later.

configuration and the corresponding $f_j(\mathbf{x})$ are shown in Table 6.3.1.

TABLE 6.3.1: Input and $f_j(\mathbf{x})$ for two failure sources and a single output

x_2	x_1	$f_j(x_2, x_1)$
0	0	$\omega_{2j}(0) + \omega_{1j}(0)$
0	1	$\omega_{2j}(0) + \omega_{1j}(1)$
1	0	$\omega_{2j}(1) + \omega_{1j}(0)$
1	1	$\omega_{2j}(1) + \omega_{1j}(1)$

Note that the logistic test model of (6.3.7) is analogous to the DFA test model in the sense that in both models a zero state of any of the failure sources affects the probability of t_j, via Pf_{ij} in the DFA test model and via $\omega_{ij}(0)$ in the logistic test model.

6.3.3 Logistic Regression Test Model

Similar to the derivation of LNOR test model from a DFA test model, we can derive the LR test model from (6.3.7). We showed that the LNOR test model can aggregate the effect of the zero-states of the failure sources by introducing a leaky node and that the LNOR test model is equivalent to the DFA test model. This suggests us to consider the effect of $\omega_{ij}(0)$ for all $i = 1, 2, \ldots, m$ into one parameter. To illustrate this point, we consider a system with two failure sources x_1 and x_2 and one test t_j, all binary. For the new logistic test model we neglect the effect of each failure source when its state is zero. Therefore, corresponding to $\omega_{1j}(0)$ and $\omega_{2j}(0)$, we do not have any parameter in the new test model, but we assign a parameter ξ_{0j} that is applied in any combination of the failure states. Therefore, we have the following relations

between the ω parameters of model (6.3.7) and the ξ parameters of the new logistic model.

$$\begin{aligned}
\omega_{2j}(0) + \omega_{1j}(0) &= \xi_{0j} \\
\omega_{2j}(0) + \omega_{1j}(1) &= \xi_{0j} + \xi_{1j} \\
\omega_{2j}(1) + \omega_{1j}(0) &= \xi_{0j} + \xi_{2j} \\
\omega_{2j}(1) + \omega_{1j}(1) &= \xi_{0j} + \xi_{2j} + \xi_{1j}
\end{aligned} \tag{6.3.8}$$

Solving the above equations for the ξ parameters, yields:

$$\begin{aligned}
\xi_{0j} &= \omega_{2j}(0) + \omega_{1j}(0) \\
\xi_{1j} &= \omega_{1j}(1) - \omega_{1j}(0) \\
\xi_{2j} &= \omega_{2j}(1) - \omega_{2j}(0)
\end{aligned} \tag{6.3.9}$$

Remark 6.3.1. In general, for m failure sources $x_1, x_2, \ldots, x_m$ and one test t_j, all binary, we can write:

$$\begin{aligned}
\xi_{0j} &= \sum_{i=1}^{m} \omega_{ij}(0) \\
\xi_{ij} &= \omega_{ij}(1) - \omega_{ij}(0), \quad i = 1, \ldots, m
\end{aligned} \tag{6.3.10}$$

The general formulation for pass outcome would be:

$$\Pr\left(t_j = 0 | \mathbf{x}\right) = \frac{\exp\left(\xi_{0j} + \sum_{i=1}^{m} \xi_{ij} x_i\right)}{1 + \exp\left(\xi_{0j} + \sum_{i=1}^{m} \xi_{ij} x_i\right)} \tag{6.3.11}$$

Remark 6.3.2. Note that ξ_{0j} is the sum of all $\omega_{ij}(0)$'s, analogous to θ_{0j} being the multiplication of all $(1 - Pf_{ij})$'s. This is because $\omega_{ij}(0)$ is related to the logarithm of

the probability (see (6.3.3)). Also, note the similarity to a logistic neuron [177].

Remark 6.3.3. Note that ξ_{ij} is the difference between $\omega_{ij}(1)$ and $\omega_{ij}(0)$, analogous to θ_{ij} being the ratio of $(1 - Pd_{ij})$ and $(1 - Pf_{ij})$.

6.4 Unified Representation of Leaky Noisy OR and Logistic Regression Test Models

In this section, we present a unified representation for the LNOR and LR test models. Both models can be represented as follows:

$$z_j(\mathbf{x}) = \theta_{0j} \prod_{i=1}^{m} \theta_{ij}^{x_i}. \tag{6.4.1}$$

with

$$z_j(\mathbf{x}) = \Pr\left(t_j = 0|\mathbf{x}\right) \Big(1 - \Pr\left(t_j = 0|\mathbf{x}\right)\Big)^{-d} \tag{6.4.2}$$

where,

$$d = \begin{cases} 0 & \text{Leaky noisy OR} \\ \\ 1 & \text{Logistic regression} \end{cases} \tag{6.4.3}$$

Note that in the LNOR test model, $z_j(\mathbf{x})$ is the probability of test t_j being zero given $\mathbf{x}$, that is, $z_j(\mathbf{x}) = \Pr\left(t_j = 0|\mathbf{x}\right)$, and in the LR test model, $z_j(\mathbf{x})$ is the odds of test t_j being zero given $\mathbf{x}$, that is $z_j(\mathbf{x}) = \frac{\Pr(t_j=0|\mathbf{x})}{1-\Pr(t_j=0|\mathbf{x})}$. The parameters $\theta_{ij}, i = 0, 1 \ldots, m$ for the LNOR test model are as they were defined in section 2, and for the LR test

model, they are as follows:

$$\theta_{0j} = \exp\left(\xi_{0j}\right) \tag{6.4.4}$$

$$\theta_{ij} = \exp\left(\xi_{ij}\right), \quad i = 1, \ldots, m \tag{6.4.5}$$

The unified representation can be written as follows, as well:

$$\ln\left(z_j(\mathbf{x})\right) = \beta_{0j} + \sum_{i=1}^{m} \beta_{ij} x_i \tag{6.4.6}$$

where for the LNOR, $\beta_{ij} = \ln(\theta_{ij})$, and for the LR test model, $\beta_{0j} = \xi_{0j}$, and $\beta_{ij} = \xi_{ij}$ for $i = 1, \ldots, m$.

Remark 6.4.1. Note that (6.4.6) states that for the LNOR test model, the logarithm of probability of test t_j being zero is an affine linear function of the failure source states (linearity in probability) while, for the LR the logarithm of the odds of t_j being zero is an affine linear function of the failure source states (linearity in odds).

Remark 6.4.2. For the same observed data, the parameters of $\beta_{ij},\ i = 0, 1 \ldots, m$ for the LNOR test model are different from those of the LR test model.

Remark 6.4.3. For the LNOR test model, the parameters β_{ij} for $i = 0, 1, \ldots, m$ are non-positive, because θ_{ij} for $i = 0, 1, \ldots, m$, being probabilities, are restricted to be in the interval $[0, 1]$.

6.5 Maximum A Posteriori (MAP) Inference for the Unified Test Model

In this section, we present the fault diagnosis problem as the *maximum a posterior* (MAP) inference problem for the unified test model, and derive its solution using the Lagrangian relaxation method. Then, we derive the dual cost function for this MAP inference problem.

Let $\mathbf{x}$ denote the vector of all failure sources, and T be the test outcomes. Given T, the inference problem can be expressed as follows:

$$\hat{\mathbf{x}} = \arg \max_{\mathbf{x}} \Pr(\mathbf{x}|T). \tag{6.5.1}$$

The MAP estimation for the above inference problem can be written as follows:

$$\hat{\mathbf{x}} = \arg \max_{\mathbf{x}} \ln(\Pr(T|\mathbf{x}) \Pr(\mathbf{x})). \tag{6.5.2}$$

By categorizing the observed test outcomes T into two disjoint sets of passed test outcomes T_p, and failed test outcomes T_f, we can write the MAP problem (6.5.2), after taking logarithm, as follows:

$$\hat{\mathbf{x}} = \arg \max_{\mathbf{x}} \{\ln(\Pr(T_f|\mathbf{x})) + \ln(\Pr(T_p|\mathbf{x})) + \ln(\Pr(\mathbf{x}))\} \tag{6.5.3}$$

Assuming each failure source x_i has the prior probability p_{s_i} of being in the fail state,

we can write:

$$\Pr(x_i) = (1 - p_{s_i}) \left(\frac{p_{s_i}}{1 - p_{s_i}} \right)^{x_i} \tag{6.5.4}$$

Validity of (6.5.4) can be verified by checking $\Pr(x_i)$ for the two possible values $x_i = 0$ and $x_i = 1$. Using the conditional independence of failure sources, we can write:

$$\Pr(\mathbf{x}) = \prod_{i=1}^{m} \Pr(x_i) \tag{6.5.5}$$

Taking logarithm of (6.5.5), and using (6.5.4), we can write:

$$\ln(\Pr(\mathbf{x})) = \gamma_0 + \sum_{i=1}^{m} \gamma_i x_i \tag{6.5.6}$$

where,

$$\gamma_0 = \sum_{i=1}^{m} \ln(1 - p_{s_i}) \tag{6.5.7}$$

$$\gamma_i = \ln \left(\frac{p_{s_i}}{1 - p_{s_i}} \right) \tag{6.5.8}$$

To calculate $\ln(\Pr(T_p|\mathbf{x}))$, we start by equation (6.4.6) and (6.4.2), rewritten below for ready reference:

$$\ln(z_j(\mathbf{x})) = \beta_{0j} + \sum_{i=1}^{m} \beta_{ij} x_i \tag{6.5.9}$$

$$z_j(\mathbf{x}) = \Pr\left(t_j = 0|\mathbf{x}\right)\Big(1 - \Pr\left(t_j = 0|\mathbf{x}\right)\Big)^{-d} \tag{6.5.10}$$

Inserting (6.5.10) into (6.5.9) yields:

$$\begin{aligned}\ln\left(\Pr\left(t_j = 0|\mathbf{x}\right)\right) = &\Big(\beta_{0j} + \sum_{i=1}^{m}\beta_{ij}x_i\Big) \\ &+d\ln\Big(1 - \Pr\left(t_j = 0|\mathbf{x}\right)\Big)\end{aligned} \tag{6.5.11}$$

Since test outcomes are independent, we can write

$$\Pr\left(T_p|\mathbf{x}\right) = \prod_{t_j \in T_p}\Pr\left(t_j = 0|\mathbf{x}\right) \tag{6.5.12}$$

Taking logarithm of (6.5.12), and using (6.5.11), we have:

$$\ln\left(\Pr\left(T_p|\mathbf{x}\right)\right) = \beta_0 + \sum_{i=1}^{m}\beta_i x_i + d\sum_{t_j \in T_p}\ln\left(1 - y_j\right) \tag{6.5.13}$$

where,

$$\beta_i = \sum_{t_j \in T_p}\beta_{ij}, \quad i = 0, 1, \ldots, m \tag{6.5.14}$$

$$y_j = \Pr(t_j = 0|\mathbf{x}) \tag{6.5.15}$$

To calculate $\ln\left(\Pr\left(T_f|\mathbf{x}\right)\right)$, based on independence of test outcomes, we first note that:

$$\Pr\left(T_f|\mathbf{x}\right) = \prod_{t_j \in T_f}\Pr\left(t_j = 1|\mathbf{x}\right) \tag{6.5.16}$$

Taking logarithm of (6.5.16), and noting that probability of a fail outcome is the complement of probability of the pass outcome, we can write:

$$\ln\left(\Pr\left(T_f|\mathbf{x}\right)\right) = \sum_{t_j \in T_f} \ln\left(1 - y_j\right) \tag{6.5.17}$$

Using equations (6.5.6), (6.5.13), and (6.5.17), and by discarding constants γ_0 and β_0, we can write the MAP inference problem (6.5.3) as follows:

$$\hat{\mathbf{x}} = \arg\max_{\mathbf{x}} \sum_{t_j \in T_z} \ln\left(1 - y_j\right) + \sum_{i=1}^{m} \alpha_i x_i \tag{6.5.18}$$

subject to:

$$\ln\left(y_j\right) - d\ln\left(1 - y_j\right) = \beta_{0j} + \sum_{i=1}^{m} \beta_{ij} x_i,\ \forall t_j \in T_z \tag{6.5.19}$$

where,

$$T_z = \begin{cases} T_f & \text{Leaky noisy OR} \\ \\ T & \text{Logistic regression} \end{cases} \tag{6.5.20}$$

$$\alpha_i = \gamma_i + \beta_i, \quad i = 1, \ldots, m \tag{6.5.21}$$

Note that, for the LR test model, we have used the relation $T_p \cup T_f = T$.

The problem in (6.5.18), in the ideal case ($\theta_{0j} = 1, \theta_{ij} = 0, i = 1, \ldots, m$) for the LNOR test model, reduces to a set covering problem. Since the set covering

problem is NP-hard [128], the general problem in (6.5.18) is NP-hard as well.

Note that, while in the second summation in (6.5.18), the effect of the failure sources are decoupled, the first summation through y_j couples *all* the failure source states nonlinearly. To relax this coupling, we use Lagrange relaxation method. The relaxed version of optimization problem becomes:

$$\begin{aligned} L = & \sum_{t_j \in T_z} \ln(1-y_j) + \sum_{i=1}^{m} \alpha_i x_i \\ & + \sum_{t_j \in T_z} \lambda_j \left(\ln(y_j) - d \ln(1-y_j) - \beta_{0j} - \sum_{i=1}^{m} \beta_{ij} x_i \right) \end{aligned} \tag{6.5.22}$$

By taking the derivative of (6.5.22) with respect to y_j and equating it to zero, we get:

$$y_j = \frac{\lambda_j}{1 + (1-d)\lambda_j}, \quad \forall t_j \in T_z \tag{6.5.23}$$

Inserting (6.5.23) into (6.5.22) and rearranging it, we have:

$$L(\boldsymbol{\lambda}, \mathbf{x}) = \sum_{t_j \in T_z} L_{1j}(\lambda_j) + \sum_{i=1}^{m} c_i(\boldsymbol{\lambda}) x_i \tag{6.5.24}$$

where

$$c_i(\boldsymbol{\lambda}) = \alpha_i - \sum_{t_j \in T_z} \lambda_j \beta_{ij} \tag{6.5.25}$$

$$L_{1j}(\lambda_j) = \lambda_j \ln(\lambda_j) + (1 - d\lambda_j)\ln(1 - d\lambda_j) \\ - (1 + (1-d)\lambda_j)\ln(1 + (1-d)\lambda_j) - \beta_{0j}\lambda_j \tag{6.5.26}$$

Note that given $\boldsymbol{\lambda}$, the first summation in (6.5.24) is a constant and can be discarded, and the optimization in the second summation can be performed *for each failure source separately.* Therefore,

$$x_i^*(\boldsymbol{\lambda}) = u\left(c_i(\boldsymbol{\lambda})\right) = u\left(\alpha_i - \sum_{t_j \in T_z} \lambda_j \beta_{ij}\right) \tag{6.5.27}$$

where, $u(.)$ is the unit step function. The pure dual cost function then is as follows:

$$L(\boldsymbol{\lambda}) = \sum_{t_j \in T_z} L_{1j}(\lambda_j) + \sum_{i=1}^{m} L_{2i}(\boldsymbol{\lambda}) \tag{6.5.28}$$

where,

$$L_{2i}(\boldsymbol{\lambda}) = c_i(\boldsymbol{\lambda}) u\left(c_i(\boldsymbol{\lambda})\right) = \max\left(0,\ \ c_i(\boldsymbol{\lambda})\right) \tag{6.5.29}$$

and $L_{1j}(\lambda_j)$ is as in (6.5.26), which can also be written as in (6.5.30) and (6.5.31), respectively, for the LNOR and the LR test models.

$$L_{1j}(\lambda_j) = \lambda_j \ln(\lambda_j) - (1 + \lambda_j)\ln(1 + \lambda_j) - \beta_{0j}\lambda_j \\ \forall t_j \in T_f \tag{6.5.30}$$

$$L_{1j}(\lambda_j) = \lambda_j \ln(\lambda_j) + (1 - \lambda_j)\ln(1 - \lambda_j) - \beta_{0j}\lambda_j \\ = -H(\lambda_j) - \beta_{0j}\lambda_j, \quad \forall t_j \in T \tag{6.5.31}$$

where, $H(\lambda_j)$ is the binary entropy. Thus, one needs Lagrange multipliers for *failed tests only* in the case of LNOR, while the Lagrange multipliers are need for *all tests* in the case of LR.

6.6 Simulation Results

6.6.1 Comparison of the Leaky Noisy OR and Logistic Regression Test Models

In this section, using an example we compare the LNOR and LR test models. Consider a system with three failure sources x_1, x_2, and x_3 and two tests t_1 and t_2. Assume that test t_1 is affected by failures source x_1 and x_2, and test t_2 is affected by failure sources x_1 and x_3. From a DFA test modeling perspective, the non-zero detection and false alarm probabilities are $Pd_{11} = 0.85$, $Pd_{21} = 0.90$, $Pd_{22} = 0.80$, $Pd_{32} = 0.95$, $Pf_{11} = 0.06$, $Pf_{21} = 0.03$, $Pf_{22} = 0.07$, $Pf_{32} = 0.08$. Using (6.2.7) and (6.2.8), we can calculate the parameters of its equivalent LNOR test model. Then, we can find the least squares estimate of LR test model. Let $\Pr(t_j = 0|\mathbf{x})$for these models be, respectively, denoted as $\mathrm{P}_{\mathrm{OrgLNOR}}(\mathbf{x})$ and $\mathrm{P}_{\mathrm{OrgLR}}(\mathbf{x})$, where the subscripts "OrgLNOR" and "OrgLR" represent the best estimates for the *original* DFA test model, respectively for the LNOR and the LR test models. A wighted sum of the test probabilities of these two models is used as the training data.

$$\begin{aligned} &\Pr_{\mathrm{Obs}}(t_j = 0|\mathbf{x}) = \\ &w_{\mathrm{LNOR}}\mathrm{P}^j_{\mathrm{OrgLNOR}}(\mathbf{x}) + (1 - w_{\mathrm{LNOR}})\mathrm{P}^j_{\mathrm{OrgLR}}(\mathbf{x}) \end{aligned} \tag{6.6.1}$$

where $0 \leq w_{\text{LNOR}} \leq 1$ and $j = 1, 2$. When $w_{\text{LNOR}} = 1$, the observations have a linear structure in the logarithm of probability of test pass, and when $w_{\text{LNOR}} = 0$ they have a linear structure in the logarithm of the odds of test pass, and when $0 < w_{\text{LNOR}} < 1$ the observations have neither linear structure in the logarithm of probability of test pass, nor in the logarithm of the odds of test pass.

We use $\Pr_{\text{Obs}}(t_j = 0|\mathbf{x}), j = 1, 2$ to train the LNOR and the LR test models. The results for probability of test pass given for two models and the training data are shown in Fig. 6.6.1 and Fig. 6.6.2, respectively for t_1 and t_2. Note that as $\Pr(t_1 = 0|\mathbf{x} = 1x_2x_1) = \Pr(t_1 = 0|\mathbf{x} = 0x_2x_1)$ and $\Pr(t_2 = 0|\mathbf{x} = x_3x_21) = \Pr(t_2 = 0|\mathbf{x} = x_3x_20)$, for each test only the combinations of the two contributing failure sources are shown. It is seen that for the extreme values of $w_{\text{LNOR}} = 0$ and $w_{\text{LNOR}} = 1$, as we expect, respectively, the LR and the LNOR test models have perfect performance. As w_{LNOR} becomes less than 1 the performance of the LNOR test model degrades and, especially, for $\Pr(t_1 = 0|x_2x_1 = 00)$ and $\Pr(t_2 = 0|x_3x_2 = 00)$, the LNOR test model has poor performance for low values of w_{LNOR}. The LR test model, however, provides robust performance as the structure of observed data varies from a log-probability-linearity to log-odds-linearity.

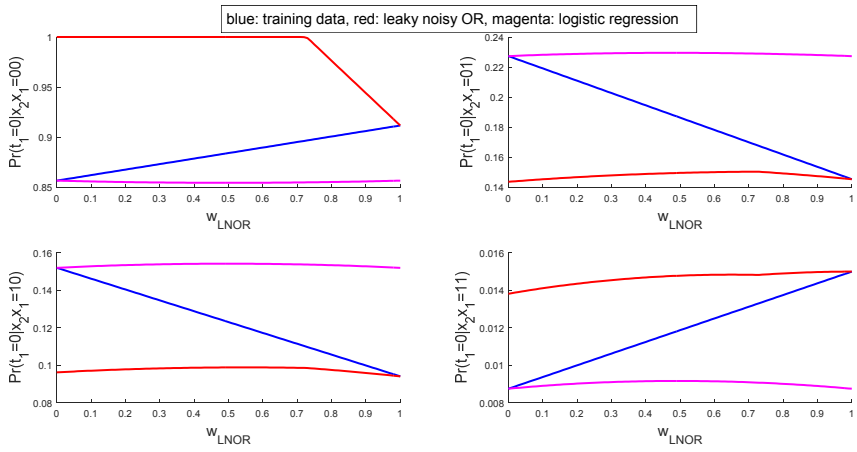

FIGURE 6.6.1: Comparison of probability of t_1 is passed given $\mathbf{x}$ for the LNOR and the LR test models

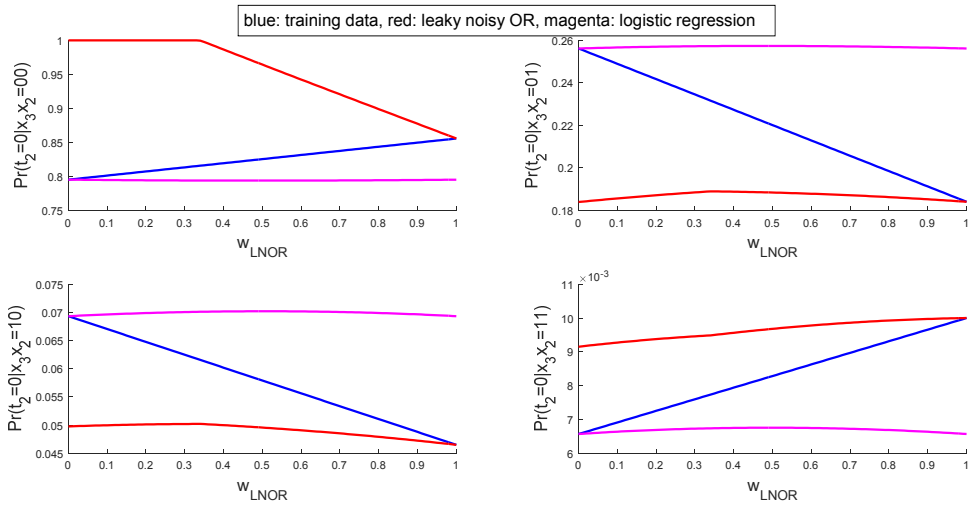

FIGURE 6.6.2: Comparison of probability of t_2 is passed given $\mathbf{x}$ for the LNOR and the LR test models

Figures 6.6.3 and 6.6.4 show $\Pr(t_2 t_1 = 11|\mathbf{x})\Pr(\mathbf{x})$ for all eight combinations

of failure sources, for $p_{s_1} = 0.15$, $p_{s_2} = 0.10$, and $p_{s_3} = 0.05$. It is seen that while the LR test model provides robust results, the LNOR test model results are off for low values of w_{LNOR} and for three combinations $x_3x_2x_1 = 000$, $x_3x_2x_1 = 001$, and $x_3x_2x_1 = 100$. The reason is that, for $x_3x_2x_1 = 100$, both inputs of test t_1 are zero, while for $x_3x_2x_1 = 001$, both inputs of test t_2 are zero, and for $x_3x_2x_1 = 000$, inputs of both tests t_1 and t_2 are zero, and we saw in Figures 6.6.1 and 6.6.2 that, the LNOR test model poorly estimates $\Pr(t_j|00)$ when w_{LNOR} is low. In reality, as the number of failure sources become large and since tests are connected to some of them only, in many combinations of the failure sources, one or more tests are subjected to all-zero inputs, and hence in those combinations, the error would be large when w_{LNOR} is low. Figure 6.6.4 also shows that when both tests fail for any value of w_{LNOR}, $\Pr(t_2t_1 = 11|\mathbf{x}\Pr(\mathbf{x}))$ has its highest value at $\mathbf{x} = 010$ and both test models provide the same inference.

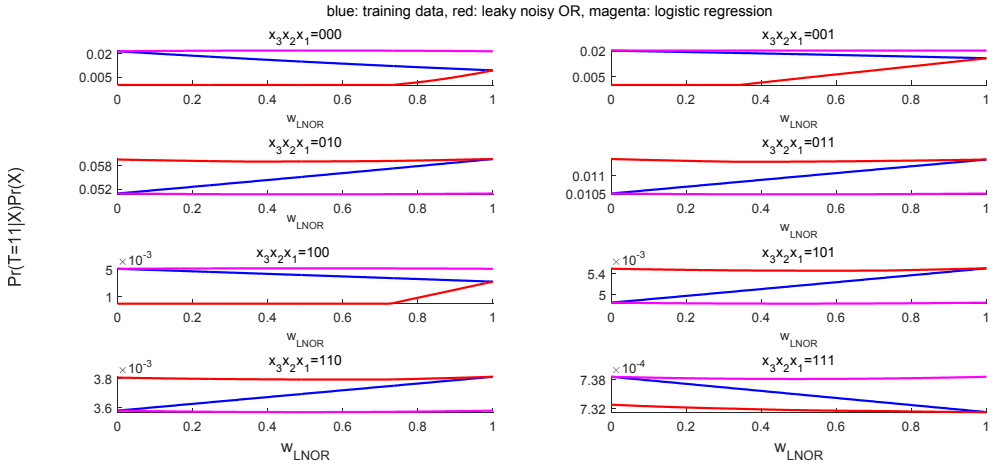

FIGURE 6.6.3: Comparison of $\Pr(T = 11|\mathbf{x})\Pr(\mathbf{x})$ for the LNOR and the LR test models

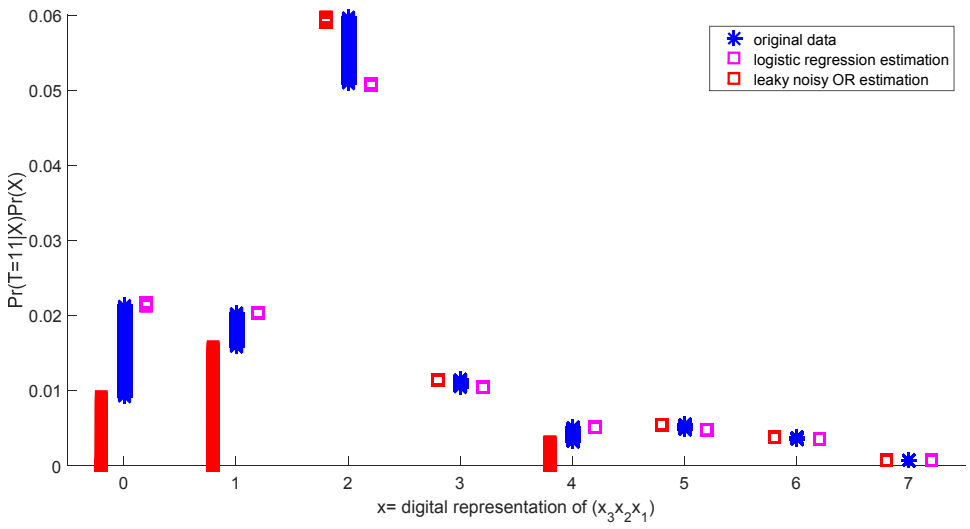

FIGURE 6.6.4: Comparison of $\Pr(T = 11|\mathbf{x})\Pr(\mathbf{x})$ for the LNOR and the LR test models

6.6.2 Dual Cost Function and the MAP Estimate

Figures 6.6.5 and 6.6.6, respectively, show the dual cost function, i.e., equation (6.5.28), for the LNOR and the LR test models. For the training of these models, we used $w_{\text{LNOR}} = 0.5$. Due to nonlinearities in (6.5.29), that is, $L_{2i}(\boldsymbol{\lambda}) = c_i(\boldsymbol{\lambda})u\left(c_i(\boldsymbol{\lambda})\right)$, both dual cost functions have sharp corners making them non-differentiable. Note that for the LR test model, based on (6.5.23), we have $\lambda_j = y_j$, and since y_j, as defined in (6.5.15), is a probability, the dual cost function for $\lambda_j > 1$ is undefined. However, for the LNOR test model based on (6.5.23), we have $\lambda_j = \frac{y_j}{1-y_j}$, which is an odds function, and thus can take any nonnegative value.

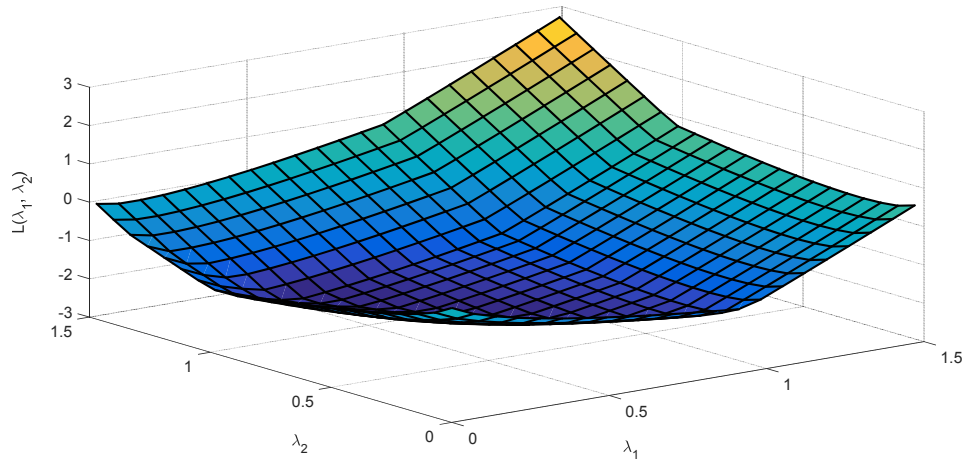

FIGURE 6.6.5: Dual cost function for the LNOR test model

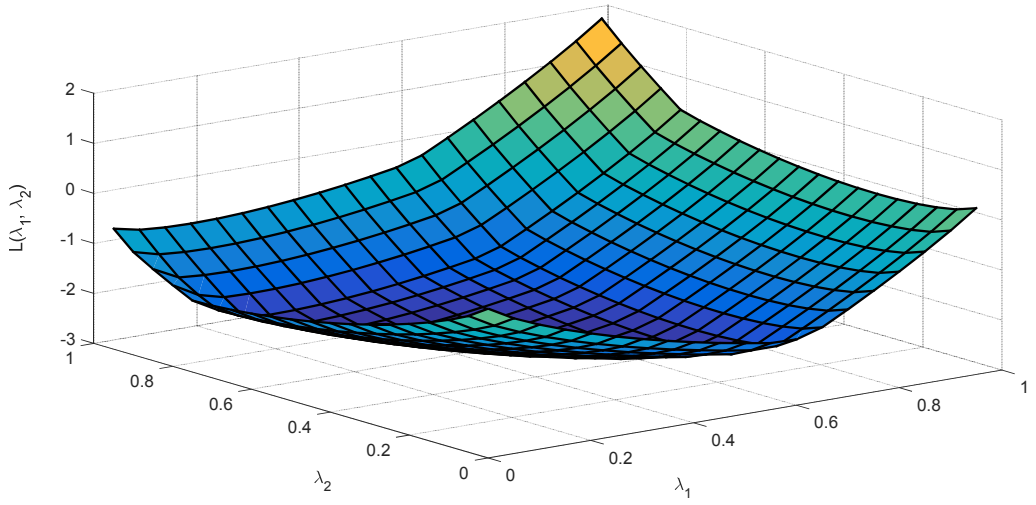

FIGURE 6.6.6: Dual cost function for the LR test model

The minimum value of the dual cost function for the LNOR test model occurs

at $(\lambda_1^*, \lambda_2^*) = (0.444, 0.716)$, and that for the LR occurs at $(\lambda_1^*, \lambda_2^*) = (0.343, 0.418)$. These result in $c_1(\boldsymbol{\lambda}^*)$ and $c_3(\boldsymbol{\lambda}^*)$ to be negative for both models, which means, based on (6.5.27), that $x_1^* = 0$ and $x_2^* = 0$. The value of $c_2(\boldsymbol{\lambda}^*)$ for both models is close to zero. When $c_i(\boldsymbol{\lambda}^*) = 0$, as the contribution of $c_i(\boldsymbol{\lambda^*})\, u\,(c_i(\boldsymbol{\lambda^*}))$ to the dual cost function is zero, irrespective of assigning 1 or 0 to $u\,(c_i(\boldsymbol{\lambda^*}))$, decision based on (6.5.27) will be ambiguous. Therefore, for $c_i(\boldsymbol{\lambda}^*)$ close to zero, we should either check the primal cost function or use the set-covering ideas. As discussed in [11] for the DFA test model, in practice, there are not many such cases. In the above example, comparing the primal cost function at $x_3x_2x_1 = 000$ and $x_3x_2x_1 = 010$ gives the optimal solution as $x_3^*x_2^*x_1^* = 010$.

6.7 Summary

In this chapter, we discussed two test models, viz., DFA (Detection False Alarm) and leaky noisy OR (LNOR); we proved the equivalence of these models in a proposition and showed that the parameters of the LNOR test model can be uniquely determined via the parameters of the DFA test model. The reverse mapping, however, is not unique. The false alarms are viewed as errors in sensor measurements and processing in the DFA test model, and as unmodeled parameters in the LNOR test model. However, in both models, once the parameters are obtained via the fault injection-test output observations, both sensor measurement errors and unmodeled parameter effects are reflected in the respective parameters of the models. In logistic test modeling, we presented two realization of the combinatorial case, one by assigning a weight to each failure combination and the other using a polynomial of degree m. Then, we showed a

more tractable model by restricting the weights on the possible states of each failure source, rather than the combination of all failure states. This resulted in a logistic test model similar to the DFA test model in structure, in the sense that a zero state of any of the failure sources affects the probability of test outcomes in both models. Using the same approach that we used for showing the equivalence of the DFA and the LNOR test models, we showed the equivalence of the restrictive test model and the logistic regression (LR) test model. Then, we devised a unified test model that encompasses both the LNOR and the LR test models. We presented the fault diagnosis problem as the *maximum a posterior* (MAP) inference problem for the unified test model, and derived its solution using a Lagrangian relaxation method. Finally, we derived the dual cost function for this unified MAP inference problem. Using an example, we discussed the dual cost function. Simulation results show that the LR test model is more robust with respect to the structure of the training data than the LNOR test model.

Chapter 7

Conclusion and Future Work

In this thesis, we discussed two problem, namely, (a) optimal battery charging and battery life management; (b) fault diagnosis using probabilistic graphical models. We applied optimization techniques to the first problem and Bayesian inference to the second one.

In optimal battery charging and battery life management, we tackled the problem in a two-time-scale algorithm which performs fast-charging at the lower-level (fast time-scale), while managing the battery life cycle at the higher-level (low time-scale). In the lower-level, we derived optimal charging algorithms for Li-ion batteries using equivalent electrical circuit models and quadratic optimization approaches. The objective function is considered as linear combination of time-to-charge (TTC), energy-loss (EL), temperature rise index (TRI), and any other arbitrary function of state-of-charge.

In the lower-level problem, with a simple battery model composed of an Open-Circuit Voltage (OCV) and a resistance, the optimal solution with objective

function being a weighted sum of TTC and EL, the solution (referred to as OtE (Optimal-time-Energy)) was proved to be the well-known CC-CV strategy with the value of current in the CC stage being a function of the ratio of weighting on TTC and EL and also the resistance of battery. To the best of our knowledge, this is the first time that it is proved that the well-known CC-CV charging profile is the optimal solution of a particular optimization problem, namely, the problem of minimizing the weighted sum of time-to-charge and energy loss.

In addition, we developed an analytical solution for the optimal TTC, EL and TRI, referred to as OtET, was developed. Due to similarity of the structure of the OtE and OtET solutions, a near-optimal version of OtET (referred to as NOtET). The NOtET is a CC-CV strategy with the value of current in the CC stage being a function of the ratio of weighting on TTC and EL, the resistance of the battery and the effective thermal resistance. Then, we presented a linear quadratic optimization approach and its solution to optimally charging a Li-ion battery in a general form. The optimal profile was derived based on a cost function, which is a weighted sum of time-to-charge (TTC), energy loss (EL), sum of the squares of the differences of the state-of-charge (SOC) from the final desired SOC, and temperature rise index (TRI). The presented solution strategy is generic and it is applicable to any equivalent electrical circuit model of a battery. A number of simulations were conducted to evaluate the effect of weighting parameters. Finally, extensive results on industrial batteries from LG, Nokia and Samsung were presented.

At the higher-level, we proposed a battery life management algorithm to determine the optimal values for the control parameters of charging process, namely, maximum allowable current and maximum allowable terminal voltage. As a precursor to the battery life management algorithm, we proposed two new battery capacity fade

models that are shown to be statistically superior to the bi-exponential capacity fade model.

The two models for estimating the normalized battery capacity are called the LAR-$\alpha\beta\gamma$ and the CVD. The former is a function of the number of cycles and the latter is a function of the number of cycles and two charge control parameters, viz., maximum terminal voltage of the battery ($v_{\max}$) and maximum charge current ($i_{\max}$). The accuracies of these models were explored by experimental data gathered from aging experiments performed on Samsung GS4 battery, and their dominance over the bi-exponential capacity model was demonstrated using the experimental data. The statistical dominance of LAR-$\alpha\beta\gamma$ over LS-BE was performed using Akaike Information Criterion (AIC). Using the CVD model, we also analyzed the effect of voltage and current on the capacity curves and we showed that $v_{\max}$, rather than $i_{\max}$, has a salient effect on capacity fade.

The proposed battery life management algorithm finds the best $v_{\max}$ and $i_{\max}$ to achieve a desired cycle life (for example, 500 cycles), while maintaining the normalized capacity above a desired threshold (for example, 80%) and attaining the fastest possible time-to-charge. The method was illustrated via numerical results. The optimal setpoint depends on the desired state of charge (denoted by s_{th}) for which we aim to attain the fastest charging time. It also depends on the resistance of the battery, i.e., R_0. Simulation results show that low fast-charging threshold on state of charge (s_{th}) and low battery resistance result in an optimal setpoint with the highest $i_{\max}$ among the set of feasible control settings, while increasing s_{th} and the battery resistance result in moving the optimal setpoint to lower values of $i_{\max}$ and higher values of $v_{\max}$. From the discussion of the different scenarios, we concluded that $i_{\max}$, rather than $v_{\max}$, has a salient effect on power fade, and $v_{\max}$, rather than $i_{\max}$, has a

salient effect on capacity fade.

In the second part of the thesis, for fault diagnosis, we considered the fault diagnosis problem using probabilistic graphical models. We discussed the Detection-False Alarm (DFA), the Leaky Noisy OR (LNOR), and the logistic regression (LR)-based test models. First, we proved the equivalence of DFA and LNOR test models. Then, we proposed a unified test model that includes both the LNOR and the LR test models as specific cases, and derived a Maximum *a posteriori* solution for the multiple fault diagnosis problem using the unified test model with the Lagrangian relaxation method, by deriving a dual cost function for the problem.

We discussed the problem of fault diagnosis in complex systems using knowledge-based probabilistic graphical models in two different contexts: static and dynamic. The fault diagnosis problem is represented using a tri-partite probabilistic graphical model. The first layer of this tri-partite graph is composed of components of the system, which are the potential sources of failures. The healthy or faulty condition of each component is represented by a binary state variable which is zero if the component is healthy and one otherwise. The second layer is composed of tests with binary outcomes (pass or fail) and the third layer is the noisy observations associated with the test outcomes. The cause-effect relations between the states of the components and the test outcomes can be compactly modeled in terms of detection and false alarm probabilities. When the probability of fault detection is one and the probability of false alarm is zero, the test is termed perfect; otherwise it is deemed imperfect. In the case of perfect tests, the static multiple fault diagnosis (SMFD) problem reduces to a set-covering problem, which itself is an NP-hard problem. We discussed the SMFD problem in its general form by maximizing the posterior probability of component states given the fail or pass outcomes of tests. Since the solution to this problem

is known to be NP-hard, we used a Lagrangian (dual) relaxation technique to find near-optimal diagnostic solutions, which has the desirable property of providing a measure of sub-optimality in terms of the approximate duality gap. Indeed, the solution would be optimal if the approximate duality gap is zero. The static problem is discussed in detail and a dual cost function is derived. By presenting some graphical illustrations, we provided insights into the properties of the non-differentiable dual function.

We also discussed the multiple fault diagnosis in a dynamic context (DMFD), where it is assumed that the states of components evolve as independent Markov chains and that, at each time epoch, we have access to some of the test outcomes. Finally, we discussed the fault diagnosis problem in the context of active probing (also termed sequential testing or troubleshooting), where information is sequentially acquired to isolate the faults in minimum time, cost or other economic factors, and we briefly mentioned some of the applications of fault diagnosis.

We discussed two widely-used graphical models, viz., DFA (Detection False Alarm) and leaky noisy OR (LNOR) test models; we proved the equivalence of these models in a proposition and showed that the parameters of the LNOR test model can be uniquely determined via the parameters of the DFA test model. The reverse mapping, however, is not unique. The false alarms are viewed as errors in sensor measurements and processing in the DFA test model, and as unmodeled parameters in the LNOR test model. However, in both models, once the parameters are obtained via the fault injection-test output observations, both sensor measurement errors and unmodeled parameter effects are reflected in the respective parameters of the models. In logistic test modeling, we presented two realization of the combinatorial case, one by assigning a weight to each failure combination and the other using a polynomial of

degree m. Then, we showed a more tractable model by restricting the weights on the possible states of each failure source, rather than the combination of all failure states. This resulted in a logistic test model similar to the DFA test model in structure, in the sense that a zero state of any of the failure sources affects the probability of test outcomes in both models. Using the same approach that we used for showing the equivalence of the DFA and the LNOR test models, we showed the equivalence of the restrictive model and the logistic regression (LR) test model. Then, we devised a unified test model that includes both the LNOR and the LR test models as special cases. We presented the fault diagnosis problem as the *maximum a posterior* (MAP) inference problem for the unified test model, and derived its solution using a Lagrangian relaxation method. Finally, we derived the dual cost function for this unified MAP inference problem. Using an example, we discussed the dual cost function. Simulation results show that the LR model is more robust with respect to the structure of the training data than the LNOR test model.

The primary contributions of this thesis are:

1. Derived a closed form solution for optimal battery charging profile to minimize a weighted sum of time-to-charge and energy loss;

2. Proved that for an OCV-Resistance battery model, CC-CV is the optimal solution with respect to an objective function, composed of linear combination of time-to-charge and energy-loss.

3. Derived a semi-closed form solution for optimal battery charging profile by adding the temperature rise index to the cost function;

4. Showed that the effect of temperature rise can be approximated as an equivalent

heating resistance;

5. Derived the optimal battery charging profile for general equivalent electrical circuit models as a linear quadratic - constant voltage (LQ-CV) strategy;

6. Derived two new battery capacity fade models that are shown to be statistically superior to the bi-exponential capacity fade model.

7. Developed an optimal charging parameter selection method for selecting the best settings for the control variables to achieve a desired "useful cycle life", while attaining the fastest possible time-to-charge;

8. Proved the equivalence of the Detection-False Alarm (DFA) and the Leaky Noisy OR (LNOR) test models;

9. Proposed a unified test model to include both the LNOR and the logistic regression (LR) test models;

10. Solved the maximum *a posteriori* (MAP) inference problem associated with the unified test model;

11. Derived a dual cost function for fault diagnosis problem both with the DFA test model and with the unified test model

12. Developed an algorithm for fault prognosis in systems using the unified test model.

The broader impacts of this thesis are:

1. Minimizing the life cycle cost of systems;

2. Enhancing the safety and reliability of systems;

3. Improving customer satisfaction through enhanced system availability;

4. The proposed research has utility in different application areas. Representative applications include automotive systems, aerospace systems, electrification of transportation, medical equipment, smart buildings/smart grid, and communication networks, to name a few.

The future work on battery management system, can include SOC-dependent and temperature-dependent parameters in the optimal battery charging. In the present work, the electrical parameters (e.g. R_0, R_1, C_1 and so on) are considered constant; while in reality they depend on SOC and temperature.

The above research can be done in two perspectives: (a) using look-up tables for parameters (b) using analytic equations for parameters. In the former, a general numerical method can be used. However, it has the benefit of being general for any chemistry, because for each chemistry, one can find the corresponding look-up tables using experiments, and then use the look-up-table-based devised method. Another advantage is that look-up tables are more favorable in industry; therefore, such a method would have more practical potential. The latter has the advantage of using analytic methods, but for any new chemistry one has to find proper analytical approximations for the parameters and different chemistries may result in different analytical formulae for electrical parameters and this makes the developed method limited. Also analytical formulae for parameters are less favorable than the look-up-table-based method in industry.

For modeling battery capacity, a future work could include not only modeling the cycle life of a battery but also modeling its calendar life, because battery capacity

not only fades with the way it is charged and discharged, but also it fades just by passing time even when the battery is not used. The study of interaction of battery cycle-life and battery calendar-life could be a challenging and interesting topic. For example, how a stand-still calendar-life affects the cycle-life behavior of a battery. This interaction, however, has practical importance in the initial calendar-life of a battery, because once a battery is bought by a user, normally it is not exposed to a long stand-still condition.

Another topic for future work could be analysis of efficiency degradation. While the efficiency of a battery mostly considered as one, in reality we get less energy from a battery during discharge process than what we put into the battery during a charge process. How this charging efficiency changes over the cycle life and calendar life of a battery could be interesting.

Another research track with practical outcomes is to use the typical usage of users that have somehow predictable loads, for example electric buses that undergo a typical load profile every week, and then using this data and the interaction of $v_{\max}$ and $i_{\max}$ with capacity fade and power fade, to determine a default charging profile that considers capacity fade and power fade in the whole useful life of the battery. This charging profile can be used as an initialization for a condition-based charging process.

Appendices

Appendix A

OCV and electrical parameters for commercial batteries

The following tables show the parameters of the equivalent electrical circuit model III for different commercial batteries.

TABLE A.0.1: Electrical parameters of model III for commercial batteries

Make	Model	Cell#	$R_0\,(\mathrm{m}\Omega)$	$R_1\,(\mathrm{m}\Omega)$	$C_1\,(\mathrm{F})$	α	$C_{\mathrm{batt}}\,(\mathrm{Ah})$
Samsung	EB575152	1	253	106	4581	0.997934	1.1875
Samsung	EB575152	2	209	94	5203	0.997962	1.2187
Samsung	EB575152	3	418	58	6222	0.99724	1.2001
Samsung	EB575152	4	200	142	3046	0.997689	1.485
Samsung	EB504465	1	259	106	4598	0.997941	1.5001
Samsung	EB504465	2	268	168	2493	0.997615	1.5293
Samsung	EB504465	3	272	211	1680	0.997186	1.5261
Samsung	EB504465	4	287	224	1589	0.997189	1.4831
Samsung	AB463651	1	451	198	2100	0.997597	0.9791
Samsung	AB463651	2	294	214	1950	0.997602	0.9614
Nokia	BP-4L	1	263	100	5031	0.998012	1.5514
Nokia	BP-4L	2	264	64	8141	0.99808	1.5691
Nokia	BP-4L	3	258	95	5306	0.998028	1.5612
Nokia	BP-4L	4	228	50	10502	0.998106	1.613
LG	LGIP	1	264	101	4747	0.997919	1.1141
LG	LGIP	2	297	76	6654	0.998021	1.1121

TABLE A.0.2: OCV parameters for commercial batteries

Make	Model	Cell #	OCV Parameters							
			K_0	K_1	K_2	K_3	K_4	K_5	K_6	K_7
Samsung	EB575152	1	-1.1288	65.0931	-10.5332	1.0640	-0.0457	-52.2654	94.1916	-0.7417
Samsung	EB575152	2	-1.6976	68.3306	-11.1189	1.1290	-0.0487	-54.5366	98.4237	-0.7882
Samsung	EB575152	3	-1.0802	68.3600	-11.0617	1.1178	-0.0480	-55.3010	99.0817	-0.8059
Samsung	EB575152	4	-4.3113	22.9007	-4.2921	0.4926	-0.0239	-10.3460	27.2251	0.0226
Samsung	EB504465	1	0.0218	54.9000	-9.1299	0.9668	-0.0442	-44.6447	78.9622	-0.7934
Samsung	EB504465	2	1.8254	61.0951	-10.0031	1.0470	-0.0474	-52.6013	89.7801	-1.0640
Samsung	EB504465	3	0.2510	55.0370	-9.1256	0.9634	-0.0439	-45.0942	79.3945	-0.8297
Samsung	EB504465	4	2.9648	59.8808	-9.7283	1.0127	-0.0457	-52.9562	88.9546	-1.1311
Samsung	AB463651	1	-1.6972	41.8528	-7.0700	0.7522	-0.0343	-30.6508	58.1983	-0.4098
Samsung	AB463651	2	-1.2526	40.3216	-6.7711	0.7166	-0.0326	-29.7536	56.3932	-0.3814
Nokia	BP-4L	1	-3.2203	51.9246	-8.8187	0.9344	-0.0421	-38.1050	71.7162	-0.5991
Nokia	BP-4L	2	-2.7537	52.9707	-8.9327	0.9407	-0.0422	-39.6357	73.7620	-0.6418
Nokia	BP-4L	3	-3.2084	51.8554	-8.7993	0.9314	-0.0419	-38.0572	71.6483	-0.5996
Nokia	BP-4L	4	-2.7140	60.3626	-10.0810	1.0533	-0.0469	-46.2542	85.0092	-0.7139
LG	LGIP	1	0.5267	61.5448	-10.1553	1.0682	-0.0485	-51.2165	89.3849	-0.9091
LG	LGIP	2	0.4788	59.0975	-9.7677	1.0290	-0.0468	-48.9737	85.6643	-0.8748

Appendix B

Temperature Modeling for OCV-Resistance Model

References [146] and [198] describe the temperature model as a linear system with two states. By discretizing the formulation in [146] and performing mathematical simplifications, we obtain a linear temperature model for a battery. The power generated at time t can be written as

$$Q_g(t) = R_0 i^2(t) \tag{B.0.1}$$

whose discrete form is

$$Q_g[k] = R_0 i^2[k] \tag{B.0.2}$$

The relation of core temperature and air temperature is as follows

$$Q_p(t) = \frac{T(t) - T_{air}(t)}{R_{eff}} \tag{B.0.3}$$

or in discrete form :

$$Q_p[k] = \frac{T[k] - T_{air}[k]}{R_{eff}} \tag{B.0.4}$$

where R_{eff} is the effective thermal resistance and is assumed constant [146] but varying in [198]. Also, from [146], we have

$$T_{air}(t) = T_{amb} + \frac{0.5Q_p(t)}{\dot{m}_{air}C_{air}} \tag{B.0.5}$$

or in discrete form:

$$T_{air}[k] = T_{amb} + \frac{0.5Q_p[k]}{\dot{m}_{air}C_{air}} \tag{B.0.6}$$

Based on [146], the formula for $T(t)$ is

$$T(t) = \int_0^t \frac{Q_g(t) - Q_p(t)}{m_{bat}C_{bat}}\, dt \tag{B.0.7}$$

We can write it in the discrete form as:

$$T[k+1] = T[k] + \frac{Q_g[k] - Q_p[k]}{m_{bat}C_{bat}}\Delta \tag{B.0.8}$$

We rewrite the required four formulas again:

$$T[k+1] = T[k] + \frac{Q_g[k] - Q_p[k]}{m_{bat}C_{bat}}\Delta \tag{B.0.9}$$

$$T_{air}[k+1] = T_{amb} + \frac{0.5Q_p[k]}{\dot{m}_{air}C_{air}} \tag{B.0.10}$$

$$Q_g[k] = R_0 i^2[k] \tag{B.0.11}$$

$$Q_p[k] = \frac{T[k] - T_{air}[k]}{R_{eff}} \tag{B.0.12}$$

Now we can write:

$$\begin{aligned} T[k+1] &= T[k] + \frac{Q_g[k] - Q_p[k]}{m_{bat}C_{bat}}\Delta \\ &= T[k] + \frac{\Delta}{m_{bat}C_{bat}}\left(R_0 i^2[k] - \frac{T[k] - T_{air}[k]}{R_{eff}}\right) \\ &= \left(1 - \frac{\Delta}{m_{bat}C_{bat}R_{eff}}\right)T[k] + \frac{\Delta}{m_{bat}C_{bat}R_{eff}}T_{air}[k] + \frac{R_0\Delta}{m_{bat}C_{bat}}i^2[k] \end{aligned} \tag{B.0.13}$$

or

$$T[k+1] = (1-a)T[k] + aT_{air}[k] + bi^2[k] \tag{B.0.14}$$

$$a = \frac{\Delta}{m_{bat} C_{bat} R_{eff}} \tag{B.0.15}$$

$$b = \frac{R_0 \Delta}{m_{bat} C_{bat}} \tag{B.0.16}$$

$$\begin{aligned} T_{air}[k+1] &= T_{amb} + \frac{0.5 Q_p[k]}{\dot{m}_{air} C_{air}} \\ &= T_{amb} + \frac{0.5}{\dot{m}_{air} C_{air}} \left(\frac{T[k] - T_{air}[k]}{R_{eff}} \right) \\ &= \frac{0.5}{\dot{m}_{air} C_{air} R_{eff}} T[k] - \frac{0.5}{\dot{m}_{air} C_{air} R_{eff}} T_{air}(k) + T_{amb} \end{aligned} \tag{B.0.17}$$

or

$$T_{air}[k+1] = cT[k] - cT_{air}[k] + T_{amb} \tag{B.0.18}$$

$$c = \frac{0.5}{\dot{m}_{air} C_{air} R_{eff}} \tag{B.0.19}$$

Putting (B.0.14) to (B.0.19) together, we can write the temperature equation in state variable form:

$$\begin{bmatrix} T[k+1] \\ T_{air}[k+1] \end{bmatrix} = \begin{bmatrix} 1-a & a \\ c & -c \end{bmatrix} \begin{bmatrix} T[k] \\ T_{air}[k] \end{bmatrix} + \begin{bmatrix} b \\ 0 \end{bmatrix} i^2[k] + \begin{bmatrix} 0 \\ 1 \end{bmatrix} T_{amb} \tag{B.0.20}$$

$$a = \frac{\Delta}{m_{bat} C_{air} R_{eff}} \tag{B.0.21}$$

$$b = \frac{R_0 \Delta}{m_{bat} C_{bat}} \tag{B.0.22}$$

$$c = \frac{0.5}{\dot{m}_{air} C_{air} R_{eff}} \tag{B.0.23}$$

The block diagram of the temperature model is shown in Fig. B.0.1

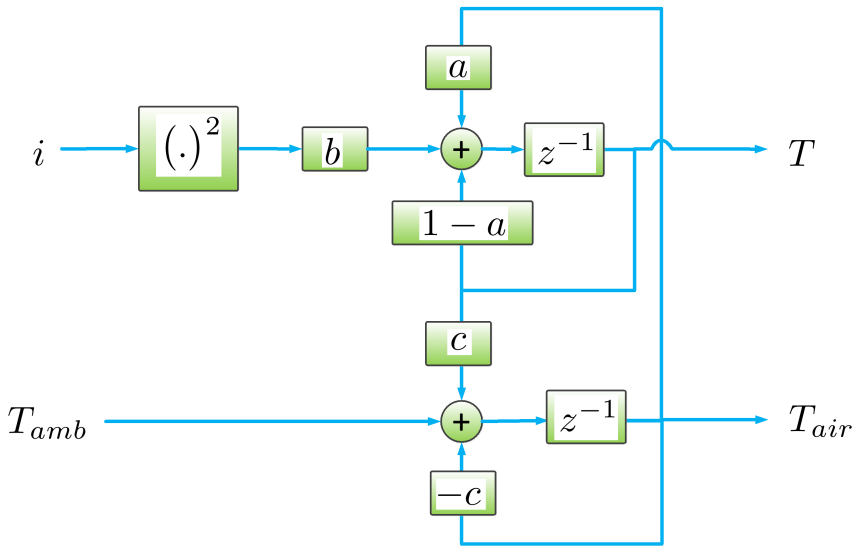

FIGURE B.0.1: Block diagram of temperature modeling

Note that $T_{air}[k]$ deviates from the ambient temperature by a negligible amount and therefore we can assume $T_{air}[k] \simeq T_{amb}$. Hence, we can write (B.0.14) as

$$\boxed{T[k+1] = T[k] - a(T[k] - T_{amb}) + bi^2[k]} \tag{B.0.24}$$

Actually, as we will see in the following, equation (B.0.24) is the linear part of heat transfer equation.

Now let us discuss temperature modeling based on heat transfer equation. References [134] and [147] discuss nonlinear temperature model based on the heat transfer equation. The heat transfer equation is as follows:

$$q - h_b A_{bs}(T_{bs} - T_f) - \sigma\varepsilon F_{bf}(T_{bs}^4 - T_f^4) = M_b C_b \frac{dT_{ba}}{dt} \tag{B.0.25}$$

Assuming $T_{bs} = T_{ba} = T_{core}, T_f = T_{amb}, q = R_0 i^2$ and discretizing (B.0.25) yields

$$T_{core}[k+1] = T_{core}[k] - a(T_{core}[k] - T_{amb}) - e(T_{core}^4[k] - T_{amb}^4) + bi^2[k] \tag{B.0.26}$$

$$a = \frac{h_b A_{bs} \Delta}{M_b C_b} \tag{B.0.27}$$

$$b = \frac{R_0 \Delta}{M_b C_b} \tag{B.0.28}$$

$$e = \frac{\sigma \varepsilon F_{bf} \Delta}{M_b C_b} \tag{B.0.29}$$

Note that based on [146], $R_{eff} = \frac{1}{h_b A_{bs}}$. Therefore, the a coefficient in (B.0.27) is exactly the same as the a coefficient in (B.0.21) in the previous section. Actually, if we neglect the $(T^4_{core}[k] - T^4_{amb})$ part of (B.0.26), then (B.0.26) reduces to (B.0.24) in the previous section. Also, note that in equation (B.0.26) the temperature should be in Kelvin. Let for notational simplicity from now on call T_{core} as T. Therefore, we write (B.0.26) as:

$$T[k+1] = T[k] - a(T[k] - T_{amb}) - e(T^4[k] - T^4_{amb}) + di^2[k] \tag{B.0.30}$$

Neglecting the nonlinear part of states, i.e., $(T^4[k] - T^4_{amb})$, we have

$$T[k+1] = T[k] - a(T[k] - T_{amb}) + bi^2[k] \tag{B.0.31}$$

Appendix C

Derivation of the LQ-CV algorithm

C.1 Concise Version

In this appendix, we derive the LQ-CV algorithm stated in section 2.4. This is a concise version of "Appendix C.2". We assumed that at time k_1, the SOC reaches the value v_c. Therefore, we can relax the constraint $s[k_1] = s_1$ with Lagrangian multiplier ν. Also, the dynamics of the system are relaxed by co-state vector $\underline{\lambda}$. Hence, the LQ problem is to minimize the following Lagrangian:

$$L[k] = J_{\mathrm{tEsT}} + \nu(s[k_1] - s_1) + \sum_{k=0}^{k_1-1} \left(\underline{\lambda}^T[k+1]\left(\Phi \underline{z}[k] + \Gamma i[k] - \underline{z}[k+1]\right)\right) \quad \text{(C.1.1)}$$

By inserting (2.4.33) into (C.1.1), and using Hamiltonian function $H[k]$ and

noting that $\begin{bmatrix} \nu & 0 \end{bmatrix} \underline{z}[k_1] = \nu(s[k_1] - s_{k_f})$, we can write $L[k]$ as in (C.1.2)

$$L[k] = \nu(s_{k_f} - s_1) + \left(\begin{bmatrix} \nu & 0 \end{bmatrix} - \underline{\lambda}^T[k_1] \right) \underline{z}[k_1] + H[0] + \sum_{k=1}^{k_1-1} \left(H[k] - \underline{\lambda}^T[k] \underline{z}[k] \right) \quad \text{(C.1.2)}$$

Applying the necessary conditions for optimality results in:

$$i[k] = -\frac{\Gamma^T}{2\Delta R_{0\text{eq}}[k]} \underline{\lambda}[k+1] \quad \text{(C.1.3)}$$

$$\underline{\lambda}[k] = \frac{\partial H[k]}{\partial \underline{z}[k]} = 2\tilde{Q}[k]\underline{z}[k] + \Phi^T \underline{\lambda}[k+1] \quad \text{(C.1.4)}$$

From (2.4.24), (C.1.3) and (C.1.4), we can write the dynamics of $\underline{z}[k]$ and $\underline{\lambda}[k]$ in the following forward/backward form:

$$\begin{bmatrix} \underline{z}[k+1] \\ \underline{\lambda}[k] \end{bmatrix} = \begin{bmatrix} \Phi & -\Psi[k] \\ 2\tilde{Q}[k] & \Phi^T \end{bmatrix} \begin{bmatrix} \underline{z}[k] \\ \underline{\lambda}[k+1] \end{bmatrix} \quad \text{(C.1.5)}$$

where

$$\Psi[k] = \frac{\Gamma\Gamma^T}{2\Delta R_{0\text{eq}}[k]} \quad \text{(C.1.6)}$$

In order to obtain the optimal current profile, we first consider the following evolutions:

$$\underline{\lambda}[k] = P[k]\underline{z}[k] + \underline{g}[k]\nu \quad \text{(C.1.7)}$$

$$s_1 = \underline{u}^T[k]\underline{z}[k] + \omega[k]\nu + d[k] \tag{C.1.8}$$

In order that the above equations hold at time k_1, we need to have: $P[k_1] = \mathbf{0}_{2\times 2}$, $\underline{g}[k_1] = \underline{u}[k_1] = \begin{bmatrix} 1 & 0 \end{bmatrix}^T$, $\omega[k_1] = 0$, and $d[k_1] = s_{k_f}$. Using (C.1.5) and (C.1.7), we can write:

$$\underline{\lambda}[k] = 2\tilde{Q}[k]\underline{z}[k] + \Phi^T \left(P[k+1]\underline{z}[k+1] + \underline{g}[k+1]\nu\right) \tag{C.1.9}$$

Using (C.1.5) and (C.1.7), we can derive $\underline{z}[k+1]$ in terms of $\underline{z}[k]$ and ν, which once inserted into (C.1.9) yields $\underline{\lambda}[k]$ as a function of $\underline{z}[k]$ and ν. Comparison of the so-obtained function for $\underline{\lambda}[k]$ to (C.1.7) and using Woodbury matrix identity [83] results in the following relations for the evolution of $P[k]$ and $\underline{g}[k]$:

$$P[k] = 2\tilde{Q}[k] + \Phi^T P[k+1]\left(I_3 + \Psi[k]P[k+1]\right)^{-1}\Phi \tag{C.1.10}$$

$$\underline{g}[k] = \Phi^T \left(I_3 + P[k+1]\Psi[k]\right)^{-1}\underline{g}[k+1] \tag{C.1.11}$$

Next, from (C.1.8) for times k and $k+1$, we can write two equivalent relations. Inserting in $\underline{z}[k+1]$, the function we obtained earlier in terms of $\underline{z}[k]$ and ν, and then equating the corresponding coefficients on both sides of the equations, we derive:

$$\underline{u}[k] = \Phi^T \left(I_3 + P[k+1]\Psi[k]\right)^{-1}\underline{u}[k+1] \tag{C.1.12}$$

$$\omega[k] = \omega[k+1] - \underline{g}^T[k+1]\left(I_3 + \Psi[k]P[k+1]\right)^{-1}\Psi[k]\underline{g}[k+1] \tag{C.1.13}$$

$$\underline{u}[k] = \underline{g}[k] \tag{C.1.14}$$

$$d[k] = s_{k_f} \quad \forall k \tag{C.1.15}$$

From (C.1.8), (C.1.14), and (C.1.15) we can write

$$\nu = \frac{s_1 - s_{k_f} - \underline{g}^T[k]\underline{z}[k]}{\omega[k]} \tag{C.1.16}$$

Knowing k_1, we can solve the dynamical equations for $P[k]$, $\underline{g}[k]$, and $\omega[k]$ in a backward fashion to calculate $\underline{g}[0]$ and $\omega[0]$. Inserting these values into (C.1.16) yields:

$$\nu = \frac{s_1 - s_{k_f} - \underline{g}^T[0]\underline{z}[0]}{\omega[0]} \tag{C.1.17}$$

Finally, we can write the optimal current as follows:

$$\boxed{i[k] = -\frac{\Gamma^T}{2\Delta R_{0\text{eq}}[k]} \left(P[k+1] \left((I_3 + \Psi[k]P[k+1])^{-1} \left(\Phi \underline{z}[k] - \Psi[k]\underline{g}[k+1]\nu \right) \right) + \underline{g}[k+1]\nu \right)} \tag{C.1.18}$$

Note that this is a state feedback (closed-loop) policy.

C.2 Detailed Version

In this appendix, we derive the LQ-CV algorithm stated in section 2.4. For a concise version of derivation, the reader may see "Appendix C.1". We assumed that at time

k_1, the SOC reaches the value v_c. Therefore, we can relax the constraint $s[k_1] = s_1$ with Lagrangian multiplier ν. Also, the dynamics of the system are relaxed by co-state vector $\underline{\lambda}$. Hence, the LQ problem is to minimize the following Lagrangian:

$$L[k] = J_{\text{tEsT}} + \nu(s[k_1] - s_1) + \sum_{k=0}^{k_1-1} \left(\underline{\lambda}^T[k+1]\left(\Phi\underline{z}[k] + \Gamma i[k] - \underline{z}[k+1]\right)\right) \quad \text{(C.2.1)}$$

Inserting (2.4.33) into (C.2.1), we have

$$\begin{aligned} L[k] &= \rho_t k_1 \Delta + \sum_{k=0}^{k_1-1} \left(\Delta R_{0\text{eq}}[k] i^2[k] + \underline{z}^T[k]\tilde{Q}[k]\underline{z}[k]\right) + \nu(s[k_1] - s_1) \\ &\quad + \sum_{k=0}^{k_1-1} \left(\underline{\lambda}^T[k+1]\left(\Phi\underline{z}[k] + \Gamma i[k] - \underline{z}[k+1]\right)\right) \\ &= \nu(s[k_1] - s_1) + \sum_{k=0}^{k_1-1} \left(\rho_t\Delta + \Delta R_{0\text{eq}}[k] i^2[k] + \underline{z}^T[k]\tilde{Q}[k]\underline{z}[k] + \underline{\lambda}^T[k+1]\left(\Phi\underline{z}[k] + \Gamma i[k]\right)\right) \\ &\quad - \sum_{k=0}^{k_1-1} \left(\underline{\lambda}^T[k]\underline{z}[k]\right) - \underline{\lambda}^T[k_1]\underline{z}[k_1] \end{aligned} \quad \text{(C.2.2)}$$

By defining Hamiltonian $H[k]$ as follows and noting that $\begin{bmatrix}\nu & 0\end{bmatrix}\underline{z}[k_1] = \nu(s[k_1] - s_{k_f})$, we can write $L[k]$ as in (C.2.4)

$$H[k] = \rho_t\Delta + \Delta R_{0\text{eq}}[k] i^2[k] + \underline{z}^T[k]\tilde{Q}[k]\underline{z}[k] + \underline{\lambda}^T[k+1]\left(\Phi\underline{z}[k] + \Gamma i[k]\right) \quad \text{(C.2.3)}$$

$$L[k] = \nu(s_{k_f} - s_1) + \left(\begin{bmatrix}\nu & 0\end{bmatrix} - \underline{\lambda}^T[k_1]\right)\underline{z}[k_1] + H[0] + \sum_{k=1}^{k_1-1}\left(H[k] - \underline{\lambda}^T[k]\underline{z}[k]\right) \quad \text{(C.2.4)}$$

The differential of $L[k]$ for small changes in current profile is

$$\delta L[k] = \left(\begin{bmatrix} \nu & 0 \end{bmatrix} - \underline{\lambda}^T[k_1] \right) \delta \underline{z}[k_1] + \frac{\partial H[0]}{\partial i[0]} \delta i[0] + \sum_{k=1}^{k_1-1} \left(\frac{\partial H[k]}{\partial i[k]} \delta i[k] + \left(\frac{\partial H[k]}{\partial \underline{z}[k]} - \underline{\lambda}[k] \right)^T \delta \underline{z}[k] \right) \quad \text{(C.2.5)}$$

Equating the coefficients of $\delta i[k]$ and $\delta \underline{z}[k]$ to zero, we obtain the necessary conditions for optimality as follows:

$$\frac{\partial H[k]}{\partial i[k]} = 0 \qquad k = 0, 1, ..., k_1 - 1 \quad \text{(C.2.6)}$$

$$\underline{\lambda}[k] = \frac{\partial H[k]}{\partial \underline{z}[k]} \qquad k = 1, ..., k_1 - 1 \quad \text{(C.2.7)}$$

$$\underline{\lambda}[k_1] = \begin{bmatrix} \nu & 0 \end{bmatrix}^T \quad \text{(C.2.8)}$$

From (C.2.3) and (C.2.6), we can write:

$$i[k] = -\frac{\Gamma^T}{2\Delta R_{0\text{eq}}[k]} \underline{\lambda}[k+1] \quad \text{(C.2.9)}$$

From (C.2.3) and (C.2.7), we can write:

$$\underline{\lambda}[k] = \frac{\partial H[k]}{\partial \underline{z}[k]} = 2\tilde{Q}[k]\underline{z}[k] + \Phi^T \underline{\lambda}[k+1] \quad \text{(C.2.10)}$$

From (2.4.24), (C.2.9) and (C.2.10), we can write the dynamics of $\underline{z}[k]$ and

$\underline{\lambda}[k]$ in the following forward/backward form:

$$\begin{bmatrix} \underline{z}[k+1] \\ \underline{\lambda}[k] \end{bmatrix} = \begin{bmatrix} \Phi & -\Psi[k] \\ 2\tilde{Q}[k] & \Phi^T \end{bmatrix} \begin{bmatrix} \underline{z}[k] \\ \underline{\lambda}[k+1] \end{bmatrix} \tag{C.2.11}$$

where

$$\Psi[k] = \frac{\Gamma\Gamma^T}{2\Delta R_{0\text{eq}}[k]} \tag{C.2.12}$$

In order to obtain the optimal current profile, we first consider the following evolutions:

$$\underline{\lambda}[k] = P[k]\underline{z}[k] + \underline{g}[k]\nu \tag{C.2.13}$$

$$s_1 = \underline{u}^T[k]\underline{z}[k] + \omega[k]\nu + d[k] \tag{C.2.14}$$

In order that the above equations hold at time k_1, we need to have:

$$P[k_1] = \begin{bmatrix} 0 & 0 \\ 0 & 0 \end{bmatrix} \tag{C.2.15}$$

$$\underline{g}[k_1] = \underline{u}[k_1] = \begin{bmatrix} 1 & 0 \end{bmatrix}^T \tag{C.2.16}$$

$$\omega[k_1] = 0 \tag{C.2.17}$$

$$d[k_1] = s_{k_f} \tag{C.2.18}$$

From (C.2.11), we have

$$\underline{\lambda}[k] = 2\tilde{Q}[k]\underline{z}[k] + \Phi^T\underline{\lambda}[k+1] \tag{C.2.19}$$

Inserting $\underline{\lambda}[k]$ from (C.2.13) into (C.2.19), we have

$$\underline{\lambda}[k] = 2\tilde{Q}[k]\underline{z}[k] + \Phi^T\left(P[k+1]\underline{z}[k+1] + \underline{g}[k+1]\nu\right) \tag{C.2.20}$$

From (C.2.11) we have

$$\underline{z}[k+1] = \Phi\underline{z}[k] - \Psi[k]\underline{\lambda}[k+1] \tag{C.2.21}$$

Inserting $\underline{\lambda}[k+1]$ from (C.2.13) into (C.2.21) we have

$$\underline{z}[k+1] = \Phi\underline{z}[k] - \Psi[k]\left(P[k+1]\underline{z}[k+1] + \underline{g}[k+1]\nu\right) \tag{C.2.22}$$

Rearranging (C.2.22), we can find $\underline{z}[k+1]$ in terms of $\underline{z}[k]$ and ν as follows

$$\underline{z}[k+1] = (I_3 + \Psi[k]P[k+1])^{-1}\left(\Phi\underline{z}[k] - \Psi[k]\underline{g}[k+1]\nu\right) \tag{C.2.23}$$

Inserting $\underline{z}[k+1]$ from (C.2.23) into (C.2.20), we have

$$\underline{\lambda}[k] = 2\tilde{Q}[k]\underline{z}[k] + \Phi^T\left(P[k+1]\left((I_3 + \Psi[k]P[k+1])^{-1}\left(\Phi\underline{z}[k] - \Psi[k]\underline{g}[k+1]\nu\right)\right) + \underline{g}[k+1]\nu\right) \tag{C.2.24}$$

Comparing (C.2.24) with (C.2.13), we can write the following relations for the evolution

of $P[k]$ and $\underline{g}[k]$:

$$P[k] = 2\tilde{Q}[k] + \Phi^T P[k+1]\left(I_3 + \Psi[k]P[k+1]\right)^{-1}\Phi \tag{C.2.25}$$

$$\underline{g}[k] \;\; = \Phi^T\left(I_3 - P[k+1]\left(I_3 + \Psi[k]P[k+1]\right)^{-1}\Psi[k]\right)\underline{g}[k+1] \tag{C.2.26}$$

Using Woodbury matrix identity, shown below, we can write (C.2.26) as (C.2.28)

$$(A + BCD)^{-1} = A^{-1} - A^{-1}B\left(C^{-1} + DA^{-1}B\right)DA^{-1} \tag{C.2.27}$$

$$\underline{g}[k] = \Phi^T\left(I_3 + P[k+1]\Psi[k]\right)^{-1}\underline{g}[k+1] \tag{C.2.28}$$

Next, from (C.2.14) for times k and $k+1$, we can write

$$\underline{u}^T[k]\underline{z}[k] + \omega[k]\nu + d[k] = \underline{u}^T[k+1]\underline{z}[k+1] + \omega[k+1]\nu + d[k+1] \tag{C.2.29}$$

Inserting $\underline{z}[k+1]$ from (C.2.23) into (C.2.29), we have

$$\begin{aligned}\underline{u}^T[k]\underline{z}[k] + \omega[k]\nu + d[k] &= \underline{u}^T[k+1]\left((I_3 + \Psi[k]P[k+1])^{-1}\left(\Phi\underline{z}[k] - \Psi[k]\underline{g}[k+1]\nu\right)\right) \\ &\quad + \omega[k+1]\nu + d[k+1] \\ &= \underline{u}^T[k+1]\left(I_3 + \Psi[k]P[k+1]\right)^{-1}\Phi\underline{z}[k] \\ &\quad + \left(\omega[k+1] - \underline{u}^T[k+1]\left(I_3 + \Psi[k]P[k+1]\right)^{-1}\Psi[k]\underline{g}[k+1]\right)\nu \\ &\quad + d[k+1]\end{aligned} \tag{C.2.30}$$

By equating the coefficients of $\underline{z}[k]$ at both sides of (C.2.30), we have

$$\underline{u}[k] = \Phi^T\left(I_3 + P[k+1]\Psi[k]\right)^{-1}\underline{u}[k+1] \tag{C.2.31}$$

Comparing (C.2.31) with (C.2.28) and noting that $\underline{u}[k_1] = \underline{g}[k_1]$, we can see that

$$\underline{u}[k] = \underline{g}[k] \tag{C.2.32}$$

By equating the coefficients of ν on both sides of (C.2.30), we have

$$\omega[k] = \omega[k+1] - \underline{g}^T[k+1]\left(I_3 + \Psi[k]P[k+1]\right)^{-1}\Psi[k]\underline{g}[k+1] \tag{C.2.33}$$

Finally, it is easy to conclude

$$d[k] = s_{k_f} \quad \forall k \tag{C.2.34}$$

From (C.2.14), (C.2.32), and (C.2.34) we can write

$$\nu = \frac{s_1 - s_{k_f} - \underline{g}^T[k]\underline{z}[k]}{\omega[k]} \tag{C.2.35}$$

For ready reference, the required equations are gathered together in the following:

$$\boxed{\begin{aligned}
&P[k] = 2\tilde{Q}[k] + \Phi^T P[k+1]\left(I_3 + \Psi[k]P[k+1]\right)^{-1}\Phi \\
&P[k_1] = \begin{bmatrix} 0 & 0 \\ 0 & 0 \end{bmatrix} \\
&\underline{g}[k] = \Phi^T\left(I_3 + P[k+1]\Psi[k]\right)^{-1}\underline{g}[k+1] \\
&\underline{g}[k_1] = \begin{bmatrix} 1 & 0 \end{bmatrix}^T \\
&\omega[k] = \omega[k+1] - \underline{g}^T[k+1]\left(I_3 + \Psi[k]P[k+1]\right)^{-1}\Psi[k]\underline{g}[k+1] \\
&\omega[k_1] = 0
\end{aligned}} \tag{C.2.36}$$

Knowing k_1, we can easily solve equations in (C.2.36) in a backward fashion to obtain the evolution of $P[k]$, $\underline{g}[k]$, and $\omega[k]$ for $k = k_1 - 1, k_1 - 2, \ldots, 1, 0$. Once we calculate $\underline{g}[0]$ and $\omega[0]$, since we already know $\underline{z}[0]$, by inserting these values into (C.2.35), we can find the value of ν as follows:

$$\boxed{\nu = \frac{s_1 - s_{k_f} - \underline{g}^T[0]\underline{z}[0]}{\omega[0]}} \tag{C.2.37}$$

Inserting (C.2.13) into (C.2.9), we have:

$$
\begin{aligned}
i[k] &= -\frac{\Gamma^T}{2\Delta R_{0\mathrm{eq}}[k]}\underline{\lambda}[k+1] \\
&= -\frac{\Gamma^T}{2\Delta R_{0\mathrm{eq}}[k]}\left(P[k+1]\underline{z}[k+1] + \underline{g}[k+1]\nu\right)
\end{aligned}
\tag{C.2.38}
$$

Inserting (C.2.23) into (C.2.38), we can write the optimal current as follows:

$$
\boxed{i[k] = -\frac{\Gamma^T}{2\Delta R_{0\mathrm{eq}}[k]}\left(P[k+1]\left((I_3 + \Psi[k]P[k+1]\right)^{-1}\left(\Phi\underline{z}[k] - \Psi[k]\underline{g}[k+1]\nu\right)\right) + \underline{g}[k+1]\nu\right)}
\tag{C.2.39}
$$

Note that this is a state feedback policy.

Bibliography

[1] *https://github.com/abdollahiali/phd-dissertation-oral-presentation*.

[2] *http://www.keithley.com/products/dcac/currentvoltage/highpower/?mn=2651a*.

[3] *http://www.teamqsi.com/tag/industrial/*.

[4] Burnham, Kenneth P and Anderson, David R, *Model selection and inference: a practical information-theoretic approach*, Springer-Verlag, New York, 1998.

[5] A Abdollahi, X Han, GV Avvari, N Raghunathan, B Balasingam, KR Pattipati, and Y Bar-Shalom, *Optimal battery charging, part I: Minimizing time-to-charge, energy loss, and temperature rise for OCV-resistance battery model*, Journal of Power Sources **303** (2016), 388–398.

[6] A. Abdollahi, X. Han, N. Raghunathan, B. Pattipati, B. Balasingam, K. R. Pattipati, Y. Bar-Shalom, and B. Card, *Optimal charging for general equivalent electrical battery model, and battery life management*, Journal of Energy Storage **9** (2017), 47–58.

[7] A. Abdollahi and K. Pattipati, *Unification of leaky noisy OR and logistic regression models and maximum a posteriori inference for multiple fault diagnosis using the unified model*, DX Conference (Denver, Co), Oct. 4-7 2016.

[8] A. Abdollahi and K. R. Pattipati, *Probabilistic graphical models for fault prognosis in complex systems*, in preparation (2017).

[9] A Abdollahi, N Raghunathan, X Han, GV Avvari, B Balasingam, KR Pattipati, and Y Bar-Shalom, *Battery charging optimization for OCV-resistance equivalent circuit model*, 2015 American Control Conference (ACC), IEEE, 2015, pp. 3467–3472.

[10] A Abdollahi, N Raghunathan, X Han, B Pattipati, B Balasingam, KR Pattipati, Y Bar-Shalom, and B Card, *Battery health degradation and optimal life management*, IEEE AUTOTESTCON, 2015, IEEE, 2015, pp. 146–151.

[11] Ali Abdollahi, Krishna R Pattipati, Anuradha Kodali, Satnam Singh, Shigang Zhang, and Peter B Luh, *Probabilistic graphical models for fault diagnosis in complex systems*, Principles of Performance and Reliability Modeling and Evaluation, Springer, 2016, pp. 109–139.

[12] Rafik A Aliev, Rashad R Aliev, Babek Guirimov, and K Uyar, *Dynamic data mining technique for rules extraction in a process of battery charging*, Applied Soft Computing **8** (2008), no. 3, 1252–1258.

[13] Chrissanthi Angeli and Avraam Chatzinikolaou, *On-line fault detection techniques for technical systems: A survey.*, IJCSA **1** (2004), no. 1, 12–30.

[14] Arora, Pankaj and White, Ralph E and Doyle, Marc, *Capacity fade mechanisms and side reactions in lithium-ion batteries*, Journal of the Electrochemical Society **145** (1998), no. 10, 3647–3667.

[15] M Athans, K-P Dunn, C. S. Greene, WH Lee, NR Sandell, I Segall, and A. S. Willsky, *The stochastic control of the f-8c aircraft using the multiple model adaptive control (MMAC) method*, Decision and Control including the 14th Symposium on Adaptive Processes, 1975 IEEE Conference on, IEEE, 1975, pp. 217–228.

[16] M Athans, K-P Dunn, CS Greene, WH Lee, NR Sandell, I Segall, and AS Willsky, *The stochastic control of the f-8c aircraft using the multiple model adaptive control (mmac) method*, Decision and Control including the 14th Symposium on Adaptive Processes, 1975 IEEE Conference on, vol. 14, IEEE, 1975, pp. 217–228.

[17] Mihiar Ayoubi and Rolf Isermann, *Neuro-fuzzy systems for diagnosis*, Fuzzy sets and Systems **89** (1997), no. 3, 289–307.

[18] Mohammad S Azam, Fang Tu, Krishna R Pattipati, and Rajaiah Karanam, *A dependency model-based approach for identifying and evaluating power quality problems*, IEEE Transactions on power delivery **19** (2004), no. 3, 1154–1166.

[19] George K Baah, Andy Podgurski, and Mary Jean Harrold, *The probabilistic program dependence graph and its application to fault diagnosis*, IEEE Transactions on Software Engineering **36** (2010), no. 4, 528–545.

[20] B Balasingam, GV Avvari, B Pattipati, KR Pattipati, and Y Bar-Shalom, *A robust approach to battery fuel gauging, part I: Real time model identification*, Journal of Power Sources **272** (2014), 1142–1153.

[21] ———, *A robust approach to battery fuel gauging, part II: Real time capacity estimation*, Journal of Power Sources **269** (2014), 949–961.

[22] Michèle Basseville, *Detecting changes in signals and systemsa survey*, Automatica **24** (1988), no. 3, 309–326.

[23] Michele Basseville and Albert Benveniste, *Desgin and comparative study of some sequential jump detection algorithms for digital signals*, IEEE Transactions on Acoustics, Speech, and Signal Processing **31** (1983), no. 3, 521–535.

[24] Michèle Basseville, Igor V Nikiforov, et al., *Detection of abrupt changes: theory and application*, vol. 104, Prentice Hall Englewood Cliffs, 1993.

[25] Richard Vernon Beard, *Failure accomodation in linear systems through self-reorganization.*, Ph.D. thesis, Massachusetts Institute of Technology, 1971.

[26] John E Beasley, *An algorithm for set covering problem*, European Journal of Operational Research **31** (1987), no. 1, 85–93.

[27] ———, *A lagrangian heuristic for set-covering problems*, Naval Research Logistics (NRL) **37** (1990), no. 1, 151–164.

[28] John E Beasley and Paul C Chu, *A genetic algorithm for the set covering problem*, European journal of operational research **94** (1996), no. 2, 392–404.

[29] John E Beasley and Kurt Jörnsten, *Enhancing an algorithm for set covering problems*, European Journal of Operational Research **58** (1992), no. 2, 293–300.

[30] DP Bertsekas, *Nonlinear programming 2nd edn (belmont, ma: Athena scientific)*, (1999).

[31] Zhong Binglin, Yan Tinghu, Huang Ren, and JA Brandon, *A genetic algorithm for diagnosis problem solving*, Systems, Man and Cybernetics, 1993.'Systems Engineering in the Service of Humans', Conference Proceedings., International Conference on, vol. 2, IEEE, 1993, pp. 404–408.

[32] Christopher M Bishop, *Neural networks for pattern recognition*, Oxford university press, 1995.

[33] Douglas M. Blough and Andrzej Pelc, *Complexity of fault diagnosis in comparison models*, IEEE Transactions on computers **41** (1992), no. 3, 318–324.

[34] R Boel, P Varaiya, and E Wong, *Martingales on jump processes. II: Applications*, SIAM Journal on Control **13** (1975), no. 5, 1022–1061.

[35] René Boel, Pravin Varaiya, and Eugene Wong, *Martingales on jump processes. I: Representation results*, SIAM Journal on control **13** (1975), no. 5, 999–1021.

[36] R Boumen, Sui Ruan, Ivo SM de Jong, JM Van De Mortel-Fronczak, JE Rooda, and Krishna R Pattipati, *Hierarchical test sequencing for complex systems*, IEEE Transactions on Systems, Man, and Cybernetics-Part A: Systems and Humans **39** (2009), no. 3, 640–649.

[37] Mikhail A Bragin, Peter B Luh, Joseph H Yan, Nanpeng Yu, and Gary A Stern, *Convergence of the surrogate lagrangian relaxation method*, Journal of Optimization Theory and applications **164** (2015), no. 1, 173.

[38] Kenneth P Burnham, David R Anderson, and Kathryn P Huyvaert, *Aic model selection and multimodel inference in behavioral ecology: some background,*

observations, and comparisons, Behavioral Ecology and Sociobiology **65** (2011), no. 1, 23–35.

[39] Chaturvedi, Nalin A and Klein, Reinhardt and Christensen, Jake and Ahmed, Jasim and Kojic, Aleksandar, *Algorithms for advanced battery-management systems*, IEEE Control Systems **30** (2010), no. 3, 49–68.

[40] Jie Chen and Ron J Patton, *Robust model-based fault diagnosis for dynamic systems*, vol. 3, Springer Science & Business Media, 2012.

[41] Liang-Rui Chen, *A design of an optimal battery pulse charge system by frequency-varied technique*, IEEE Transactions on Industrial Electronics **54** (2007), no. 1, 398–405.

[42] ———, *Design of duty-varied voltage pulse charger for improving li-ion battery-charging response*, IEEE Transactions on Industrial Electronics **56** (2009), no. 2, 480–487.

[43] Liang-Rui Chen, Roy Chaoming Hsu, and Chuan-Sheng Liu, *A design of a grey-predicted li-ion battery charge system*, IEEE Transactions on Industrial Electronics **55** (2008), no. 10, 3692–3701.

[44] Stefano Chessa and Paolo Santi, *Operative diagnosis of graph-based systems with multiple faults*, IEEE Transactions on Systems, Man, and Cybernetics-Part A: Systems and Humans **31** (2001), no. 2, 112–119.

[45] Kihoon Choi, M Madhavi Namburu, Mohammad Azam, Jianhui Luo, Krishna Pattipati, and Ann Patterson-Hine, *Fault diagnosis in hvac chillers using data-*

driven techniques, AUTOTESTCON 2004. Proceedings, IEEE, 2004, pp. 407–413.

[46] Kihoon Choi, Satnam Singh, Anuradha Kodali, Krishna R Pattipati, John W Sheppard, Setu Madhavi Namburu, Shunsuke Chigusa, Danil V Prokhorov, and Liu Qiao, *Novel classifier fusion approaches for fault diagnosis in automotive systems*, IEEE Transactions on Instrumentation and Measurement **58** (2009), no. 3, 602–611.

[47] EYEY Chow and AS Willsky, *Analytical redundancy and the design of robust failure detection systems*, IEEE Transactions on automatic control **29** (1984), no. 7, 603–614.

[48] Vasek Chvatal, *A greedy heuristic for the set-covering problem*, Mathematics of operations research **4** (1979), no. 3, 233–235.

[49] Robert N Clark, Douglas C Fosth, and Vincent M Walton, *Detecting instrument malfunctions in control systems*, IEEE Transactions on Aerospace and Electronic Systems (1975), no. 4, 465–473.

[50] ———, *Detecting instrument malfunctions in control systems*, IEEE Transactions on Aerospace and Electronic Systems (1975), no. 4, 465–473.

[51] Richard C Cope and Yury Podrazhansky, *The art of battery charging*, Battery Conference on Applications and Advances. The Fourteenth Annual, IEEE, 1999, pp. 233–235.

[52] Anton T. Dahbura and Gerald M. Masson, *An $o(n^{2.5})$ fault identification algorithm for diagnosable systems*, IEEE Transactions on Computers (1984), no. 6, 486–492.

[53] Anton T Dahbura, Krishan K Sabnani, and Linda L King, *The comparison approach to multiprocessor fault diagnosis*, IEEE Transactions on Computers **36** (1987), no. 3, 373–378.

[54] Xuewu Dai and Zhiwei Gao, *From model, signal to knowledge: A data-driven perspective of fault detection and diagnosis*, IEEE Transactions on Industrial Informatics **9** (2013), no. 4, 2226–2238.

[55] Jaime M De Faria, Carlos RP Hartmann, Carl L Gerberich, and Pramod Varshney, *An information theoretic approach to the construction of efficient decision trees*, (1980).

[56] Johan De Kleer and Brian C Williams, *Diagnosing multiple faults*, Artificial intelligence **32** (1987), no. 1, 97–130.

[57] Somnath Deb, Krishna R Pattipati, Vijay Raghavan, Mojdeh Shakeri, and Roshan Shrestha, *Multi-signal flow graphs: a novel approach for system testability analysis and fault diagnosis*, IEEE Aerospace and Electronic Systems Magazine **10** (1995), no. 5, 14–25.

[58] AL Dexter, *Fuzzy model based fault diagnosis*, IEE Proceedings-Control Theory and Applications **142** (1995), no. 6, 545–550.

[59] Markus Einhorn, Fiorentino Valerio Conte, Christian Kral, and Juergen Fleig, *A method for online capacity estimation of lithium ion battery cells using the state*

of charge and the transferred charge, IEEE Transactions on Industry Applications **48** (2012), no. 2, 736–741.

[60] N El Alami, A Ouansafi, and N Znaidi, *On the discrete linear quadratic minimum-time problem*, Journal of the Franklin Institute **335** (1998), no. 3, 525–532.

[61] Samuel L Fagin, *Recursive linear regression theory, optimal filter theory, and error analysis of optimal systems*, IEEE international convention record, vol. 12, 1964, pp. 216–245.

[62] De Faria et al., *Application of information theory to sequential fault diagnosis*, IEEE Transactions on Computers **100** (1982), no. 2, 164–170.

[63] Giulio Fedi, Riccardo Giomi, Antonio Luchetta, Stefano Manetti, and Maria Cristina Piccirilli, *On the application of symbolic techniques to the multiple fault location in low testability analog circuits*, IEEE Transactions on Circuits and Systems II: Analog and Digital Signal Processing **45** (1998), no. 10, 1383–1388.

[64] Marshall L Fisher, *The lagrangian relaxation method for solving integer programming problems*, Management science **27** (1981), no. 1, 1–18.

[65] Paul M Frank, *Fault diagnosis in dynamic systems using analytical and knowledge-based redundancy: A survey and some new results*, automatica **26** (1990), no. 3, 459–474.

[66] ———, *Analytical and qualitative model-based fault diagnosis–a survey and some new results*, European Journal of control **2** (1996), no. 1, 6–28.

[67] Paul M Frank and Xianchun Ding, *Survey of robust residual generation and evaluation methods in observer-based fault detection systems*, Journal of process control **7** (1997), no. 6, 403–424.

[68] Paul M Frank and Birgit Köppen-Seliger, *New developments using AI in fault diagnosis*, Engineering Applications of Artificial Intelligence **10** (1997), no. 1, 3–14.

[69] ———, *New developments using ai in fault diagnosis*, Engineering Applications of Artificial Intelligence **10** (1997), no. 1, 3–14.

[70] PM Frank, SX Ding, and T Marcu, *Model-based fault diagnosis in technical processes*, Transactions of the Institute of Measurement and Control **22** (2000), no. 1, 57–101.

[71] Zhiwei Gao, Carlo Cecati, and Steven X Ding, *A survey of fault diagnosis and fault-tolerant techniquespart i: Fault diagnosis with model-based and signal-based approaches*, IEEE Transactions on Industrial Electronics **62** (2015), no. 6, 3757–3767.

[72] M. R. Garey and D. S. Johnson, *Computers and intractability : A guide to the theory of np-completeness*, New York: Freeman, 1983.

[73] Janos J Gertler, *Survey of model-based failure detection and isolation in complex plants*, IEEE Control systems magazine **8** (1988), no. 6, 3–11.

[74] ———, *Fault detection and diagnosis in engineering systems*, CRC press, 1998.

[75] Kai Goebel, Bhaskar Saha, Abhinav Saxena, Jose R Celaya, and Jon P Christophersen, *Prognostics in battery health management*, IEEE instrumentation & measurement magazine **11** (2008), no. 4, 33–40.

[76] Guifang Guo, Peng Xu, Zhifeng Bai, Shiqiong Zhou, Gang Xu, and Binggang Cao, *Optimization of ni-mh battery fast charging in electric vehicles using dynamic data mining and anfis*, International Conference on Intelligent Computing, Springer, 2008, pp. 468–475.

[77] Zhen Guo, Bor Yann Liaw, Xinping Qiu, Lanlan Gao, and Changshui Zhang, *Optimal charging method for lithium ion batteries using a universal voltage protocol accommodating aging*, Journal of Power Sources **274** (2015), 957–964.

[78] Zhen Guo, Xinping Qiu, Guangdong Hou, Bor Yann Liaw, and Changshui Zhang, *State of health estimation for lithium ion batteries based on charging curves*, Journal of Power Sources **249** (2014), 457–462.

[79] Edmund Handschin, Fred C Schweppe, Jurg Kohlas, and Armin Fiechter, *Bad data analysis for power system state estimation*, IEEE Transactions on Power Apparatus and Systems **94** (1975), no. 2, 329–337.

[80] ———, *Bad data analysis for power system state estimation*, Power Apparatus and Systems, IEEE Transactions on **94** (1975), no. 2, 329–337.

[81] Fan He and Lin Ma, *Thermal management of batteries employing active temperature control and reciprocating cooling flow*, International Journal of Heat and Mass Transfer **83** (2015), 164–172.

[82] Wei He, Nicholas Williard, Michael Osterman, and Michael Pecht, *Prognostics of lithium-ion batteries based on dempster–shafer theory and the bayesian monte carlo method*, Journal of Power Sources **196** (2011), no. 23, 10314–10321.

[83] Nicholas J Higham, *Accuracy and stability of numerical algorithms*, Siam, 2002.

[84] Xiaosong Hu, Shengbo Li, Huei Peng, and Fengchun Sun, *Charging time and loss optimization for linmc and lifepo 4 batteries based on equivalent circuit models*, Journal of Power Sources **239** (2013), 449–457.

[85] Hu, Xiaosong and Li, Shengbo Eben and Jia, Zhenzhong and Egardt, Bo, *Enhanced sample entropy-based health management of Li-ion battery for electrified vehicles*, Energy **64** (2014), 953–960.

[86] Inseok Hwang, Sungwan Kim, Youdan Kim, and Chze Eng Seah, *A survey of fault detection, isolation, and reconfiguration methods*, IEEE Transactions on Control Systems Technology **18** (2010), no. 3, 636–653.

[87] Laurent Hyafil and Ronald L Rivest, *Constructing optimal binary decision trees is np-complete*, Information processing letters **5** (1976), no. 1, 15–17.

[88] Tomohiko Ikeya, Nobuyuki Sawada, Jun-ich Murakami, Kazsuyuki Kobayashi, Masanori Hattori, Nobuo Murotani, Satoru Ujiie, Katuya Kajiyama, Hideki Nasu, Hayato Narisoko, et al., *Multi-step constant-current charging method for an electric vehicle nickel/metal hydride battery with high-energy efficiency and long cycle life*, Journal of power sources **105** (2002), no. 1, 6–12.

[89] Tomohiko Ikeya, Nobuyuki Sawada, Sakae Takagi, Jun-ichi Murakami, Kazuyuki Kobayashi, Tetsuya Sakabe, Eiichi Kousaka, Haruki Yoshioka, Satoru Kato,

Masanori Yamashita, et al., *Multi-step constant-current charging method for electric vehicle, valve-regulated, lead/acid batteries during night time for load-levelling*, Journal of power sources **75** (1998), no. 1, 101–107.

[90] Rolf Isermann, *Process fault detection based on modeling and estimation methodsa survey*, automatica **20** (1984), no. 4, 387–404.

[91] ———, *On fuzzy logic applications for automatic control, supervision, and fault diagnosis*, IEEE Transactions on Systems, Man, and Cybernetics-Part A: Systems and Humans **28** (1998), no. 2, 221–235.

[92] ———, *Model-based fault-detection and diagnosis–status and applications*, Annual Reviews in control **29** (2005), no. 1, 71–85.

[93] Rolf Isermann and Peter Balle, *Trends in the application of model-based fault detection and diagnosis of technical processes*, Control engineering practice **5** (1997), no. 5, 709–719.

[94] A Jazwinski, *Limited memory optimal filtering*, IEEE Transactions on Automatic Control **13** (1968), no. 5, 558–563.

[95] Andrew H Jazwinski, *Stochastic processes and filtering theory*, Courier Corporation, 2007.

[96] Shengbing Jiang and Ratnesh Kumar, *Failure diagnosis of discrete-event systems with linear-time temporal logic specifications*, IEEE Transactions on Automatic Control **49** (2004), no. 6, 934–945.

[97] Harold Lee Jones, *Failure detection in linear systems.*, Ph.D. thesis, Massachusetts Institute of Technology, 1973.

[98] ———, *Failure detection in linear systems.*, Ph.D. thesis, Massachusetts Institute of Technology, 1973.

[99] Michael Irwin Jordan, *Learning in graphical models*, vol. 89, Springer Science & Business Media, 1998.

[100] Peter Keil and Andreas Jossen, *Charging protocols for lithium-ion batteries and their impact on cycle lifean experimental study with different 18650 high-power cells*, Journal of Energy Storage **6** (2016), 125–141.

[101] T. H. Kerr, *A two ellipsoid overlap test for real time failure detection and isolation by confidence regions*, IEEE Conference on Decision and Control including the 13th Symposium on Adaptive Processes, 1974, pp. 735–742.

[102] Klein, Reinhardt and Chaturvedi, Nalin A and Christensen, Jake and Ahmed, Jasim and Findeisen, Rolf and Kojic, Aleksandar, *Optimal charging strategies in lithium-ion battery*, Proceedings of the 2011 American Control Conference, IEEE, 2011, pp. 382–387.

[103] Anuradha Kodali, Krishna Pattipati, and Satnam Singh, *Coupled factorial hidden markov models (cfhmm) for diagnosing multiple and coupled faults*, IEEE Transactions on Systems, Man, and Cybernetics: Systems **43** (2013), no. 3, 522–534.

[104] Anuradha Kodali, Satnam Singh, and Krishna Pattipati, *Dynamic set-covering for real-time multiple fault diagnosis with delayed test outcomes*, IEEE Transactions on Systems, Man, and Cybernetics: Systems **43** (2013), no. 3, 547–562.

[105] Anuradha Kodali, Yilu Zhang, Chaitanya Sankavaram, Krishna Pattipati, and Mutasim Salman, *Fault diagnosis in the automotive electric power generation and storage system (epgs)*, IEEE/ASME Transactions on Mechatronics **18** (2013), no. 6, 1809–1818.

[106] Masasumi Kokawa, Satoshi Miyazaki, and Sadanori Shingai, *Fault location using digraph and inverse direction search with application*, Automatica **19** (1983), no. 6, 729–735.

[107] Mattias Krysander and Erik Frisk, *Sensor placement for fault diagnosis*, IEEE Transactions on Systems, Man, and Cybernetics-Part A: Systems and Humans **38** (2008), no. 6, 1398–1410.

[108] Benjamin Kuipers, *The limits of qualitative simulation.*, IJCAI, 1985, pp. 128–136.

[109] ———, *Qualitative simulation*, Artificial intelligence **29** (1986), no. 3, 289–338.

[110] ———, *Qualitative simulation as causal explanation*, IEEE Transactions on Systems, Man, and Cybernetics **17** (1987), no. 3, 432–444.

[111] D. G. Lainiotis, *Joint detection, estimation and system identification*, Information and control **19** (1971), no. 1, 75–92.

[112] Steffen Leonhardt and M Ayoubi, *Methods of fault diagnosis*, Control engineering practice **5** (1997), no. 5, 683–692.

[113] Jun Li, Edward Murphy, Jack Winnick, and Paul A Kohl, *The effects of pulse charging on cycling characteristics of commercial lithium-ion batteries*, Journal of Power Sources **102** (2001), no. 1, 302–309.

[114] Xianke Lin, Jonghyun Park, Lin Liu, Yoonkoo Lee, AM Sastry, and Wei Lu, *A comprehensive capacity fade model and analysis for li-ion batteries*, Journal of The Electrochemical Society **160** (2013), no. 10, A1701–A1710.

[115] Yi-Hwa Liu, Ching-Hsing Hsieh, and Yi-Feng Luo, *Search for an optimal five-step charging pattern for li-ion batteries using consecutive orthogonal arrays*, IEEE Transactions on Energy Conversion **26** (2011), no. 2, 654–661.

[116] Yi-Hwa Liu and Yi-Feng Luo, *Search for an optimal rapid-charging pattern for li-ion batteries using the taguchi approach*, IEEE Transactions on Industrial Electronics **57** (2010), no. 12, 3963–3971.

[117] Yi-Hwa Liu, Jen-Hao Teng, and Yu-Chung Lin, *Search for an optimal rapid charging pattern for lithium-ion batteries using ant colony system algorithm*, IEEE Transactions on Industrial Electronics **52** (2005), no. 5, 1328–1336.

[118] Lennart Ljung and Torsten Söderström, *Theory and practice of recursive identification*, vol. 5, JSTOR, 1983.

[119] Jianhui Luo, Madhavi Namburu, Krishna R Pattipati, Liu Qiao, and Shunsuke Chigusa, *Integrated model-based and data-driven diagnosis of automotive antilock braking systems*, IEEE Transactions on Systems, Man, and Cybernetics-Part A: Systems and Humans **40** (2010), no. 2, 321–336.

[120] Jianhui Luo, Krishna R Pattipati, Liu Qiao, and Shunsuke Chigusa, *An integrated diagnostic development process for automotive engine control systems*, IEEE Transactions on Systems, Man, and Cybernetics, Part C (Applications and Reviews) **37** (2007), no. 6, 1163–1173.

[121] M-A Massoumnia, *A geometric approach to the synthesis of failure detection filters*, IEEE Transactions on automatic control **31** (1986), no. 9, 839–846.

[122] Raman K Mehra and J Peschon, *An innovations approach to fault detection and diagnosis in dynamic systems*, Automatica **7** (1971), no. 5, 637–640.

[123] ———, *An innovations approach to fault detection and diagnosis in dynamic systems*, Automatica **7** (1971), no. 5, 637–640.

[124] Hyde McCune Merrill, *Bad data suppression in state estimation, with applications to problems in power.*, Ph.D. thesis, Massachusetts Institute of Technology, 1972.

[125] Hyde McCune Merrill, *Bad data suppression in state estimation, with applications to problems in power.*, Ph.D. thesis, Massachusetts Institute of Technology, 1972.

[126] Walter C Merrill, *Sensor failure detection for jet engines using analytical redundancy*, J. Guidance **8** (1985), no. 8.

[127] John A Miller, Walter D Potter, Ravi V Gandham, and Chito N Lapena, *An evaluation of local improvement operators for genetic algorithms*, IEEE Transactions on Systems, Man, and Cybernetics **23** (1993), no. 5, 1340–1351.

[128] R Miller, *Complexity of computer computations: Proceedings of a symposium on the complexity of computer computations, held march 20–22, 1972, at the ibm thomas j. watson research center, yorktown heights, new york, and sponsored by the office of naval research, mathematics program, ibm world trade corporation, and the ibm research mathematical sciences department*, Springer Science & Business Media, 2013.

[129] Robert Milne, *Strategies for diagnosis*, IEEE Transactions on Systems, Man, and Cybernetics **17** (1987), no. 3, 333–339.

[130] Kevin P Murphy, *Machine learning: a probabilistic perspective*, MIT press, 2012.

[131] Kenney Ng and Richard P Lippmann, *A comparative study of the practical characteristics of neural network and conventional pattern classifiers*, Advances in neural information processing systems, 1991, pp. 970–976.

[132] Peter HL Notten, JHG Op het Veld, and JRG Van Beek, *Boostcharging li-ion batteries: A challenging new charging concept*, Journal of Power Sources **145** (2005), no. 1, 89–94.

[133] Mattias Nyberg, *Model-based diagnosis of an automotive engine using several types of fault models*, IEEE Transactions on control systems technology **10** (2002), no. 5, 679–689.

[134] Claire E Parfitt, William E Crofts, and Rachel Buckle, *An adaptable lithium-ion battery model*, ECS Transactions **28** (2010), no. 22, 21–33.

[135] B Pattipati, B Balasingam, A Abdollahi, GV Avvari, KR Pattipati, and Y Bar-Shalom, *Integrated battery fuel gauge and optimal charger*, 2014 IEEE AUTOTEST, IEEE, 2014, pp. 260–269.

[136] Bharath Pattipati, Chaitanya Sankavaram, and Krishna Pattipati, *System identification and estimation framework for pivotal automotive battery management system characteristics*, IEEE Transactions on Systems, Man, and Cybernetics, Part C (Applications and Reviews) **41** (2011), no. 6, 869–884.

[137] KR Pattipati, V Raghavan, M Shakeri, S Deb, and R Shrestha, *Teams: testability engineering and maintenance system*, American Control Conference, 1994, vol. 2, IEEE, 1994, pp. 1989–1995.

[138] Krishna R Pattipati and Mark G Alexandridis, *Application of heuristic search and information theory to sequential fault diagnosis*, IEEE Transactions on Systems, Man, and Cybernetics **20** (1990), no. 4, 872–887.

[139] Krishna R Pattipati and Mahesh Dontamsetty, *On a generalized test sequencing problem*, IEEE transactions on systems, man, and cybernetics **22** (1992), no. 2, 392–396.

[140] RJ Patton, *Fault detection and diagnosis in aerospace systems using analytical redundancy*, Computing & Control Engineering Journal **2** (1991), no. 3, 127–136.

[141] RJ Patton, FJ Uppal, and CJ Lopez-Toribio, *Soft computing approaches to fault diagnosis for dynamic systems: a survey*, IFAC Proceedings Volumes **33** (2000), no. 11, 303–315.

[142] Ron J Patton, *Robustness in model-based fault diagnosis: the 1995 situation*, Annual reviews in control **21** (1997), 103–123.

[143] Ron J Patton, Paul M Frank, and Robert N Clark, *Issues of fault diagnosis for dynamic systems*, Springer Science & Business Media, 2000.

[144] Yun Peng and James A Reggia, *A probabilistic causal model for diagnostic problem solving part i: Integrating symbolic causal inference with numeric probabilistic inference*, IEEE Transactions on Systems, Man, and Cybernetics **17** (1987), no. 2, 146–162.

[145] ———, *A probabilistic causal model for diagnostic problem solving part ii: Diagnostic strategy*, IEEE Transactions on Systems, Man, and Cybernetics **17** (1987), no. 3, 395–406.

[146] Ahmad A Pesaran, *Battery thermal models for hybrid vehicle simulations*, Journal of Power Sources **110** (2002), no. 2, 377–382.

[147] Ahmad A Pesaran, Andreas Vlahinos, and Steven D Burch, *Thermal performance of ev and hev battery modules and packs*, National Renewable Energy Laboratory, 1997.

[148] Panom Petchjatuporn, Noppadol Khaehintung, Khamron Sunat, Phaophak Sirisuk, and Wiwat Kiranon, *Implementation of GA-trained GRNN for intelligent fast charger for ni-cd batteries*, Power Electronics and Motion Control Conference, CES/IEEE 5th International, vol. 1, IEEE, 2006, pp. 1–5.

[149] David Walter Peterson, *Hypothesis, estimation, and validation of dynamic social models: energy demand modeling.*, Ph.D. thesis, Massachusetts Institute of Technology, 1975.

[150] Gregory L Plett, *Extended kalman filtering for battery management systems of LiPB-based hev battery packs: Part 3. state and parameter estimation*, Journal of Power sources **134** (2004), no. 2, 277–292.

[151] ———, *Recursive approximate weighted total least squares estimation of battery cell total capacity*, Journal of Power Sources **196** (2011), no. 4, 2319–2331.

[152] Prasad, Githin K and Rahn, Christopher D, *Model based identification of aging parameters in lithium ion batteries*, Journal of power sources **232** (2013), 79–85.

[153] BK Purushothaman and U Landau, *Rapid charging of lithium-ion batteries using pulsed currents a theoretical analysis*, Journal of The Electrochemical Society **153** (2006), no. 3, A533–A542.

[154] Vijay Raghavan, Mojdeh Shakeri, and Krishna Pattipati, *Optimal and near-optimal test sequencing algorithms with realistic test models*, IEEE Transactions on systems, man, and cybernetics-part A: Systems and Humans **29** (1999), no. 1, 11–26.

[155] Vijay Raghavan, Mojdeh Shakeri, and Krishna R Pattipati, *Test sequencing problems arising in test planning and design for testability*, IEEE Transactions on Systems, Man, and Cybernetics-Part A: Systems and Humans **29** (1999), no. 2, 153–163.

[156] Vijaya Raghavan, Mojdeh Shakeri, and Krishna Pattipati, *Test sequencing algorithms with unreliable tests*, IEEE Transactions on Systems, Man, and Cybernetics-Part A: Systems and Humans **29** (1999), no. 4, 347–357.

[157] Nageswara SV Rao, *On parallel algorithms for single-fault diagnosis in fault propagation graph systems*, IEEE Transactions on Parallel and Distributed Systems **7** (1996), no. 12, 1217–1223.

[158] Raymond Reiter, *A theory of diagnosis from first principles*, Artificial intelligence **32** (1987), no. 1, 57–95.

[159] Frank Rijmen, *Bayesian networks with a logistic regression model for the conditional probabilities*, International Journal of Approximate Reasoning **48** (2008), no. 2, 659–666.

[160] Peng Rong and Massoud Pedram, *An analytical model for predicting the remaining battery capacity of lithium-ion batteries*, IEEE Transactions on Very Large Scale Integration (VLSI) Systems **14** (2006), no. 5, 441–451.

[161] Sui Ruan, Fang Tu, Krishna R Pattipati, and Ann Patterson-Hine, *On a multimode test sequencing problem*, IEEE Transactions on Systems, Man, and Cybernetics, Part B (Cybernetics) **34** (2004), no. 3, 1490–1499.

[162] Bhaskar Saha, Kai Goebel, Scott Poll, and Jon Christophersen, *Prognostics methods for battery health monitoring using a bayesian framework*, IEEE Transactions on Instrumentation and Measurement **58** (2009), no. 2, 291–296.

[163] Meera Sampath, Raja Sengupta, Stéphane Lafortune, Kasim Sinnamohideen, and Demosthenis Teneketzis, *Diagnosability of discrete-event systems*, IEEE Transactions on automatic control **40** (1995), no. 9, 1555–1575.

[164] Meera Sampath, Raja Sengupta, Stephane Lafortune, Kasim Sinnamohideen, and Demosthenis C Teneketzis, *Failure diagnosis using discrete-event models*, IEEE transactions on control systems technology **4** (1996), no. 2, 105–124.

[165] FRED C Schweppe and EDMUND J Handschin, *Static state estimation in electric power systems*, Proceedings of the IEEE **62** (1974), no. 7, 972–982.

[166] Fred C Schweppe and Edmund J Handschin, *Static state estimation in electric power systems*, Proceedings of the IEEE **62** (1974), no. 7, 972–982.

[167] Mojdeh Shakeri, Vijaya Raghavan, Krishna R Pattipati, and Ann Patterson-Hine, *Optimal and near-optimal algorithms for multiple fault diagnosis with*

unreliable tests, IEEE Transactions on Systems, Man, and Cybernetics, Part C (Applications and Reviews) **28** (1998), no. 3, 431–440.

[168] ———, *Sequential testing algorithms for multiple fault diagnosis*, IEEE Transactions on Systems, Man, and Cybernetics-Part A: Systems and Humans **30** (2000), no. 1, 1–14.

[169] Michael A Shwe, Blackford Middleton, DE Heckerman, Max Henrion, EJ Horvitz, HP Lehmann, and GF Cooper, *Probabilistic diagnosis using a reformulation of the internist-1/qmr knowledge base*, Methods of information in Medicine **30** (1991), no. 4, 241–255.

[170] Satnam Singh, Anuradha Kodali, Kihoon Choi, Krishna R Pattipati, Setu Madhavi Namburu, Shunsuke Chigusa Sean, Danil V Prokhorov, and Liu Qiao, *Dynamic multiple fault diagnosis: Mathematical formulations and solution techniques*, IEEE Transactions on Systems, Man, and Cybernetics-Part A: Systems and Humans **39** (2009), no. 1, 160–176.

[171] K Sinnamohideen, *Discrete-event based diagnostic supervisory control system*, Proceedings of the AIChE Annual Meeting, 1991.

[172] Padhraic Smyth, *Hidden markov models for fault detection in dynamic systems*, Pattern recognition **27** (1994), no. 1, 149–164.

[173] ———, *Markov monitoring with unknown states*, IEEE Journal on Selected Areas in Communications **12** (1994), no. 9, 1600–1612.

[174] Peter Struss and Chris Price, *Model-based systems in the automotive industry*, AI magazine **24** (2003), no. 4, 17.

[175] Suthar, Bharatkumar and Ramadesigan, Venkatasailanathan and De, Sumitava and Braatz, Richard D and Subramanian, Venkat R, *Optimal charging profiles for mechanically constrained lithium-ion batteries*, Physical Chemistry Chemical Physics **16** (2014), no. 1, 277–287.

[176] Tzyh Jong Tarn and Johnson Zaborszky, *A practical nondiverging filter*, AIAA Journal **8** (1970), no. 6, 1127–1133.

[177] Sergios Theodoridis, *Machine learning: a bayesian and optimization perspective*, Academic Press, 2015.

[178] Louise Travé-Massuyes, Teresa Escobet, and Xavier Olive, *Diagnosability analysis based on component-supported analytical redundancy relations*, IEEE Transactions on Systems, Man, and Cybernetics-Part A: Systems and Humans **36** (2006), no. 6, 1146–1160.

[179] Fang Tu and Krishna R. Pattipati, *Rollout strategies for sequential fault diagnosis*, IEEE Transactions on Systems, Man, and Cybernetics-Part A: Systems and Humans **33** (2003), no. 1, 86–99.

[180] Fang Tu, Krishna R. Pattipati, Somnath Deb, and Venkata Narayana Malepati, *Computationally efficient algorithms for multiple fault diagnosis in large graph-based systems*, IEEE Transactions on Systems, Man, and Cybernetics-Part A: Systems and Humans **33** (2003), no. 1, 73–85.

[181] LH Ungar, BA Powell, and SN Kamens, *Adaptive networks for fault diagnosis and process control*, Computers & Chemical Engineering **14** (1990), no. 4-5, 561–572.

[182] Francis J Vasko and George R Wilson, *Using a facility location algorithm to solve large set covering problems*, Operations Research Letters **3** (1984), no. 2, 85–90.

[183] Venkat Venkatasubramanian, Raghunathan Rengaswamy, Surya N Kavuri, and Kewen Yin, *A review of process fault detection and diagnosis: Part iii: Process history based methods*, Computers & chemical engineering **27** (2003), no. 3, 327–346.

[184] Venkat Venkatasubramanian, Raghunathan Rengaswamy, Kewen Yin, and Surya N Kavuri, *A review of process fault detection and diagnosis: Part i: Quantitative model-based methods*, Computers & chemical engineering **27** (2003), no. 3, 293–311.

[185] Venkat Venkatsubramanian, *A review of process fault detection and diagnosis, part ii: Qualitative models and search strategics*, Computers and Chemical Engineering **27** (2003), no. 3, 313–326.

[186] EI Verriest and FL Lewis, *On the linear quadratic minimum-time problem*, IEEE transactions on automatic control **36** (1991), no. 7, 859–863.

[187] Thanh Tu Vo, Xiaopeng Chen, Weixiang Shen, and Ajay Kapoor, *New charging strategy for lithium-ion batteries based on the integration of taguchi method and state of charge estimation*, Journal of Power Sources **273** (2015), 413–422.

[188] ———, *New charging strategy for lithium-ion batteries based on the integration of taguchi method and state of charge estimation*, Journal of Power Sources **273** (2015), 413–422.

[189] Sholom M Weiss and Ioannis Kapouleas, *An empirical comparison of pattern recognition, neural nets and machine learning classification methods*, Readings in machine learning (1990), 177–183.

[190] JOHNE White and JASONL Speyer, *Detection filter design: Spectral theory and algorithms*, IEEE Transactions on Automatic Control **32** (1987), no. 7, 593–603.

[191] A. S. Willsky, *A survey of design methods for failure detection in dynamic systems*, Automatica **12** (Nov. 1976), no. 6, 601–611.

[192] Alan Willsky and H Jones, *A generalized likelihood ratio approach to the detection and estimation of jumps in linear systems*, IEEE Transactions on Automatic control **21** (1976), no. 1, 108–112.

[193] ———, *A generalized likelihood ratio approach to the detection and estimation of jumps in linear systems*, IEEE Transactions on Automatic control **21** (1976), no. 1, 108–112.

[194] Alan S Willsky, *A survey of design methods for failure detection in dynamic systems*, Automatica **12** (1976), no. 6, 601–611.

[195] Alan S Willsky, JJ Deyst, and BS Crawford, *Two self-test methods applied to an inertial system problem*, Journal of Spacecraft and Rockets **12** (1975), 434–437.

[196] Randy Ben Wright, Chester George Motloch, Jeffrey R Belt, Jon Petter Christophersen, Chinh Dac Ho, Roger Allen Richardson, I Bloom, SA Jones, Vincent S Battaglia, GL Henriksen, et al., *Calendar-and cycle-life studies of advanced technology development program generation 1 lithium-ion batteries*, Journal of power sources **110** (2002), no. 2, 445–470.

[197] Thomas D Wu, *A problem decomposition method for efficient diagnosis and interpretation of multiple disorders*, Computer methods and programs in biomedicine **35** (1991), no. 4, 239–250.

[198] Jingyu Yan, Guoqing Xu, Huihuan Qian, Yangsheng Xu, and Zhibin Song, *Model predictive control-based fast charging for vehicular batteries*, Energies **4** (2011), no. 8, 1178–1196.

[199] M Yildiz, H Karakoc, and I Dincer, *Modeling and validation of temperature changes in a pouch lithium-ion battery at various discharge rates*, International Communications in Heat and Mass Transfer **75** (2016), 311–314.

[200] Feili Yu, Fang Tu, Haiying Tu, and Krishna R Pattipati, *A lagrangian relaxation algorithm for finding the map configuration in qmr-dt*, IEEE Transactions on Systems, Man, and Cybernetics-Part A: Systems and Humans **37** (2007), no. 5, 746–757.

[201] Jingliang Zhang and Jay Lee, *A review on prognostics and health monitoring of li-ion battery*, Journal of Power Sources **196** (2011), no. 15, 6007–6014.

[202] Jixiao Zhang, Jingxian Yu, Chuansin Cha, and Hanxi Yang, *The effects of pulse charging on inner pressure and cycling characteristics of sealed ni/mh batteries*, Journal of power sources **136** (2004), no. 1, 180–185.

[203] P Zhang and SX Ding, *On fault detection in linear discrete-time, periodic, and sampled-data systems*, Journal of control science and engineering **2008** (2008), 8.

[204] Shigang Zhang, Krishna R Pattipati, Zheng Hu, Xisen Wen, and Chaitanya Sankavaram, *Dynamic coupled fault diagnosis with propagation and observation delays*, IEEE Transactions on Systems, Man, and Cybernetics: Systems **43** (2013), no. 6, 1424–1439.

[205] Zhang, D and Haran, BS and Durairajan, A and White, Ralph E and Podrazhansky, Y and Popov, Branko N, *Studies on capacity fade of lithium-ion batteries*, Journal of Power Sources **91** (2000), no. 2, 122–129.

[206] Huiming Zou, Wei Wang, Guiying Zhang, Fei Qin, Changqing Tian, and Yuying Yan, *Experimental investigation on an integrated thermal management system with heat pipe heat exchanger for electric vehicle*, Energy Conversion and Management **118** (2016), 88–95.